Department of Physics
Faculty of Mathematics and Natural Sciences
Dresden University of Technology

Structure, microstructure and magnetic properties of electrodeposited Co and Co-Pt in different nanoscale geometries

Dissertation
for the partial fulfillment of the requirements
for the academic degree of
Doctor rerum naturalium
(Dr. rer. nat.)

by
M. Tech. Manvendra Singh Khatri
born on 6th September 1978 in Sugi (Chamoli), Uttrakhand, India

Dresden
2010

Tag der Einreichung: 13.01.2010
Tag der Verteidigung: 09.07.2010

1. Gutachter: Prof. Dr. L. Schultz (TU Dresden and IFW Dresden)

2. Gutachter: Prof. Dr. V. Srinivas (IIT Kharagpur)

Abstract

Thin films and nanowires of Co-Pt have been prepared by means of electrodeposition. Composition, structure, microstructure and magnetic properties have been intensively studied using X-ray diffraction, scanning electron microscopy and vibrating sample magnetometry and correlated to the deposition parameters such as electrolyte composition, deposition current and/or potential. Co rich Co-Pt films have been deposited at various current densities. A nearly constant composition of $Co_{70}Pt_{30}$ was achieved for current densities between 18 and 32 mA/cm². Detailed texture measurements confirmed an increasing fraction of the hexagonal phase with its c-axis aligned perpendicular to the film plane with increasing current density. Accordingly, magnetic properties are strongly affected by the magnetocrystalline anisotropy of the hexagonal phase that competes with the shape anisotropy of the thin film geometry. Co-Pt nanowires have been prepared within alumina templates at different deposition potentials between -0.6 and -0.9V_{SCE} changing the composition from nearly pure Pt to Co. The composition $Co_{80}Pt_{20}$ was observed at a deposition potential of -0.7V_{SCE}. Co-Pt nanowires are nanocrystalline in the as-deposited state. Magnetic measurements reveal changing fcc and hcp phase fractions within the wires as the effective anisotropy significantly differs from the expected shape anisotropy for nanowires with high aspect ratio. This change in effective anisotropy is attributed to the preferential alignment of the c-axis of hcp Co-Pt phase perpendicular to the nanowires axis. A promising alternative with much smaller feature sizes is the diblock copolymer template. Electrodeposition of Co and Co-Pt into these templates has been carried out. Inhomogeneities in the template thickness as well as a certain substrate roughness have been identified to be the reasons for inhomogeneous template filling. Thus magnetic properties are dominated by large deposits found on top of the template. Additionally, rolled-up tubes of several nm thick Au/Co/Au films have been characterized magnetically. Temperature dependent measurements show an exchange bias behaviour that is explained in terms of induced stresses during cooling. Changes of magnetic properties in the investigated samples are finally discussed in terms of competing effects of different magnetic anisotropies in various geometries.

Kurzfassung

Co-Pt Dünnschichten und Nanodrähte wurden mittels elektrochemischer Abscheidung hergestellt. Zusammensetzung, Struktur, Mikrostruktur und magnetische Eigenschaften wurden intensiv mit Röntgenbeugung, Rasterelektronenmikroskopie und Magnetometrie untersucht und mit den Depositionsparametern wie Elektrolytzusammensetzung, Abscheidestrom und/oder-potential korreliert. Co reiche Co-Pt-Filme wurden mit verschiedenen Stromdichten hergestellt. Eine nahezu konstante Zusammensetzung im Bereich $Co_{70}Pt_{30}$ wurde für Stromdichten zwischen 18 und 32 mA/cm^2 erreicht. Detaillierte Texturmessungen bestätigen einen zunehmenden Anteil an hexagonaler Phase mit senkrecht zur Filmebene ausgerichteter c-Achse mit zunehmender Stromdichte. Dementsprechend werden die magnetischen Eigenschaften stark von der magnetokristallinen Anisotropie der hexagonalen Phase beeinflusst, die mit der Formanisotropie der Dünnschicht-Geometrie konkurriert. Co-Pt-Nanodrähte wurden in nanoporöse Aluminiumoxidmembranen bei verschiedenen Potentialen zwischen -0,6 und -0.9 V_{SCE} abgeschieden, wobei sich die Zusammensetzung von nahezu reinem Pt zu Co verändert. Die Zusammensetzung $Co_{80}Pt_{20}$ wurde bei einem Abscheidepotential von -0.7 V_{SCE} erhalten. Die so hergestellten Co-Pt Nanodrähte sind nanokistallin. Magnetische Messungen weisen jedoch auf veränderte Phasenanteile der fcc und hcp Phase innerhalb der Drähte hin, da die effektive Anisotropie erheblich von der für Nanodrähte mit hohem Aspektverhältnis erwarteten Formanisotropie abweicht. Diese Änderung der effektiven Anisotropie ist auf die bevorzugte Ausrichtung der hexagonalen c-Achse des Co-Pt senkrecht zur Drahtachse zurückzuführen. Vielversprechende Template mit deutlich kleineren Dimensionen sind Diblockcopolymertemplate. Es wurden Versuche zur Abscheidung von Co und Co-Pt in diese Template durchgeführt. Als Gründe für die inhomogene Templatfüllung wurden Inhomogenitäten in der Schichtdicke sowie eine gewisse Rauhigkeit der Substrate identifiziert. Aufgrund der ungleichmäßigen Fülleg werden die magnetischen Eigenschaften durch große, halbkugelförmige Abscheidunge auf der Oberfläche des Templates bestimmt. Darüber hinaus wurden aus wenige nm dicken Au/Co/Au Filmen hergestellte Mikroröhren magnetisch charakterisiert. Temperaturabhängige Messungen zeigen ein Exchange Bias Verhalten, das durch beim Abkühlen induzierte Spannungen erklärt wird. Unterschiede

im magnetischen Verhalten der untersuchten Proben werden abschließend im Hinblick auf die verschiedenen konkurrierenden magnetischen Anisotropien in verschiedenen Geometrien diskutiert.

Contents

Introduction ……………………………………………………………………………..1

1 Fundamentals and background ……………………………………………………...5

1.1 Different types of magnetic anisotropy ....……………………………5

1.2 Electrodeposition ……………………………………………………………...9

1.2.1 Fundamentals ……………………………………………………………9

1.2.2 Electrodeposition of alloys ……………………………………………..10

1.3 Co-Pt thin films ……………………………………………………………...12

1.3.1 Background and applications …………………………………………...12

1.3.2 Phase diagram of the Co-Pt system ……………………………………12

1.3.3 Structure and magnetic properties of $L1_0$ and Co-rich Co-Pt films ……………………………………………………………………14

1.3.4 Electrodeposited Co-Pt films …………………………………………...17

1.4 Nanostructuring for magnetic materials ………………………….....................21

1.4.1 Nanolithography ………………………………………………………......21

1.4.2 Self-assembly of porous media ……………………………………...21

1.5 Co-Pt Nanowires ……………………………………………………………....24

1.5.1 Background and applications …………………………………….......24

1.5.2 Crystal structure and phase formation ………………………….......25

1.5.3 Studies on magnetic properties of CoPt nanowires …………………26

2 Experimental methods ……………………………………………………………….31

2.1 Electrodeposition set-up for thin films ……………………………………......31

2.2 Alumina template fabrication …………………………………………………32

2.3 Diblock copolymer template fabrication ………………………………........34

2.4 Electrodeposition set-up for nanowires ……………………………………….37

2.5 Structural characterization …………………………………………….........38

2.5.1 X-ray diffraction (XRD) …………………………………………......38

2.5.2 Pole figure analysis ………………………………………………......39

2.6 Vibrating sample magnetometry (VSM) …………………………...........40

2.7 Scanning electron microscopy (SEM) ………………………………….....41

2.8 Atomic force microscopy (AFM) / Magnetic force microscopy (MFM) ……..44

3 Continuous Co-Pt films ………………………………………………………..47

3.1 Current-potential curves ……………………………………………........47

3.2 Film morphology and chemical composition ……………………….......48

3.3 Phase formation and crystal structure ………………………….............49

3.3.1 XRD patterns of Co-Pt films ………………………………………..49

3.3.2 Phase analysis by pole figure measurements ……………………….50

3.4 Magnetic properties and their correlation with structure …………….........53

3.5 Magnetic microstructure ……………………………………………….......57

3.6 Ageing study of the electrolyte ………………………………………......59

4 Co-Pt nanowires within alumina templates ……………………………………65

4.1 Influence of the deposition potential on morphology and composition ………65

4.2 XRD in the as-deposited state ………………………………………………...68

4.3 Magnetic properties and their correlation with deposition potential …………69

4.4 Temperature dependent study in the as-deposited state ………………………73

5 Co and Co-Pt within polymeric templates ……………………………………………..79

5.1 Electrodeposition of Co using different pretreatment conditions ………….....79

5.2 Electrodeposition of Co-Pt using different pretreatment conditions …………81

5.3 Magnetic properties of Co-Pt within a polymeric template ……………….....85

6 Magnetic properties of rolled-up microtubes ………………………………………….87

6.1 Motivation ………………………………………………………………………87

6.2 Fabrication of rolled-up microtubes ……………………………………………87

6.3 Magnetic measurements ………………………………………………………..90

Summary and outlook …………………………………………………………………95

References ……………………………………………………………………………....99

Publication list…………………………………………………………………………106

Acknowledgements …………………………………………………………………....107

Introduction

This thesis focuses on the magnetic properties of different nanostructured geometries, e.g. thin films, nanowires and rolled-up microtubes. These geometries are sketched in Figure 1. It will be investigated how these different geometries influence the anisotropic magnetic properties of each sample. As magnetic material Co and Co-Pt is used, since both of these materials can exist in *fcc* or *hcp* structure. Depending on the crystallographic structure, different magnetocrystalline anisotropies are expected, which gives an additional freedom to control magnetism. In addition to shape and magnetocrystalline anisotropy the contribution of magnetoelastic anisotropy is examined.

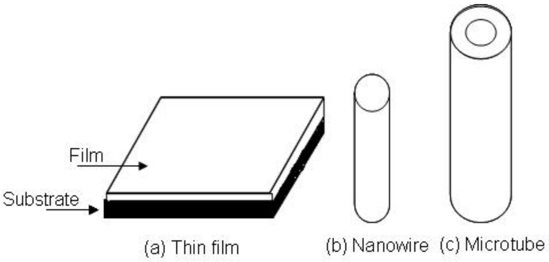

Figure 1: Schematic diagrams of the different geometries examined.

Understanding the correlation between structure, microstructure and shape with magnetic properties in these different geometries is essential to tailor their properties for potential applications. These include permanent magnet components for microelectromechanical systems (MEMS)[1], magnetic patterned media for advanced recording devices[2,3], microjet engines[4] and magnetofluidic sensors[5]. Electrodeposited Co-rich Co-Pt is of particular interest in this respect, as this material can provide hard magnetic properties already in the as-deposited state. Most other hard magnetic materials, like equiatomic CoPt and FePt require a heat treatment, which is disadvantageous to keep the shape of functional nanostructures.

In the present work mostly electrodeposition is used for the growth of the ferromagnetic material. This method had been selected, since it allows to grow complex nanostructures and to tailor both, structure and microstructure, by changing deposition conditions. In this rich playground of applied physics, this thesis will focus on the following fundamentals aspects.

First thin Co-Pt films are examined (chapter 3). For this geometry it is well known that shape anisotropy tends to align magnetization within the film plane. Hence, here the additional influence of magnetocrystalline anisotropy is examined. Magnetocrystalline anisotropy as an intrinsic property depends on the crystallographic structure, which is expected to differ between *fcc* and *hcp* structure. It will be shown, that in particular for highly textured films dedicated diffraction methods are required for distinguishing both phases having almost identical lattice spacing. In order to understand the anisotropic magnetic properties, it is of equal importance to probe the alignment of the crystallite's easy axes. It has been reported by Zana and Zangari[6] that, effective perpendicular anisotropy in thin films can also be enhanced by growing a columnar-type microstructure with magnetically decoupled columns in such a way, that the effective shape anisotropy of the columns adds up with the magnetocrystalline anisotropy. Since electrodeposition is used for film growth, this analysis will include a correlation of the observed properties with the specific growth parameters.

As second model system arrays of ferromagnetic nanowires are examined. In chapter 4 it will be shown how Co-Pt nanowires with a diameter of 70 nm can be prepared by filling anodic alumina templates by electrodeposition. For nanowires one expects that their shape results in a preferable alignment of magnetization along the wire axis. For this system it will be shown that the magnetocrystalline anisotropy associated with the different crystallographic structures of Co-Pt allows tuning the magnetic properties. A systematic variation of deposition conditions will be used to control composition and aspect ratio of the Co-Pt nanowires, which results in a large variation of their magnetic properties. In order to understand the influence of magnetocrystalline anisotropy in detail, temperature dependent measurements will be used.

In order to obtain a further reduction of the nanowire's extensions, diblock copolymer templates with a pore diameter of about 8 nm will be used (chapter 5). Approaches to fill these templates with Co and Co-Pt are given. These templates offer an attractive route to fabricate nanoscaled structures, since they spontaneously form a range of well-defined, well-ordered structures including spheres, cylinders and lamellae[7]. For this template system the focus will be on the limits to scale electrodeposition to small dimensions. It is analyzed why it is difficult to obtain a regular filling of these nanotemplates. The origin of the complex magnetic nanostructures is analysed and consequences for the effective magnetic anisotropy are given.

Finally, in chapter 6, the magnetic properties of Au/Co/Au rolled-up microtubes are investigated. It will be shown how rolled-up semiconductor[8,9]/magnetic[10,11] tubes can be realized by the roll-up of strained layer systems. The magnetic properties of Au/Co/Au films have been compared with the corresponding rolled-up microtubes. This will be discussed with respect to shape and magnetoelastic anisotropy.

Chapter 1

Fundamentals and background

Ferromagnetic nanostructures like thin films and nanowires with high magnetic anisotropy and high coercivity are of interest in various applications including magnetic patterned media for advanced recording devices and magnetic actuators for microelectromechanical system (MEMS). Co-rich Co-Pt alloys are of particular interest, as they can provide high coercivity due to the high anisotropy induced by the incorporation of Pt in the hexagonal close-packed (hcp) phase of Co. The first part of this chapter discusses the different types of anisotropy, electrodeposition of binary alloys, the phase diagram and magnetic properties of CoPt films prepared by other techniques in comparison to electrodeposition. The next part deals with the self-assembly of porous media and Co-Pt nanowires, including a literature review on alumina and diblock copolymer templates, crystal structures and magnetic properties of Co-Pt nanowires.

1.1 Different types of magnetic anisotropy

Magnetic anisotropy in a magnetic material can originate from different mechanisms:

1) Magnetocrystalline anisotropy (depends on crystal structure)
2) Shape anisotropy (depends on shape of the grains and the whole sample)
3) Magnetoelastic anisotropy (depends on applied or residual stress)
4) Induced anisotropy (depends on annealing, irradiation)

1) Among these different types, only magnetocrystalline anisotropy is an intrinsic property of the material. This strongly affects the shape of the hysteresis curves and controls the coercivity and remanence. For a hcp structure, the hexagonal c-axis is the direction of easy magnetization. As an example, the easy and hard axis magnetization

directions for hcp Co are shown in Figure 2. The anisotropy energy E in hexagonal crystals can be given by:

$$E = K_0 + K_1 \sin^2\theta + K_2 \sin^4\theta + \ldots \qquad (1.1)$$

Where K_0, K_1 and K_2 are anisotropy constants and θ is the angle between the magnetization vector and the c-axis.

When K_1 is positive and $K_2 > - K_1$, the energy E is minimum for $\theta = 0$, and the c-axis [0001] is the easy magnetization.

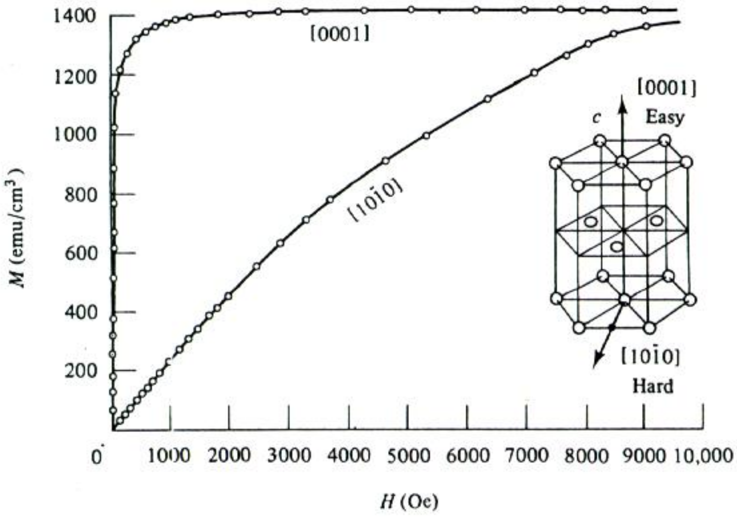

Figure 2: Easy and hard axis magnetization for a hcp Co crystal[12].

The energy E will have a minimum for $\theta = 90°$ if K_1 is negative and $K_2 < |K_1|/2$, or if K_1 is positive and $K_2 < - K_1$. The basal plane is then the easy plane of magnetization. For all other conditions the preferential magnetization direction lies on an easy cone around the c-axis.

The total energy density for a hexagonal crystal in an applied field can be written as the sum of the anisotropy term and the Zeeman term:

$$E_{tot} = K_1 \sin^2\theta + K_2 \sin^4\theta - HM_s \cos(\alpha - \theta) \qquad (1.2)$$

where H is the magnitude of the applied field, M_s is the saturation magnetization at a given temperature and α is the angle between $\vec{H}$ and the c-axis.

The minimum in the anisotropy energy is observed at θ = 0 and 180° for $K_1 > 0$, $K_1+K_2 > 0$. If the external field is applied parallel to the c-axis [0001] (α = 0°), the energy minimum always lies at 0° and thus the magnetization ($M = M_s \cos\theta$) always reaches saturation, as shown in Figure 2.

When the field H is applied along the hard axis (perpendicular to the c-axis α = 90°), equ. 1.2 can be written as:

$$E_{tot} = K_1 \sin^2\theta + K_2 \sin^4\theta - HM_s \sin\theta \qquad (1.3)$$

The magnetization along a hard axis proceeds via the rotation of the magnetization vector from the easy axis to the hard axis. Thus, the projection of the magnetization on to the hard axis ($(M^{\perp} = M_s \sin\theta)$ increases linearly with the field, and the saturation in magnetization is achieved at the field value of the anisotropy field H_A. It is the field required to align the magnetization along the hard axis, which is $[10\bar{1}0]$ for a hcp cobalt crystal (Figure 2). The preferred direction of magnetization can be obtained by minimizing eqn. 1.3.

$$\frac{dE_{tot}}{d\theta} = 2K_1 \sin\theta\cos\theta + 4K_2 \sin^3\theta\cos\theta - HM_s \cos\theta = 0 \qquad (1.4)$$

After simplification equ. (1.4) turns to:

$$H = \frac{2K_1 \sin\theta + 4K\ \ \sin^3\theta}{M_s} \qquad (1.5)$$

The anisotropy field H_A is the field required to align the magnetization perpendicular to the easy axis, i.e., θ = 90°. So from equ. (1.5) it follows that the anisotropy field is given by: $H_A = \dfrac{2K_1 + 4K_2}{M_s}$ (1.6)

2) The second important contribution to the anisotropy comes from the shape or the geometry of the sample. The preference of magnetization to lie in a particular direction in a sample is given by shape anisotropy. Upon magnetizing the sample in a strong

external applied field, positive and negative surface charges develop, forming magnetic dipoles in the sample. The direction of the magnetic field generated by these dipoles is opposite to the magnetization of the sample. The demagnetizing field H_d is strongly influenced by the shape/geometry of the sample. It is given by:

$$H_d = NM \tag{1.7}$$

Where M is the magnetization of the sample and N is the demagnetization factor (depending mainly on the shape of the body)

Equ. (1.7) says that the greater the magnetization of the sample, the more the field from the surface poles opposes the external field. Thus for soft magnetic materials, where a large magnetization results from a relatively weak external field, the internal field can be much less than the applied field even if the demagnetization factor N is very much less than unity. Shape effects become important with the aspect ratio of the sample.

A magnetic thin film which is equivalent to an infinite sheet has $N \sim 1$, if it is magnetized normal to its surface, and $N \sim 0$, if it is magnetized in-plane.

For a magnetic nanowire which can be treated as an infinitely long cylinder the demagnetization factor $N \sim 0$, if it is magnetized along its length, and $N \sim ½$ if it is magnetized perpendicular to its length.

Due to this lower N, it costs less energy for a thin film to magnetize in-plane and for a nanowire to magnetize along its long axis, because then there are no surface poles to cause opposing fields.

For a polycrystalline sample, which has its grains oriented in all possible directions, there exists no crystal anisotropy. If it is additionally spherical, the magnetic moments average out and cancel one another. However, if the crystal is non-spherical, it is easier to magnetize it along the long axis compared to the short axis, due to the smaller demagnetizing field along the long axis.

3) Magnetoelastic effect arises from the spin-orbit interaction. The spin moments are coupled to the lattice via the orbital electrons. If the lattice is changed by strain the distances between the magnetic atoms is altered and hence the interaction energies are changed. This produces magnetoelastic anisotropy.

The magnetoelastic anisotropy constant (K_σ), which is derived from the magnetoelsatic energy, involves the magnetostrictive strain and the applied stress, is given by:

$$K_\sigma = \frac{3}{2}\lambda_{si}\sigma \qquad (1.8)$$

Where λ_{si} is magnetostrictive strain measured at magnetic saturation, σ is the applied stress

The way in which a material responds to stress depends only on the sign of the product of the λ_{si} and σ; a material with positive λ_{si} under tension behaves like one with negative λ_{si} under compression.

The axis of stress is an easy axis if $\lambda_{si}\sigma$ is positive. If this quantity is negative, the stress axis is a hard axis and the plane normal to the stress axis is an easy plane of magnetization.

4) Induced anisotropy is not important here.

1.2 Electrodeposition

1.2.1 Fundamentals

In general, when a metal is immersed in a solution containing its own ions, some surface atoms in the metal lattice do become hydrate and dissolve into the solution. At the same time ions from the solution are deposited on the electrode. The rate of these two opposing processes is controlled by the potential difference at the metal-solution interface. The specific potential at which these two reaction rates are equal, is called standard potential.

There are three main steps in the cathodic deposition of alloys or single elements:

1. Ionic migration (Hydrated ions in the electrolyte migrate(s) towards the cathode)
2. Electron transfer (Loss of hydrated shell from the ion in the double layer and the individual ion is neutralized and absorbed)
3. Incorporation (Adsorbed ion wanders to a growth point on the cathode and is incorporated in the growing lattice)

The equilibrium potential at a metallic electrode that is in equilibrium with its ions is given by the well known Nernst expression:

$$E = E^0 + \frac{RT}{vF}\ln a_{ion} \qquad (1.9)$$

E reversible electrode potential

E^0 standard oxidation electrode potential

v valence

F Faraday charge

a_{ion} ionic actual activity

Deposition occurs as an irreversible process, which is given by:

$$E^D = E^0 + \frac{RT}{vF}\ln a^{v^+} + \eta \qquad (1.10)$$

Where η is the overpotential and given by the difference of equ. (1.11) and (1.10) and a^{v^+} is the activity value of the cation being deposited. The overpotential η is the extra potential needed to maintain the deposition going at the given desired rate suitable to the nature and properties of the cathode film

1.2.2 Electrodeposition of alloys

Electrodeposition of alloys is almost as old an art or science as is the electrodeposition of individual metals. The contribution by C. L. Faust in the previous (1974) edition of Modern Electroplating[13] draws attention to a number of fundamentally important points regarding alloys and their properties. Many of these are relevant today as they were nearly three decades ago. It is stated that the properties of alloy deposits are superior to those of single-metal electrodeposits. It is further asserted that, relative to the single-component metals involved, alloy deposits can have different properties in certain composition ranges. They can be denser, harder, more corrosion resistant, superior in magnetic properties and in antifriction applications.

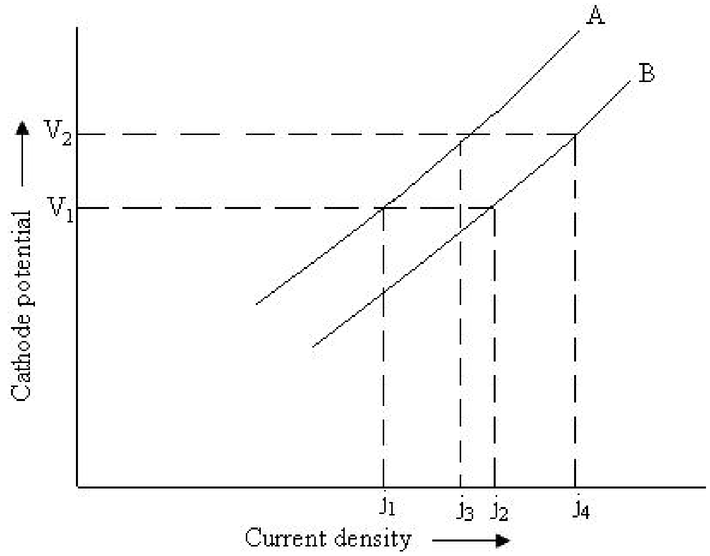

Figure 3: Polarization curves for the deposition of alloys[14].

Electrodeposition of alloys requires the codeposition of two or more metals. In other words their ions must be present in an electrolyte that provides a cathodic film where the individual deposition potentials can be made to be close or even the same. Figure 3 depicts typical polarization curves, that is, deposition potential as a function of current density for two metals (A and B; corresponding to curves A and B in Figure 3) separately. From such curves it is possible to infer that from a deposition bath that contains both metal ions it would be, at potential V_2, possible to codeposit the two metals A and B in the ratio j_3/j_4.

The standard electrode potential of two metals should not be far apart for the deposition. The difference can be eliminated by modifying the activity values or by adding complexing agents. The standard reduction potentials of cobalt and platinum are -0.287 V and +1.19 V vs. the saturated hydrogen electrode (SHE), respectively. In order to bring the potentials of cobalt and platinum close enough to achieve the co-deposition, ammonium tartrate, and ammonia solution or other complex agents are added to a form complex with metal ions in the aqueous solution[15]. The deposition of metals is accompanied by hydrogen evolution, so during alloy plating hydrogen is the codepositing element. Alloy plating of two metals makes it into the process of production of hydrogen and two more metals. The evolution of hydrogen during the electrodeposition of an alloy has a significant effect on the polarization and composition of the deposited alloy. If a significant amount of hydrogen is evolved, the potential of the cathode during the alloy deposition may be almost totally determined by the hydrogen evolution reaction. Under such condition an increase in potential will increase the amount of hydrogen evolution, resulting in a poor efficiency for alloy deposition with a minor change in the composition of deposited alloy.

1.3 Co-Pt thin films

1.3.1 Background and applications

Magnetic films with strong perpendicular magnetic anisotropy (easy axis perpendicular to the film plane) attract wide interest as viable media for perpendicular recording systems[16,17,18], as well as for patterned magnetic media[2,3,19,20]. In order to obtain recording densities in the order of $10^2 - 10^3$ Gbits/inch^2, the bit dimensions must be of the order of 80-25 nm. For perpendicular recording systems this requires both a small grain size and a high anisotropy. A high anisotropy is required to overcome the superparamagnetic limit in smaller grains caused by thermal instability. To overcome this thermal instability the ratio of the magnetic energy K_uV (K_u is the uniaxial magnetic anisotropy and V the grain volume) to thermal energy kT (k is Boltzmann's constant and T the temperature) should be larger than 25[12]. Binary alloys and intermetallic compounds of the Co-Pt and Fe-Pt systems are main focus of study for this purpose. These materials exhibit a very high anisotropy in the range of 10^5 to 10^7 J/m^3 [16,17,21,22].

1.3.2 Phase diagram of the Co-Pt system

The Co-Pt phase diagram is characterized by the A1 phase in the range of complete solid solubility at high temperatures. The crystal structure of the A1 phase is disordered face-centerd-cubic (fcc) over the whole solid solution range, in which Co and Pt atoms statistically occupy the crystallographic sites. The high temperature fcc phase is practically useless for permanent magnetic applications because a cubic phase in general does not offer a sufficiently high magnetic anisotropy. For temperatures around 1100 °C and on the Co-rich side, the system orders ferromagnetically but stays atomically disordered. At a relatively low Pt concentration (Pt ~ 23 at. %), it transforms into the hcp structure[23]. An ordered Co_3Pt phase ($L1_2$) has been reported to occur[24,25] at a temperature of approximately 450 °C. Below 825 °C, a disorder-order transition results in the transformation of the fcc structure to the $L1_0$ structure and a $CoPt_3$ phase ($L1_2$) on the Pt rich side occurs with a maximum ordering temperature of 750 °C. The $L1_0$ phase is an ordered superstructure with Pt at the 000 and ½ ½ 0 sites and Co at the ½ 0 ½ and 0 ½ ½ sites. It is a magnetically hard phase with a very high magnetocrystalline anisotropy field ($\mu_0 H_A \approx$ 13 T at room temperature) and an easy axis of magnetization along the c-axis.

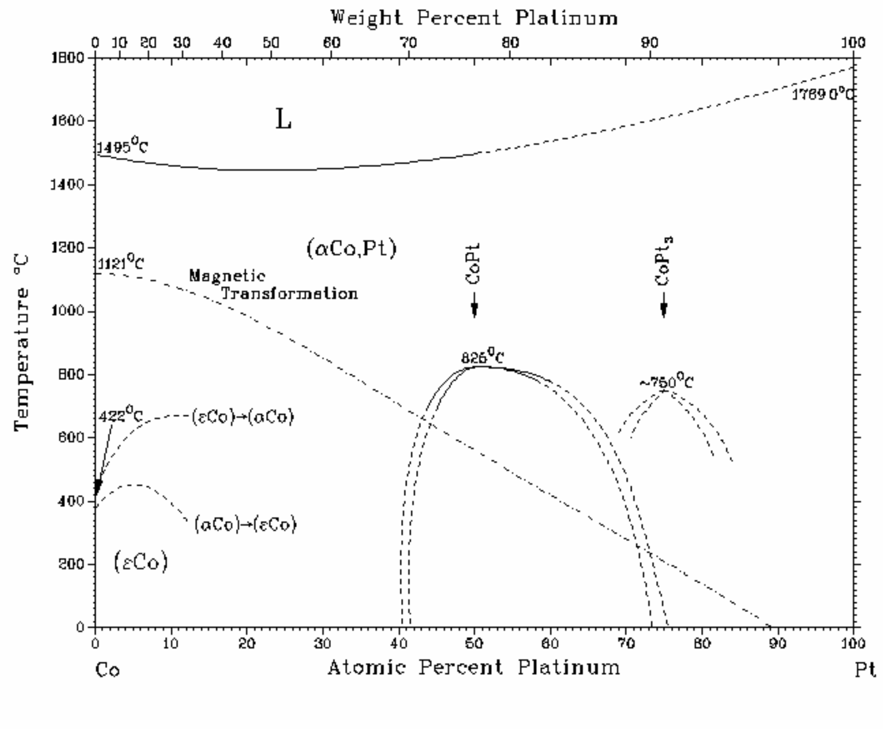

Figure 4: Phase diagram for CoPt alloy[23].

1.3.3 Structure and magnetic properties of $L1_0$ and Co-rich Co-Pt films

Intrinsic properties

$L1_0$ Co-Pt films can be prepared by different deposition techniques like sputtering[22,26,27,28,29], pulsed laser deposition (PLD)[30] and electron beam evaporation[31]. The equiatomic Co-Pt alloy is characterized by the disordered fcc structure in the as-deposited state. An annealing treatment is necessary to assist a formation of the long range chemical ordering[32,33]. By controlling thickness, composition and annealing conditions and/or depositing a proper underlayer $L1_0$ Co-Pt films can be obtained. The lattice parameters for $L1_0$ Co-Pt films[22] obtained at a substrate temperature of 704 °C are a = 3.802 Å, c = 3.698 Å, and c/a = 0.973 which are similar to bulk samples[34]. Agostinelli *et al.*[30] have studied the effect of annealing time on the crystallographic ordering of $Co_{50}Pt_{50}$ films on a Pt underlayer. The $L1_0$ phase is detected after annealing at 640 °C for 120 min. For longer annealing duration the reduction in the reflections of the $L1_0$ phase is due to a thermal diffusion between Pt and CoPt layers that causes a reduction of crystallographic order. The saturation magnetization (M_s) of ~ 1.0 to 1.13 T and the anisotropy of ~ $3x10^6$ J/m^3 for $Co_{1-x}Pt_x$ (40 < x < 60 at. %) films has been reported by Barmak *et al.*[22]. Visokay and Sinclair[29] have reported the direct formation of the ordered $L1_0$ structure at a substrate temperature above 540 °C with an anisotropy constant of ~ $2.8x10^6$ J/m^3. Zeng *et al.*[28] have found that suppressing grain growth promotes an increase of a (001) texture in very thin (10 nm) films of $Co_{50}Pt_{50}$.

In addition to the equiatomic Co-Pt, Co-rich Co_3Pt[25,35] and $Co_{80}Pt_{20}$[36,37,38] films with a magnetic anisotropy constant in the order of 10^6 J/m^3 were achieved by various deposition techniques. Harp *et al.*[35] have studied the structure transition in the Co_3Pt alloy (hcp to fcc) with respect to the deposition temperature. There is a transition from hcp to fcc near 700 K, as observed in bulk Co-Pt alloys for a Pt concentration up to 20 at. %[23]. Howard[36] has reported that $Co_{80}Pt_{20}$ films deposited at 126 °C exhibit the hcp structure with a strong (002) texture. Yamada *et al.*[25] have shown that the origin of the large magnetic anisotropy constant in Co_3Pt is due to the magnetocrystalline anisotropy of the Co_3Pt disordered phase and an interface-induced magnetic anisotropy in the Co_3Pt

ordered phase. It has been reported by several groups that the magnetic anisotropy depends on the Pt concentration in CoPt alloys and reaches a maximum at a Pt concentration of 25-30 at. %[25,39,40]. Pandey *et al.*[37] have reported that the anisotropy of Co-rich Co-Pt films can be increased by improving their (002) texture by using a Ru underlayer.

Extrinsic properties

Coercivity values of 0.28 to 1.5 T have been achieved in $L1_0$ Co-Pt films[30,32,41]. Ristau *et al.*[32] have reported that the increase in coercivity of $L1_0$ CoPt films is due to defects in the magnetic material, such as grain boundaries and phase boundaries, which form pinning sites that impede the movement of magnetic domain walls. In $L1_0$ ordered CoPt the magnetic easy axis corresponds to the tetragonal c-axis. Thus the boundaries between the adjacent c-axis variants are expected to be effective pinning sites because of the 90° change in the magnetic easy axis that occurs at this boundary. Agostinelli *et al.*[30] have studied the variation of coercivity as a function of annealing time for $Co_{50}Pt_{50}$ films prepared by PLD. They found that the coercivity increases with the annealing time which could be due to the increase of the amount of the $L1_0$ phase. A high uniaxial anisotropy (K_u), which is essential for a high coercivity (H_c), is mostly dependent on the degree of long-range order in $L1_0$ alloys[42]. The coercivity of $L1_0$ Co-Pt films prepared by various deposition techniques and annealed at different temperatures are summarized in Table 1.

Table 1: Coercivity of $L1_0$ Co-Pt films prepared by various deposition techniques.

Deposition technique [Ref.]	Annealing temperature	Film thickness	Coercivity
PLD [30]	600° C	-	0.28 T
Sputtering [32]	700° C	10 nm	1.53 T
Electrodeposition [45]	650° C	5 µm	1.42 T

The thickness dependence of the coercivity (H_c) and of the magnetization at 5 T for $Co_{49}Pt_{51}$ films annealed at 800 °C is shown in Figure 5[26]. The low coercivity might result from a smaller amount of ordered phase in the thin film samples because of the shortage of nucleation sites. For Co_xPt_{1-x} films (x = 40, 45 and 50 at. %) Tsoukatos *et al.*[27] reported that the microstructure of the as-sputtered films consists of fine grains which grow substantially in size after annealing at 650 °C. It was found that the average grain size also increases with thickness, which results in an increased coercivity. As the grain size observed in these films in the as-deposited state is well below the critical size value $D_c \sim 400$ nm, which leads to a reduction in coercivity for $D < D_c$ because of thermal effects ($H_c \sim [1-(D_c/D)^{3/2})]$)[12]. For $Co_{50}Pt_{50}$ films Barmak *et al.*[41] have also reported an increase in coercivity with grain size and annealing temperature. This increase in coercivity is due to the formation of the ordered $L1_0$ phase. Ariake *et al.*[38] reported that a high Ar gas pressure deposition of Co-Pt films generates physically isolated grains and magnetically weekly coupled grains, this difference in microstrucure, resulting in high coercivity.

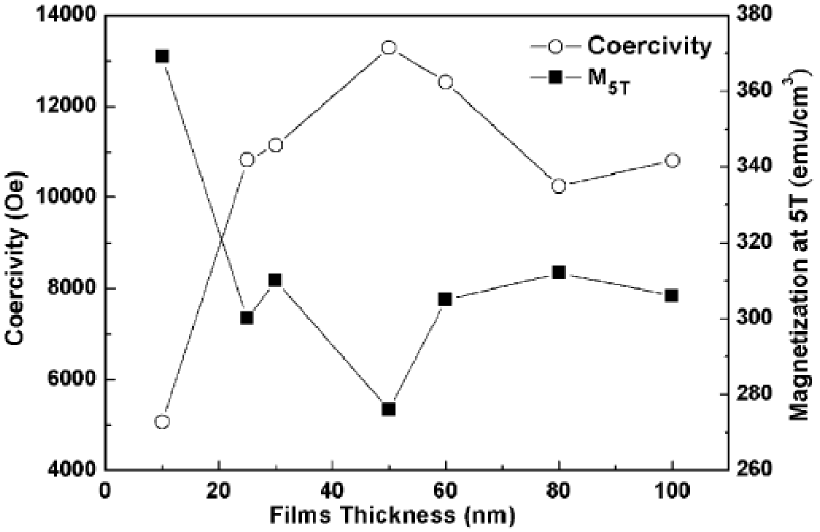

Figure 5: Thickness dependence of coercivity and magnetization of $Co_{49}Pt_{51}$ films annealed at 800 °C[26].

The coercivity obtained for the Co-rich $Co_{72}Pt_{28}$ alloy is 0.55 T[37] in the out-of-plane direction. This high coercivity H_c may be attributed to the large magnetic anisotropy of the magnetic film, since $H_c \propto 2K_u/M_s$, where K_u is the uniaxial magnetic anisotropy and M_s the saturation magnetization of the magnetic layer. Howard[36] has studied the influence of different underlayer (Cr or W) on the magnetic properties of Co-rich Co-Pt films. A deposition of the $Co_{80}Pt_{20}$ films on W causes a significant increase in coercivity (0.24 T) compared to the Cr underlayer, which could be due to the formation of βW (metastable phase of W) or an hcp phase of Co_3W.

1.3.4 Electrodeposited Co-Pt films

Electrodeposited equiatomic CoPt films have also been reported by several groups[15,43,44,45,46]. Like sputter deposition or PLD of Co_xPt_{1-x} films, these electrodeposited films are also in a disordered fcc phase. A subsequent heat treatment is required to obtain the ordered $L1_0$ phase. In order to take advantage of the magnetic properties of these alloys, it is essential to control the film composition and structure. In particular it is important to identify the conditions how to deposit near-stoichiometric, single phase films. Different electrolyte systems have been used by different groups for depositing $L1_0$ and Co-rich Co-Pt films (see Table 2). Wang *et al.*[15] have reported that the composition of Co-Pt films can be controlled by the metal ion ratio in the plating bath and by the applied current density. The as-deposited films have a disordered fcc structure. By annealing above 600 °C they transform to the $L1_0$ ordered structure. After annealing at 700 °C a coercivity of about 652.6 kAm^{-1} at a film composition of 51.8 at. % Pt has been achieved in these films. Thick films (~ 5 µm) of Co-Pt reported by Wu *et al.*[45] contain A1+ $L1_0$ phases. The size and the volume fraction of the $L1_0$ ordered phase increase with annealing time. After annealing at 650 °C for 2.5 hours the films show a nearly single-phase hysteresis loop with a large coercivity of 1.42 T and a high remanence ratio (M_r/M_s) of 0.88, which could be due to the strong magnetic coupling between the A1 phase and the $L1_0$ ordered phase.

Table 2: Electrolyte systems used for the deposition of Co-Pt films.

Electrolyte system	pH	Bath temperature	Reference
x M $CoCl_2.H_2O$ 0.05-x M H_2PtCl_6 2x M $(NH_4)_2C_4H_4O_6$ 2x M $NH_3.H_2O$ Where x = 0.005 and 0.015	9.5	60 °C	15
50 mM $CoSO_4$ 10 mM $Pt(NO_2)_2(NH_3)_2$ 0-100 mM $(NH_4)_2C_6H_6O_7$ 0-100 mM $C_6H_5Na_3O_7$ 1-150 mM $(NH_4)_2SO_4$	8	50 °C	43
3-4 mM $Co(NH_2SO_3)_2$ 2 mM $Pt(NH_3)_2(NO_2)_2$ 20 mM $(NH_4)_2C_6H_6O_7$ 0.2 mM NH_2CH_2COOH	8	60 °C	44
0.1 M $Co(NH_2SO_3)_2$ 0.01 M $Pt(NO_2)_2(NH_3)_2$ 0.1 M $(NH_4)_2C_6H_6O_7$ 0.1 M NH_2CH_2COOH 0.1 M $NaH_2PO_2.H_2O$	8	65 °C	6
12.8-55 mM $CoSO_4.7H_2O$ 3.5 mM $Pt(NH_3)_2(NO_2)_2$ 0.94 M Na_2CO_3 0.85 M $NaCH_3CO_2$ 0.47 M $C_6H_{15}NO_3$	5	70 °C	51

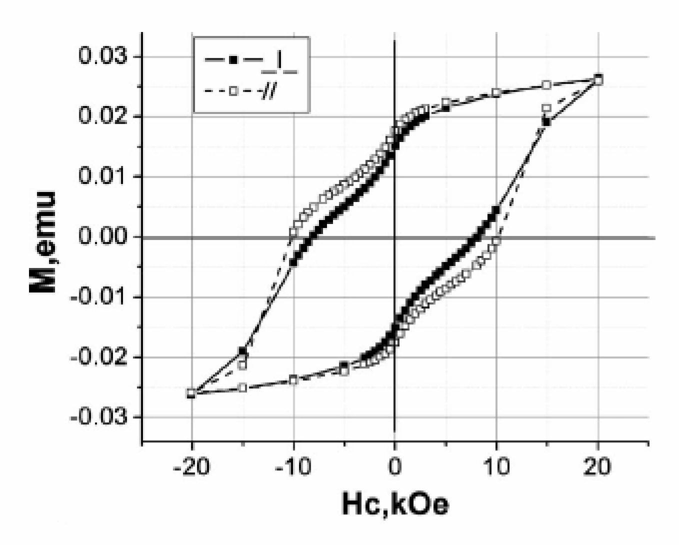

Figure 6: Room temperature hysteresis loops of an annealed (at 700 °C for 4 h) electrodeposited CoPt film[43].

The hysteresis loop of an equiatomic CoPt film[43] (Pt ~ 42 - 48 at. %) is displayed in Figure 6. The coercivity increases significantly after annealing. This increase in coercivity is expected due to the transformation of the disordered fcc phase (A1) to the $L1_0$ phase. The shape of the hysteresis shows the presence of two phases (A1 and $L1_0$) in the film. This behavior could be due to the presence of a low coercive phase with a coercivity of about 0.2 T, and the formation of the highly coercive CoO fcc phase. The formation of fcc CoO can be attributed to the penetration of some air into the annealing chamber, which contained argon. Coercivity, remanence and squareness (M_r/M_s) of up to 0.8 - 1.0 T, 0.32 - 0.37 T, and 0.67 - 0.70 were observed for these films.

For electrodeposition of Co-rich Co-Pt films, Cu and Ru buffers are generally preferred as seed layer, due to the lattice matching of the substrate and the film. Electrodeposition of Co-rich Co-Pt films exhibit high coercivity and perpendicular magnetic anisotropy (PMA) in the as-deposited state[6,47,48,49,50]. Zana and Zangari[6] have reported that Co-Pt films on a Cu (111) seedlayer with hcp phase can be obtained by optimizing the growth conditions. Cu (111) seedlayers stabilize the hcp matrix, due to the almost perfect lattice matching between the Cu (111) plane and the basal plane of the hcp CoPt phase.

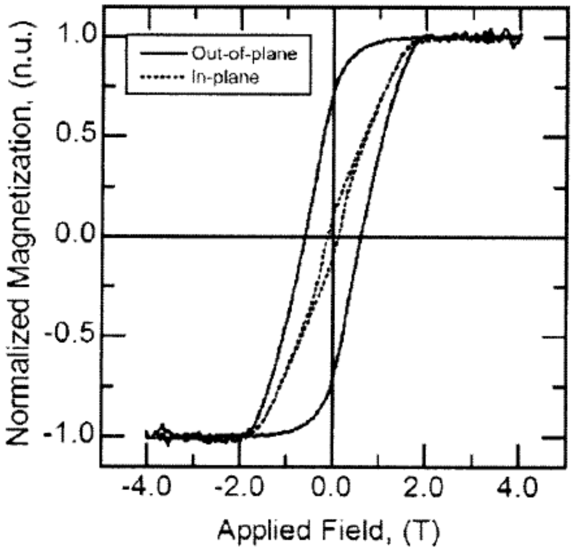

Figure 7: Hysteresis loops of an electrodeposited Co-rich Co-Pt film measured at room temperature[6].

A high coercivity is observed in these films due to the Cu (111) substrate which promotes a large out-of-plane magnetic anisotropy (shown in Figure 7) due to the combined effect of the growth of an hcp phase with the c-axis perpendicular to the substrate and the columnar microstructure. Zana and Zangari[49] have reported a saturation magnetization (M_s) of 0.97-1.04 T and a magnetic anisotropy of ~ 1×10^6 J/m^3 for $Co_{80}Pt_{20}$ films. A coercivity of about 0.6 T and a squareness (S) of 0.7 is achieved for the $Co_{80}Pt_{20}$ films deposited at a current density of 50 mA/cm^2 on a Cu (111) seed layer[6]. This high coercivity at this current density could be due to the high fraction of hcp phase present in the film. Eagleton *et al.*[51] have reported that the composition and the crystal structure of the Co_xPt_{1-x} films depend on the solution composition and the deposition potential. These Co_xPt_{1-x} films are fcc for $x < 0.52$ at. % and deposited below -0.65 V, while films with $x > 0.76$ at. % and deposited at a more negative potential (-0.85 V) exhibit the hcp phase. Pattanaik *et al.*[48] have reported hcp Co-Pt films irrespective of deposition current density. However, the deposition current density plays an important role in optimizing microstructure and hard magnetic properties of Co-rich Co-Pt films. Ru(0001) provides an appropriate interface for an oriented growth, resulting in excellent magnetic properties. The coercivity and the squareness reported for these films are about 0.45 T and ~ 0.9, respectively[48].

1.4 Nanostructuring for magnetic materials

1.4.1 Nanolithography

Nanolithography is a traditional method to produce periodic arrays of nanoscale magnetic particles, dots and wires[52,53]. This refers to the fabrication of nanometer-scale structures, meaning patterns with at least one lateral dimension between the size of an individual atom and approximately 100 nm. However this method is comparatively cumbersome and not suitable for large-area production.

1.4.2 Self-assembly of porous media

Magnetic nanostructures can be fabricated by using the self-assembly of porous media[54]. This approach is promising for large-area nanopatterning with high aspect ratio, which is usually difficult to achieve by conventional lithography. Track etched polymer membranes[55,56], block copolymer membranes[57,58] and porous anodic alumites[54] are some representative templates. These membranes enable to make fibrils of uniform diameter of a few tens of nm and with an aspect ratio of 10^3. In choosing a template material for generating nanowires, several factors, as e.g. pore size, pore density and pore shape, must be taken into account and eventually optimized.

A diblock copolymer is a linear-chain molecule consisting of two sub-chains joined covalently to each other. One of the sub-chains is made of monomers of type A and the other of type B (Figure 8 (a)). Diblock copolymers (diBC) can self-assemble into well defined, ordered arrays of nanoscopic domains ranging from spheres to cylinders to lamellae as shown in Figure 8 (b) to (d), depending on the degree of polymerization (N), segment-segment interaction parameter (χ) and the volume fraction (f) of the components[7,59].

The calculated phase diagram of diblock copolymers is shown in Figure 9. The simplest of these ordered microphases is the lamellar (L) phase in which the A and B monomers separate into A-rich and B-rich lamellae. It is observed to occur when the volume fractions of two monomers are comparable. If the volume fraction of one monomer becomes sufficiently greater than that of the other, the minority component is observed to form cylinders which pack in a hexagonal arrangement forming the hexagonal (*H*) phase.

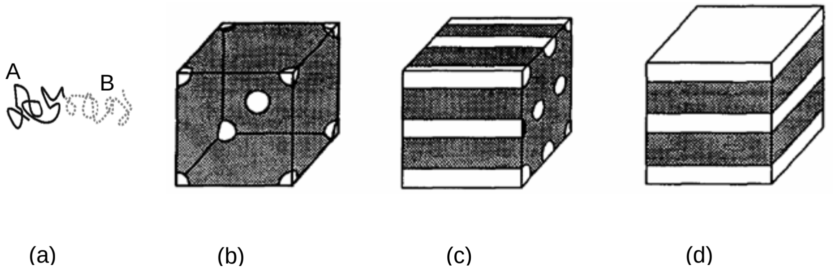

Figure 8: Typical architecture of a diblock copolymer, where A and B correspond to two different polymer blocks (a). Different morphologies found in diblock copolymer templates: spherical (b), cylindrical (c) and lamellar (d)[7].

With further increasing asymmetry in volume fraction (*f*), the minority fraction forms spheres which then pack in a body-centered cubic arrangement, the cubic (*C*) phase. The product χN expresses the degree of microphase separation (where χ is the interaction parameter between the blocks and N is the degree of polymerization). χN and the block volume fraction f completely determine symmetry and the dimensions of microphase separated structure and are used for the construction of block copolymer (BC) phase diagrams (Figure 9). The phase diagram for symmetric *di*BC ($f = 0.5$) at $\chi N \ll 10$, is characterized by the disordered state (*D*), which occurs at high melt temperatures, when the interactions between dissimilar monomers are weak. As f appreciably deviates from 0.5, the flat interface of the lamellar structure can not be maintained by stretching the major block[60]. It becomes energetically more favorable to form curved interfaces. The interfacial curvature is changed stepwise upon the transition from one morphology to another. Also, in the intermediate segregation limit (region of

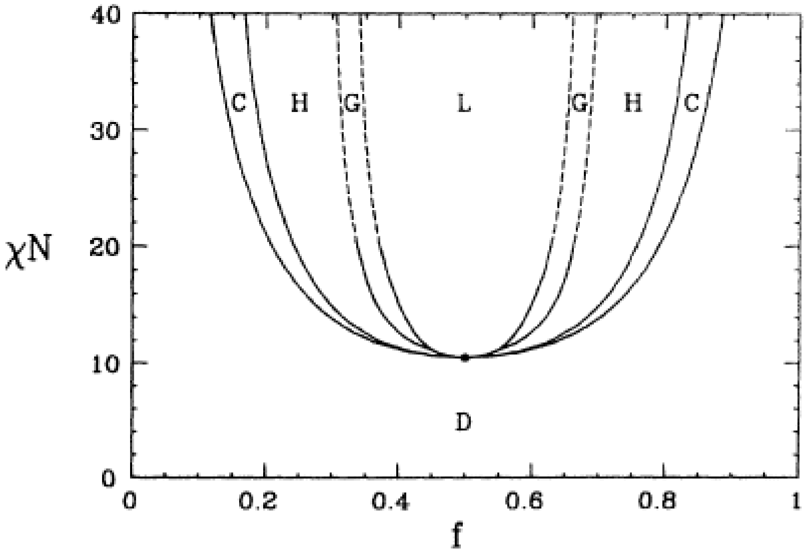

Figure 9: Calculated phase diagram of diblock copolymers showing regions of stability for disordered (*D*), lamellar (*L*), gyroid (*G*), hexagonal (*H*) and cubic (*C*) phases[61].

χN between 10.5 and ≈ 50), increase of the *di*BC asymmetry results in the following sequence of *order-order transitions* (*OOT*): lamellar (*L*) → bicontinuous cubic (*gyroid*) → hexagonal cylindrical (*H*) → body-centered cubic spherical (BCC *S*) → *disordered* state (*D*).

The interface to a substrate allows further control of the self-organized nanostructure. BC thin films confined by the copolymer-substrate and the copolymer-air (or vacuum) interfaces undergo both surface relaxation and surface reconstruction. It is caused by surface phenomena which induce changes in the periodicity and force one of the blocks to occupy an interface. This property is explored for templating. The preparation of the copolymer templates avoids the strong acid etching conditions necessary for anodizing aluminum and enables a new pathway to the fabrication of nanostructure templates. Different block copolymers such as polystyrene-*block* - poly (4-vinylpyridine) (PS-P4VP)[64], polystyrene-polybutadiene (PS-PB) and PS-polyisoprene (PI)[62], polystyrene (PS) - *block* - poly (methylmethacrylate) (PMMA)[63] have been used for fabricating the templates.

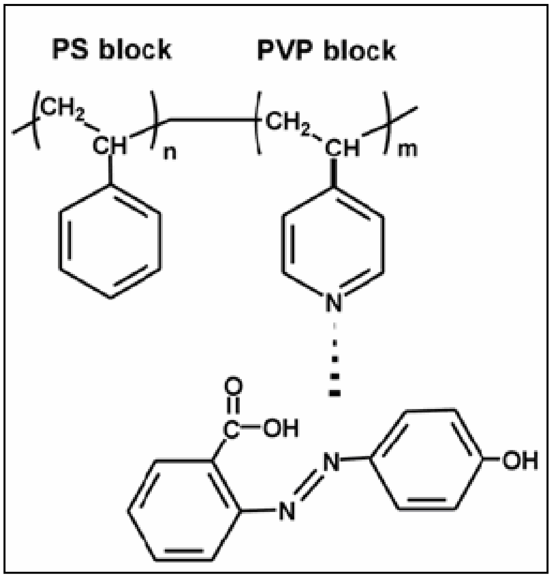

Figure 10: polystyrene *block*-poly (4-vinylpyridine) (PS-b-P4VP) + HABA assemble[64].

An elegant approach to porous bulk materials has been reported by Mäki-Ontto *et al.*[65]. It is based on supramolecular assemblies of a block copolymer and a low molar mass additive, which forms hydrogen bonds with one of the blocks as shown in Figure 10. The additive can be extracted with a selective solvent producing empty channels.

1.5 Co-Pt nanowires

1.5.1 Background and applications

Periodic arrays of magnetic nanowires deposited in self-assembled alumina and diblock copolymer templates have attracted much attention. The arrays have many potential applications in technology, for example in high density magnetic recording and as sensors, and are scientifically interesting because they can be considered as model systems to study interaction processes and magnetic reversal in low-dimensional magnetic structures.

1.5.2 Crystal structure and phase formation

Co-Pt nanowires exhibit fcc, $L1_0$ or hcp structure depending on composition and annealing conditions. The most studied crystal structure is $L1_0$, due to its high uniaxial magnetocrystalline anisotropy that is in the range of $1x10^6$-$5x10^6$ J/m^3 [66,67,68]. The as-deposited nanowires are fcc (Figure 11) corresponding to the disordered phase[69,70,71]. The $L1_0$ phase is formed during annealing at 700 °C. The annealing process contributes to a phase transition of the Co_xPt_{1-x} nanowires: two extra superstructure peaks ((001) and (110)) appear in the XRD pattern (Figure 12).

For Co-rich Co-Pt nanowires fcc ($L1_2$) or hcp phases have been reported[72,73,74]. The XRD for different compositions ($Co_{67}Pt_{33}$, $Co_{84}Pt_{16}$, and $Co_{92}Pt_8$) were analysed[72]. All peaks in the patterns are assigned to the Co_3Pt phase ($L1_2$). Nanowires fabricated by Li and Shen[73] have been reported as hcp for a composition of $Co_{96}Pt_4$, $Co_{92}Pt_8$, and $Co_{87}Pt_{13}$: the identifiable peaks are (100), (002), and (110), the relative intensity of the peaks decreases with increasing Pt content in the nanowires.

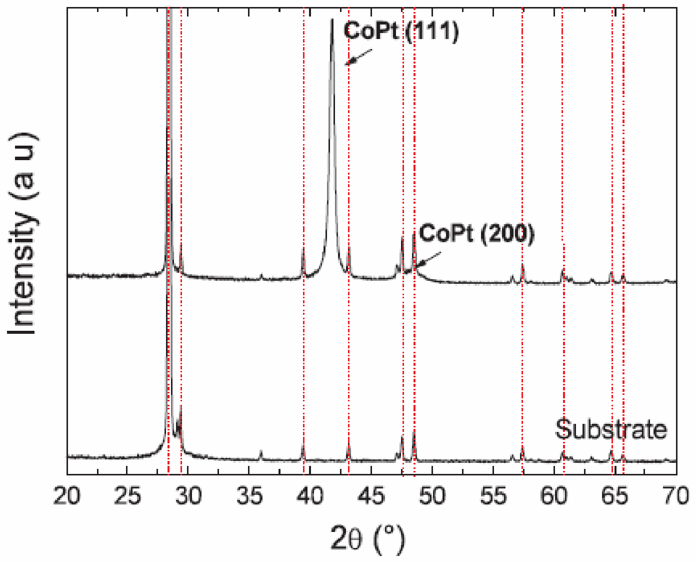

Figure 11: XRD patterns of the nanoporous substrate and the as-deposited Co_xPt_{1-x} nanowires showing a fcc structure[66].

In comparison to the nanowires fabricated by Min *et al.*[72], and Li and Shen[73], the nanowires prepared by Li *et al.*[74] are amorphous in the as-deposited state. After annealing at 700 °C for 20 min in Ar, the diffraction peaks corresponding to the (111), (200), (220), and (311) planes of fcc CoPt appear in the XRD patterns[74].

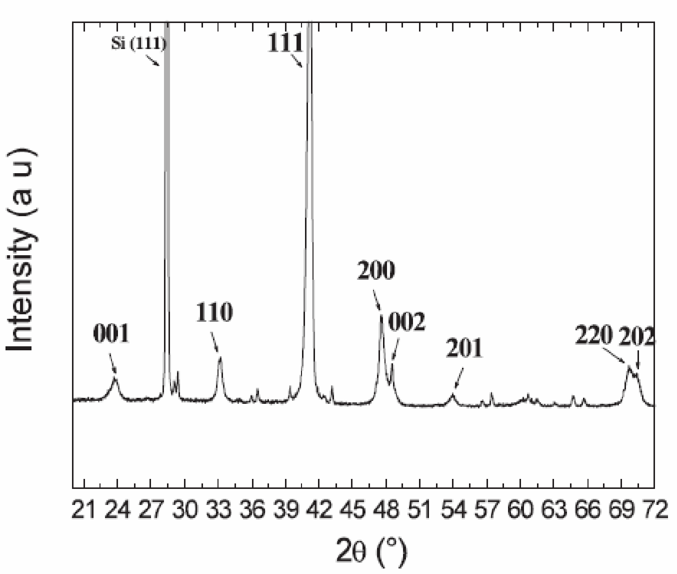

Figure 12: XRD patterns of $Co_{0.47}Pt_{0.53}$ nanowires after annealing at 700 °C[66].

1.5.3 Studies on magnetic properties of CoPt nanowires

Ferromagnetic nanowires exhibit unique and tunable magnetic properties due to their inherent shape anisotropy. The magnetic properties of nanowires have been investigated with the particular emphasis on three areas: (1) Factors that determine the effective easy axis of the wires, (2) magnetization reversal processes within the arrays and (3) magnetic interaction between the wires.

The saturation magnetization reported by Gao *et al.*[71] for $Co_{52}Pt_{48}$ nanowire is 1.15 T, which is close to the bulk value[75]. $L1_0$ ordered arrays of magnetic nanowires exhibit very high coercive fields[66,69,70]. The highest equal to 1.08 T has been obtained with 80 nm diameter $Co_{0.47}Pt_{0.53}$ wires at 300 K[66]. No large difference in the hysteresis loops has been observed between the two directions (Figure 13) although the aspect ratio of the wires is much larger than 10. This is because the $L1_0$ Co_xPt_{1-x} has a very strong magnetocrystalline anisotropy, much higher than the shape anisotropy. The coercivity of

$L1_0$ CoPt nanowire arrays obtained by different groups is summarized in Table 3. Nanowires fabricated by the group of Gapin *et al.*[69], show a coercivity of 0.77 T along the nanowire axis after annealing at 700 °C.

Table 3: Coercivity obtained for $L1_0$ CoPt nanowires.

Composition [Ref.]	Wire diameter (nm)	Coercivity (T)
$Co_{47}Pt_{53}$ [66]	80	1.08
$Co_{54}Pt_{46}$ [67]	80	0.74
$Co_{48}Pt_{52}$ [68]	65	1.0
$Co_{56}Pt_{44}$ [69]	20	0.77

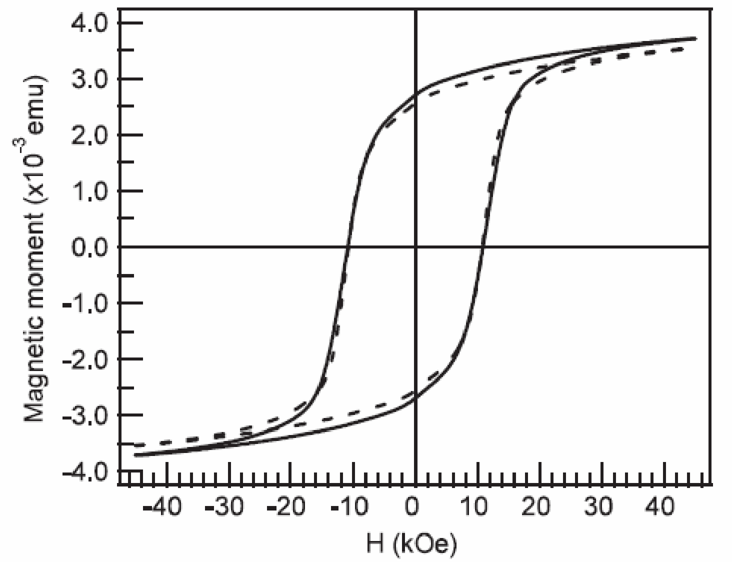

Figure 13: Hysteresis loops for $L1_0$ $Co_{0.47}Pt_{0.53}$ nanowire arrays measured at room temperature with the field applied parallel (solid line) and perpendicular (dotted line) to the wire axis[66].

For Co-rich Co-Pt nanowires, the magnetic properties have been studied for different cobalt compositions and diameters of the anodic alumina templates[72,73,74,76]. Nanowires reported by the group of Min *et al.*[72] exhibit the anisotropy along their axis nanowire with a coercivity of 0.03 T. This low coercivity is ascribed to the polycrystallinity of the nanowires prepared in the anodic aluminum oxide (AAO) template with a larger pore size of 200 nm, which in turns leads to a polydomain structure or deteriorated magnetic properties. The maximum value of coercivity is observed for the $Co_{80}Pt_{20}$ samples[73]. These as-deposited nanowires with 14 nm wire diameter, have much higher coercivity over 0.15 T for the field applied parallel to the wire axis. The magnetic properties of Co-rich Co-Pt nanowires of different diameters are listed in Table 4. For the nanowires reported by Li *et al.*[74], the coercivity and squareness (M_r/M_s) of as prepared nanowires are about 0.17 T and 0.7, when the field is applied parallel to the wire axis (Figure 14). After annealing, the sample exhibits an anisotropy perpendicular to the wire axis, which could be due to the magnetocrystalline anisotropy.

Table 4: Magnetic properties of Co-rich Co-Pt nanowires.

Composition/Phase [Ref.]	Wire diameter (nm)	Coercivity ‖ wire axis (T)	Squareness (M_r/M_s)
$Co_{1-x}Pt_x$ $(0.08<x\leq 0.33)$/fcc [72]	200	0.03	?
$Co_{1-x}PtPt_x$ $(0<x\leq 0.2)$/hcp [73]	14	0.15	0.91
$Co_{0.71}Pt_{0.29}$/Amorphous [74]	50	0.17	0.7
$Co_{1-x}Pt_x$ $x\leq 0.3$/fcc [76]	40	0.02	0.93

In the amorphous sample the shape anisotropy makes the main contribution to the total anisotropy, which favors the magnetization parallel to the wire axis. For polycrystalline samples, the magnetocrystalline anisotropy ($k_\mu \sim 5\text{x}10^5$ J/m^3) is comparable with the shape anisotropy (($\mu_0 M_s^2/4$) ~ $1\text{x}10^5$ J/m^3 for infinite cylinder. As a result, the competition of the two kinds of anisotropy energies results in no perpendicular anisotropy.

It is expected that the structure and the magnetic properties may be significantly enhanced for a reduced pore size of the anodic alumina template[72,77]. The *M-H* curves at different temperatures are also measured to observe the temperature-dependent magnetic properties of Co-Pt nanowire arrays of 40 and 200 nm diameters.[76] The magneto-

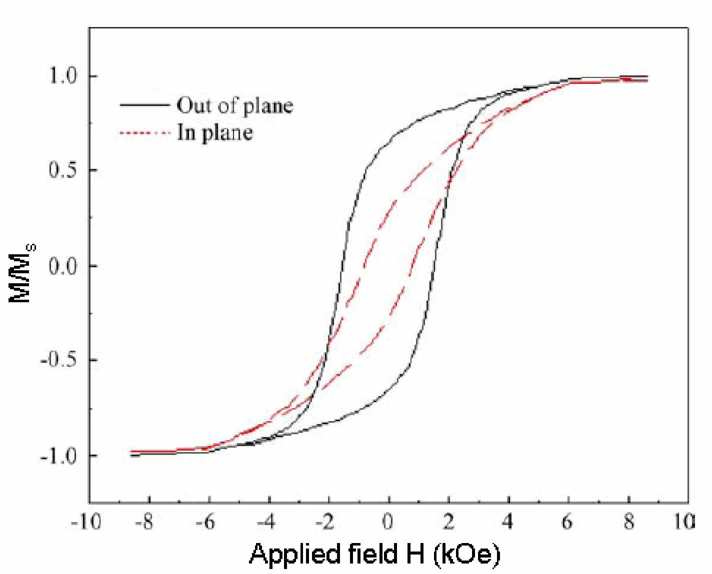

Figure 14: Hysteresis loops of as-deposited nanowire arrays measured at room temperature with an external field applied parallel (out-of-plane) and perpendicular (in-plane) to the nanowire axis[74].

crystalline anisotropy tends to rotate the orientation of the easy axis of magnetization from the high-temperature orientation. This anisotropy of the nanowires decreases with an increase in temperature. For a diameter (*d*) of 40 nm the shape anisotropy becomes prevalent resulting in the orientation of the easy axis along the parallel direction. For d = 200 nm the magnetostatic interaction increases resulting in the alignment of the easy axis perpendicular to the nanowires axis.

Chapter 2

Experimental methods

This chapter deals with the experimental methods used for the preparation and characterization of Co-Pt films, templates and nanowires.

2.1 Electrodeposition set-up for thin films

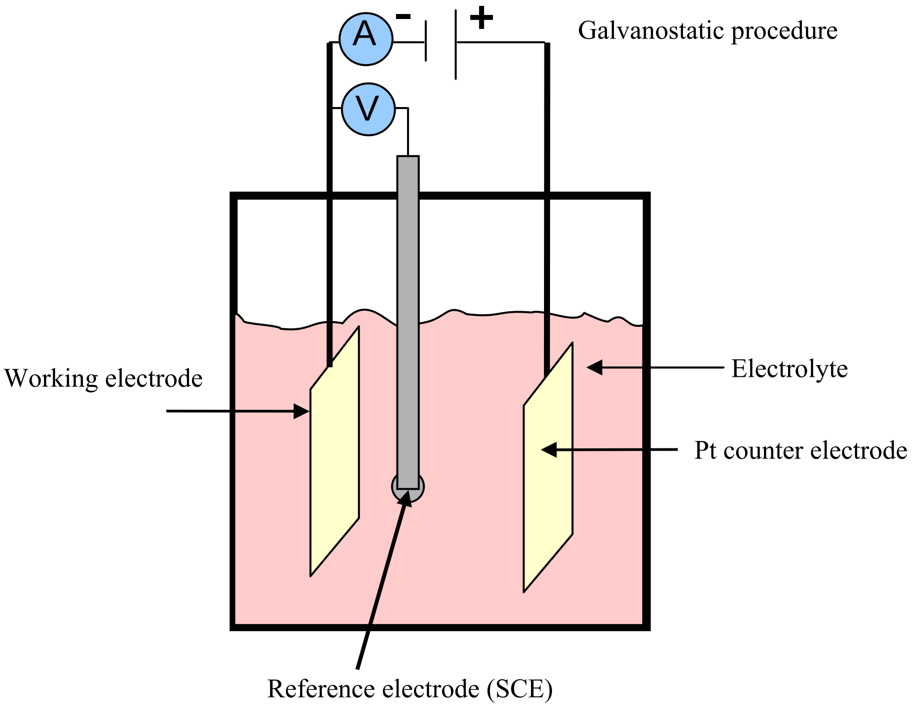

Figure 15: Schematic diagram of the electrochemical cell used for the deposition of Co-Pt films.

The 3-electrodes arrangement of the electrochemical cell is schematically shown in Figure 15. In this study Co-Pt thin films were prepared on 10 mm x 10 mm oxidized Si(100) wafers with a 30 nm thick Cr buffer and a 10 nm thick Au conducting layer as substrates. Both Cr and Au layers were deposited by magnetron sputtering. A Pt sheet was used as counter electrode, a Si wafer with a conducting Au layer and a Cr buffer as working electrode. A saturated calomel electrode (SCE) was used as reference electrode. The potential of the saturated calomel electrode is +0.241 V versus the saturated hydrogen electrode (SHE). Prior to electrodeposition, the substrates have been cleaned two to three times with acetone for 1 to 2 minutes. Current-potential curves were measured in order to characterized the deposition of Co, Pt and Co-Pt. The electrolyte used for the deposition of pure Co contains 20 mM $Co(NH_2SO_3)_2$, 20 mM $(NH_4)_2C_6H_8O_7$ and 0.2 mM NH_2CH_2COOH. The Pt deposition was carried out in an electrolyte containing 2 mM $Pt(NH_3)_2(NO_2)_2$, 20 mM $(NH_4)_2C_6H_8O_7$ and 0.2 mM NH_2CH_2COOH. The electrolyte used for the deposition of the Co-Pt films was amino-citrate based and contained 2 mM $Pt(NH_3)_2(NO_2)_2$, 20 mM $Co(NH_2SO_3)_2$, 20 mM $(NH_4)_2C_6H_8O_7$ and 0.2 mM NH_2CH_2COOH[6]. The electrolyte concentration is diluted in our case, compared to the composition reported by Zana and Zangari[6]. The temperature of the electrolyte was 65 °C and the pH was maintained at 8.0 by using NH_4OH. The films have been deposited for 10 min at current densities varying between 10 and 32 mA/cm^2, controlled by an EG & G model 263 A potentiostate.

2.2 Alumina template fabrication

A 0.32 mm thick aluminum foil (99.999 %) was used as starting material. Prior to electropolishing, Al was recrystallized at 500 °C for 3 hours in Ar atmosphere. The porous alumina was fabricated by a two-step anodization process as described by Masuda *et al.*[54,78]. The electropolished Al was first anodized in 0.3 M oxalic acid at 3 °C for 24 hours by applying a DC voltage of 40 V across the electrodes. This long-time anodization allows the formation of a well-ordered hexagonal pore array and also reduces the number of defects. The mechanical stress at the metal/oxide interface during the oxide growth is proposed to cause the repulsive force between the neighboring pores which promotes the formation of the ordered hexagonal pore array[79]. The thick layer of alumina formed in the first anodization step is removed in a 0.2 M CrO_3 and 0.61 M H_3PO_4 solution. The second step anodization process is carried out also in 0.3 M oxalic acid for 18 to 20 hours at 3 °C. The schematic diagram of the porous alumina template after second anodization is shown in Figure 16.

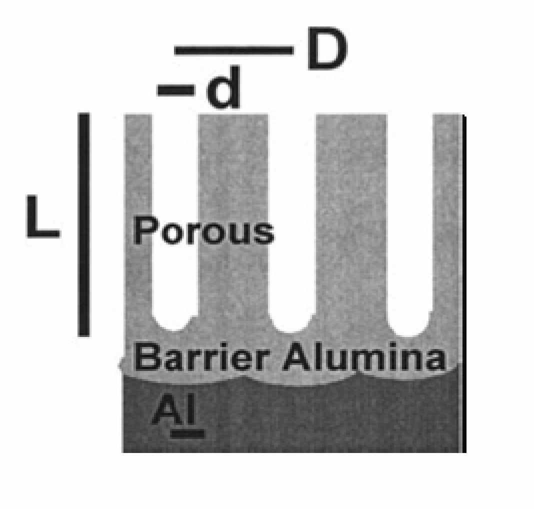

Figure 16: Schematic diagram of the cross-section of a porous alumina template; where d is the pore diameter, D is the interpore distance and L is the channel length[80].

At the bottom there is a thin barrier layer of aluminum oxide. The basic idea concerning the growth of porous aluminum oxide is an equilibrium of two competing mechanisms[79,80], the electric field-enhanced oxide dissolution at the oxide/electrolyte interface and the oxide growth at the metal/oxide interface. The oxide growth is attributed to the migration of oxygen containing ions (O^{2-}/OH^-) from the electrolyte through the oxide layer at the pore bottom. The elementary processes involved in the porous oxide growth are shown in Figure 17.

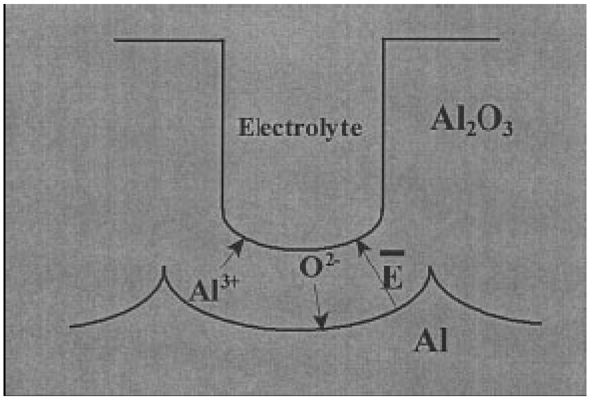

Figure 17: Elementary processes during pore growth[80].

The back side aluminum layer is dissolved in a solution of 0.1 M $CuCl_2.2H_2O$ and 8.26 M HCl. Finally the pore widening process is carried out in 5 wt. % of phosphoric acid. Highly ordered AAO templates with a pore diameter of about 70 nm and a periodicity of 100 nm were fabricated by this two step anodization process (Figure 18). Finally a thin layer of Au (~ 16 nm thick) for conductivity was deposited on the back-side of the template by sputtering.

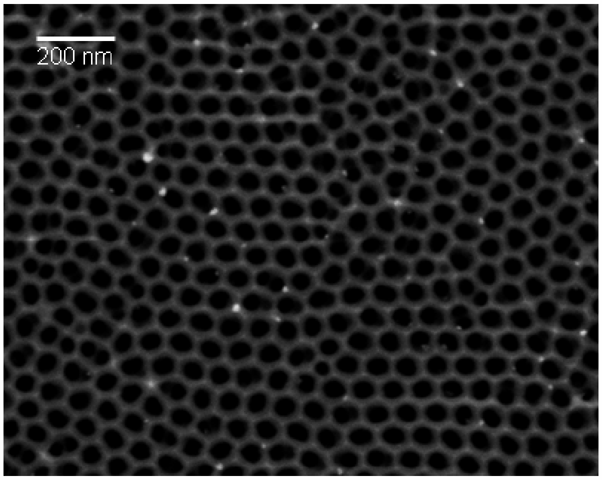

Figure 18: SEM image of an alumina template with an ordered hexagonal pore structure (top view).

Prior to the pore filling, Pt was electrodeposited on the back-side of the template in order to avoid the formation of a continuous film during the electrodeposition of the Co-Pt alloy.

2.3 Diblock copolymer template fabrication

In the following, the key steps to produce diblock copolymer templates will be described. Pieces of oxidized Si (100) covered with a 30 nm Cr adhesion layer and a 10 nm Au conducting layer are used as substrates. A low surface roughness is important for the formation of the ordered arrays of nanopores. In order not to disturb the ordering process for the samples the RMS roughness was found to be in the range of 0.5 nm over an area of 1 µm × 1µm (Figure 19). Diblock copolymer templates have been fabricated by the group of Prof. Stamm at IPF Dresden. Poly (styrene-*block*-(4-vinylpyridine)) (PS-PVP), with number average molecular masses (M_n) of PS 35500 g/mol, PVP 3680 g/mol, M_w/M_n = 1.06 for both blocks, purchased from Polymer Source, Inc. 2-(4′ Hydroxybenzeneazo) benzoic acid (HABA) was purchased from Sigma-Aldrich. Nanoporous templates were prepared by dip-coating the conducting substrate in a solution (dioxane) containing 1 wt. % of diblock copolymer polystyrene-*block*-poly (4-vinylpyridine) (PS-b-P4VP) and 2-(4-hydroxybenzeneazo) benzoic acid (HABA). A speed up to 1 mm/s and a dip time of 10 s are used as dip-coating parameters. The long-range order in the cylindrical morphology of the dip-coated thin films was relatively poor. It was improved by annealing the sample in vapor of 1,4-dioxane. During the solvent vapor annealing, a sufficient mobility is induced in the system which helps to approach the equilibrium state of highly ordered structures. The vapor annealing was performed in a glass dish in which 1,4-dioxane was stored in a small petri-dish. The sample was placed in the glass dish which then was tightly sealed. The sample was removed when the swelling ratio, i.e. the ratio between the thickness of the swollen film and the thickness of the original film, of ~ 2.75 (room temperature) was reached, as visually estimated from the color of the swollen films.

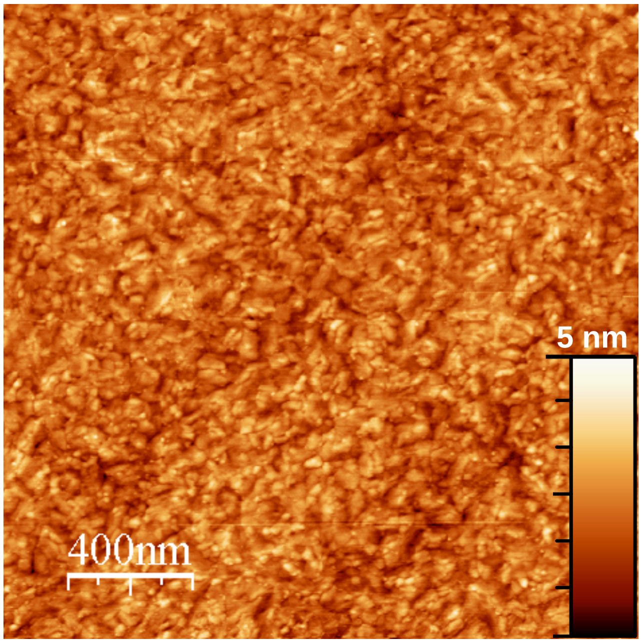

Figure 19: AFM image of the Si substrate with a 30 nm Cr adhesion layer and a 10 nm Au as conducting layer.

Earlier studies have shown that, at this swelling ratio, the maximum long-range order of perpendicular cylindrical domains is achieved. After vapor annealing the HABA was selectively removed with methanol to open the pores. Figure 20 shows a typical atomic force microscopy image of a PS-b-P4VP film after washing HABA in methanol for 10 min. HABA selectively binds to the pyridine group of P4VP by hydrogen bonds. Thin films of the PS-P4VP + HABA assembly exhibit a hexagonal cylindrical morphology composed of the P4VP (HABA) cylinders and the PS matrix.

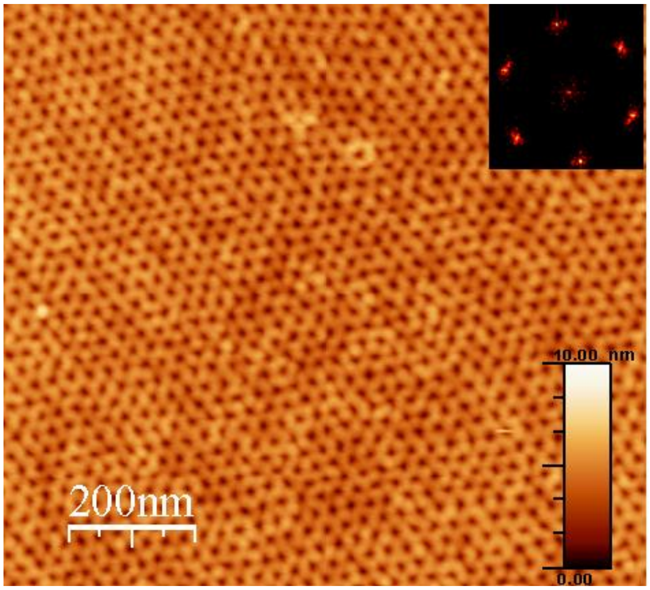

Figure 20: AFM image of a diblock copolymer template and corresponding Fourier transform image (inset).

Rinsing in a selective solvent, i.e. methanol, allows for the extraction of HABA from the film. This leads to the formation of cylindrical channels in PS matrix with P4VP chains collapsed on the wall of the channels. Some collapsed P4VP chains however may also remain at the bottom. The cylindrical channels are oriented normal to the surface of the film and span the entire film thickness. The cylindrical channels are nearly perfectly hexagonally arranged (see inset Figure 20). The diameter of a cylinder is about 8 nm, with a periodicity of about 24 nm[64]. The average template thickness measured by ellipsometry was ~ 30 nm.

2.4 Electrodeposition set-up for nanowires

The 3-electrodes arrangement of an electrochemical cell used for the deposition of Co and Co-Pt nanowires into anodic alumina oxide (AAO) and diblock copolymer membrane is schematically shown in Figure 21.

A ~ 16 nm thin layer of Au was deposited on the back-side of the alumina template by sputtering to obtain some conductivity. Prior to the electrodeposition, Pt was deposited on the back-side of the template in order to avoid the formation of a magnetic thin film during the electrodeposition of the Co-Pt alloy.

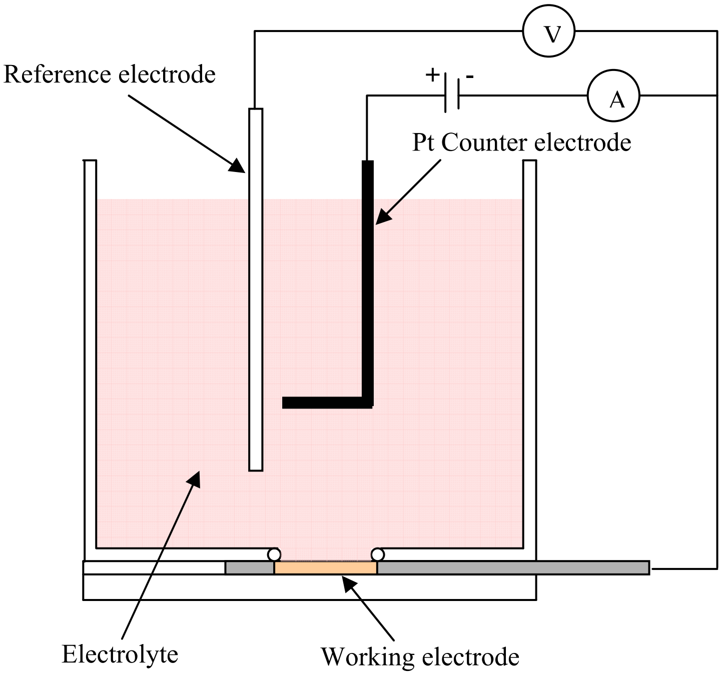

Figure 21: Schematic diagram of an electrochemical cell used for the deposition of Co and Co-Pt nanowires.

The electrodeposition was carried out at room temperature using a three electrode potentiostatic control with a saturated calomel electrode (SCE) as a reference electrode, a platinum plate as a counter electrode and a Au coated AAO template as working electrode. The electrolyte used for the deposition of Co-Pt nanowires consists of 0.1 M $CoSO_4.7H_2O$, 0.003 M H_2PtCl_6. The pH value of the solution was 2.5. The deposition was carried out for 80 min by varying the potential from -0.6 to - 0.9 V, controlled by an EG & G model 263 A potentiostate.

In order to deposit Co and Co-Pt, diblock copolymer templates on oxidized Si (100) covered with a 30 nm Cr adhesion layer and a 10 nm Au conducting layer has been used as a working electrode. The counter and reference electrodes are the same as those used for the deposition of Co-Pt nanowires into AAO templates.

The electrolyte used for the deposition of Co within the diblock copolymer consists of 0.5 M $CoSO_4.7H_2O$ and 0.1 M H_3BO_4, and the pH of the solution was adjusted to 7 using NH_4OH. The deposition was carried out using pulse plating by applying a 4 mA current as cathodic and anodic pulse for 10 ms and 2 ms, respectively. The total number of 250 sweeps has been used for the electrodeposition.

The electrolyte system and the pH used for the deposition of Co-Pt within the diblock copolymer template is the same as that used for the Co-Pt thin films (refer 2.1). The deposition was carried out for 2 minutes at a current of 2 mA (current density ~ 36 mA/cm^2).

2.5 Structural characterization

2.5.1 X-ray diffraction (XRD)

X-ray diffraction (XRD) is a nondestructive technique used to characterize the crystallographic structure, the crystallite size and the preferred orientation in a sample. In XRD, a set of atomic planes of the sample parallel to the substrate satisfying Bragg's condition ($n\lambda = 2d\sin\theta$, where λ is the wavelength of X-ray, d is the distance between the planes, n is an integer and θ is the incidence angle) confirms crystallinity in the sample. If the sample is crystalline, distinct peaks are observed in the X-ray diffraction pattern. Moreover, textured samples show preferential reflections only from a certain family of atomic planes which are parallel to the substrate surface, denoted as {hkl}. Knowledge of the *d*-spacing of these planes can be used for phase identification by comparison with the powder diffraction file (PDF) database. In Bragg-Brentano geometry, only lattice planes parallel to the sample surface contribute to the XRD patterns. Hence, for textured samples only few families of reflections are observed. For instance, a sample with a strong {00l} texture will only exhibit {00l} lines in the Bragg-Brentano geometry.

θ-2θ XRD patterns of Co-Pt films and nanowires have been measured in Bragg-Brentano geometry in a Philps X'pert (PW3020) Diffractometer with CoK$_\alpha$ (λ = 0.178 nm) radiation.

2.5.2 Pole figure analysis

Pole figure measurements are a useful technique to determine the orientation (texture) relationship of the film with respect to the substrate and buffer. Although mainly used for texture analysis, it is used in particular to identify the phases in the sample. To obtain information about the orientation distribution of a set of lattice planes, the diffraction condition $(\theta - 2\theta)$ is set to the corresponding lattice spacing, defined by Bragg's equation. While keeping this condition constant, the sample is rotated (ϕ) and tilted (ψ) and the intensity at these different orientations is recorded. Poles are usually represented in a similar way to the crystallographic planes with their Miller indices (hkl). A pole is the projection of the normal of a plane onto a 3-D sphere residing around the circle.

The presence of the distinct pole indicates that the sample not only has an out-of-plane texture but also has an in-plane texture with a unique relation with respect to the buffer/substrate known as epitaxial relation. A ring in the pole figure measurements corresponds to the preferred orientation of the crystallites along a certain crystallographic axis.

Co-Pt pole figures ($0 \leq \phi \leq 360°$ and $(0 \leq \psi \leq 82°)$ have been measured with a Philips X' pert (PW3040) texture goniometer with CuK$_\alpha$ (λ = 0.154 nm) radiation. Before starting the pole figure measurements for a certain reflection, the $(\theta - 2\theta)$ value was optimized on an expected pole for maximum intensity. Then the samples were measured at fixed 2θ values. For phase identification pole figure measurements have been carried out for the (200) pole of the fcc phase and are compared with pole figures of the most densely packed planes that can originate either from (002) hcp or (111) fcc planes. The (200) fcc has been chosen for the pole figure measurements as this is a unique reflection which does not coincide with any of the hcp reflections of Co-Pt.

2.6 Vibrating sample magnetometry (VSM)

A vibrating sample magnetometer (VSM) operates on Faraday's law of induction, which tells that a changing magnetic field will produce an electric field. In a VSM the sample is subjected to a sinusoidal motion and the voltage is induced in the pick-up coils according to Faraday's law of induction. The induced voltage in the pick-up coil is proportional to the sample's magnetic moment, which can be varied by changing the magnetic field produced by an electromagnet. In a VSM, the sample is placed inside a uniform magnetic field to magnetize the sample. The sample is placed on a long rod, which is positioned between the pole pieces of an electromagnet to which the pick-up coils have been mounted.

Field and temperature dependent magnetization measurements of Co-Pt films, Co-Pt nanowires and rolled-up Co nanotubes were performed in a PPMS VSM set-up with a maximum applied field of 3 T. Hysteresis curves have not been corrected for the demagnetization field contributions. A correction for the applied field due to the demagnetization can be done to obtain the internal field, $H_{in} = (H_{ext}-N_dM)$, where H_{ext} is the external magnetic field and N_dM is the demagnetizing field of the sample. For the field applied perpendicular to an homogeneous magnetic film the demagnetizing factor N_d is 1, and 0 for the applied field in the plane. In order to correct the demagnetizing field for a magnetic thin films, the thickness of the film must be known accurately and also the film has to be homogeneously magnetized. In literature there are sometimes some compromises for the N_d used for the correction of the demagnetizing field of thin films[81]. Since a selection of N_d different from 0 or 1 is arbitrary and the film thickness of the presented films could not be measured accurately enough, here, it was decided not to deshear the magnetization curves. The hysteresis curves have been measured with a sweep rate of 5 mT/s. The magnetic field was applied perpendicular (out-of-plane) and parallel (in-plane) to the substrate. Due to the sensitivity of the device, the diamagnetic signal of sample holder and substrate also contribute to the measured magnetic moment. The magnetic moment of the Co-Pt films, having a sample size of 2 mm x 2 mm to 4 mm x 4 mm, measured by VSM is $10^{-5} – 10^{-4}$ emu, whereas the background arising from the sample holder and the diamagnetic substrate is ~ 10^{-6} emu. Therefore, in order to deduce the magnetic moment solely arising from the film or nanowires, a careful measurement of the background signal is necessary. Hysteresis measurements of a Co-Pt film measured in a VSM are shown in Figure 22. Three different hysteresis loops correspond to the as-measured sample (contribution from Co-Pt film, Si substrate and the sample holder) and a corrected hysteresis curve, showing only the contribution of the film after subtraction of the background curve.

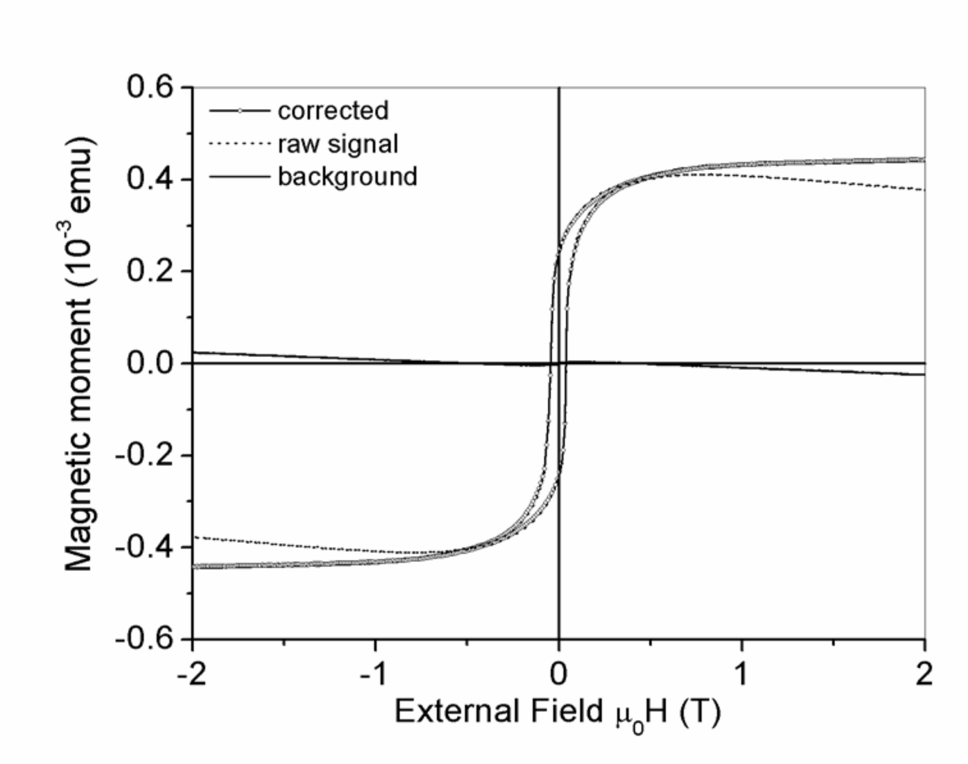

Figure 22: Hysteresis loops of Co-Pt films (raw and background corrected) with a background measured at room temperature.

2.7 Scanning electron microscopy (SEM)

- **Surface morphology**

The microstructural characterization of the Co-Pt films and the CoPt nanowires has been performed in a scanning electron microscope (SEM). SEM images the sample surface by scanning it with the very high energy electron beam. The elastic and inelastic scattering of the electrons in the solid specimen produces a wide variety of emissions, all of which are potentially useful. The sketch for the electron beam-specimen interaction is shown in Figure 23. Each of these signals is produced with different efficiency, coming from a different volume of the sample, and carries the different information about the specimen. These signals mainly consist of backscattered electrons, which consists of incident electrons scattered through large angle (90° or more) within the sample and secondary electrons. The fractional yield (η) of backscattered electrons, the i.e. number of the backscattered electrons/number of incident electrons is called the backscattered yield. The average energy of these electrons is about 0.5 to 0.6 of the incidents energy and the η is typically 0.2 to 0.4. The energy of the secondary electrons lies within the range of 0 to 50 eV. As the energy of the backscattered electrons is much greater than that of secondary electrons, the backscattered electrons can consequently emerge from the considerable depth within the specimen. For a beam energy of 20 keV backscattered electrons can carry information about regions several micrometers below the sample surface compared with a few nanometers for the secondary electrons. The yield η of backscattered electrons varies with the atomic number of the target. Although this yield η also somewhat depends on the energy of the incident electrons, above 5 keV the backscattered yield is almost independent of the accelerating voltage. In this case η can be approximated by the function:

$$\eta = -0.0254 + 0.016Z - 0.000186Z^2 \qquad (2.1)$$

Where Z is the atomic number of the target.

Since the yield is a monotonic function of Z a backscattered image can display a contrast which is directly related to the atomic number of the atoms in the area sampled by the electron probe. Thus, in multiphase alloys regions of the specimen with different atomic number will appear with different brightness. The level of the contrast depends on the difference in Z.

The secondary electrons are produced by a variety of inelastic scattering processes within the sample. Because the secondary electrons are low in energy they can not travel more than a few nanometers through the sample to reach the surface. The dominant imaging mode for the secondary electrons is topographic contrast[82]. The effect arises when an increase in the angle of incidence θ (the angle between the beam and the surface normal) will lead to an increase in the yield of secondary electrons. As θ increases the fraction of the secondary electrons produced also increases. The secondary signal $I(\theta)$ at an angle of incidence θ is related to the signal $I(0)$ at normal incidence by the approximate relationship:

$$I(\theta) = I(0)\sec\theta \qquad (2.2)$$

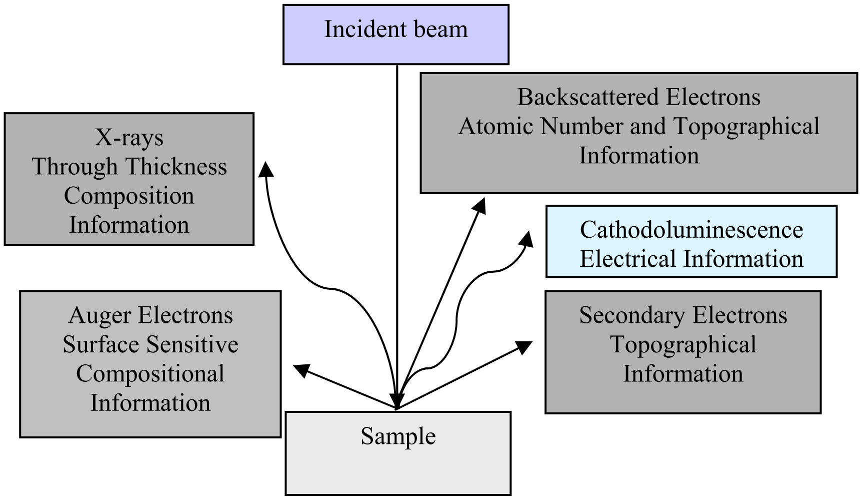

Figure 23: Information from electron beam-specimen interactions.

If an electron beam moves over a surface which has topography, the local angle of incidence between the beam and the surface normal will change and produce a corresponding change in the secondary signal. When the sample has a rough surface or a significant surface topography then this results in an image containing pronounced light and shadow effects. Faces at a high angle of inclination to the beam and facing the detector will be bright, while surfaces normal to the beam will be darker. The Co-Pt films and nanowires were analyzed using a Leo Gemini 1530 SEM equipped with in-Lens and secondary electron (SE) detectors using a beam energy of 5 keV.

- **Energy dispersive X-ray analysis**

The SEM is usually equipped with an energy dispersive X-ray (EDX) spectrometer to determine the composition of the sample. In this technique an electron beam strikes the surface of the conducting sample. The energy of the beam is typically in the range of 10-20 keV. The interaction of the high energy electron beam with the sample results in the emission of abroad wavelength band of radiation called continuous or white radiation and characteristic radiation. The white radiation is produced as the impinging high energy electrons are decelerated by an interface with the atomic electrons of the elements making up the specimen. While the characteristic X-rays emitted from the sample depend on the material under examination. These characteristics X-rays are emitted when the energy of the striking electron is greater than the binding energy of the atomic electron. As a result the atomic electron will be ejected from its atomic position, departing from the atom with a kinetic energy $(E-\phi)$ equivalent to the difference between the energy E of the initial particle and the binding energy ϕ of the atomic electron. As long as the vacancy in the shell exists, the atom is in an unstable state. The excited atom can regain stability by the transfer of an electron from one of the outer orbitals to fill the vacancy. The energy difference between the initial and the final state of the transferred electron may be released in the form of an X-ray photon. Since all emitted X-ray photons have energies proportional to the difference in the energy states of the atomic electrons, the lines from a given element will be characteristic of that element. EDX spectra of Co-Pt films and nanowires were recorded using the Leo Gemini 1530 SEM equipped with a XFlash detector using a beam energy of 20 keV.

2.8 Atomic force microscopy (AFM) / Magnetic force microscopy (MFM)

Atomic force microscopy (AFM) was also used to probe the surface morphology of the Co-Pt films and the diblock copolymer templates. The principle behind the operation of an AFM is shown in Figure 24. The tip is attached to the free end of a cantilever and is brought very close to the surface of the sample. Attractive or repulsive forces resulting from interactions between the tip and the surface will cause a positive or negative bending of the cantilever. The bending is detected by means of a laser beam, which is reflected from the back side of the cantilever. The AFM was used in the tapping mode, where the cantilever is oscillating close to its resonance frequency. An electronic feedback loop ensures that the oscillation amplitude remains constant, such that a constant tip-sample interaction is maintained during scanning. Forces that act between the sample and the tip (van der Waals forces) will not only cause a change in the oscillation amplitude, but also a change in the resonant frequency and in the phase of the cantilever. The amplitude is used for the feedback and the vertical adjustment of the piezoscanner is recorded as a height. The AFM provides a number of advantages over conventional microscopy techniques. It probes the sample and makes measurements in three dimensions, x, y, and z (normal to the sample surface), thus enabling the presentation of three-dimensional images of a sample surface. This provides a great advantage compared to other available microscopes. With good samples (clean, with no excessively large surface features), the resolution in the x-y plane ranges from 0.1 to 1.0 nm and in the z direction it is about 0.01 nm (atomic resolution).

Whereas in the SEM a beam of electrons must travel to the sample to provide an image, the sample must be vacuum compatible and either electrically conductive or coated with a conductive layer to avoid charge buildup[83], the AFM requires neither a vacuum environment nor any special sample preparation and it can be used in either an ambient or liquid environment.

The magnetic microstructure of the Co-Pt films was studied by MFM. In MFM a magnetic tip is used to probe the magnetic stray field above the sample surface. The image is formed by scanning the tip laterally with respect to the sample and measuring the force gradient as a function of position[84]. The force gradient is detected by the resonance frequency shift of the cantilever[85].

The magnetic force acting on the tip is given by:

$$\vec{F}_m = m_z \left(\frac{\partial B_z}{\partial z} \right) \hat{e}_z \qquad (2.3)$$

Where m_z is the magnetic moment of the tip, B_z is the magnetic field of the sample along the z direction and $\hat{e}_z$ is the unit vector along the z direction.

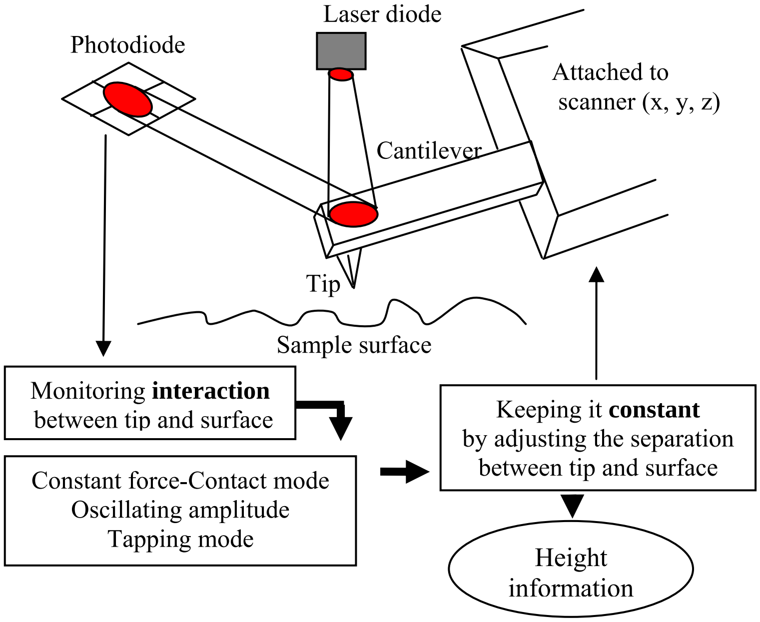

Figure 24: Schematic diagram showing the operating principle of AFM.

MFM detects the force gradient of the total force, along the *z* direction which can be written as:

$$\frac{\partial F_m}{\partial z} = m_z \frac{\partial^2 B_z}{\partial z^2} \qquad (2.4)$$

MFM images of Co-Pt films, presented in this work, have been taken in the remanent state of the samples.

Chapter 3

Continuous Co-Pt films

Co-Pt films have been deposited on Si (100) substrates with a 30 nm thick Cr buffer and a10 nm Au conducting layer, as discussed in section 2.1. The films have been deposited at different current densities. The influence of the phase formation has been correlated with magnetic properties of the films. Latter section deals with the ageing effect of electrolyte on composition, phase formation and magnetic properties of the films.

3.1 Current-potential curves

Potentiodynamic current-potential curves were measured in order to characterize the deposition of pure Co, pure Pt and the co-deposition of Co-Pt (Figure 25).

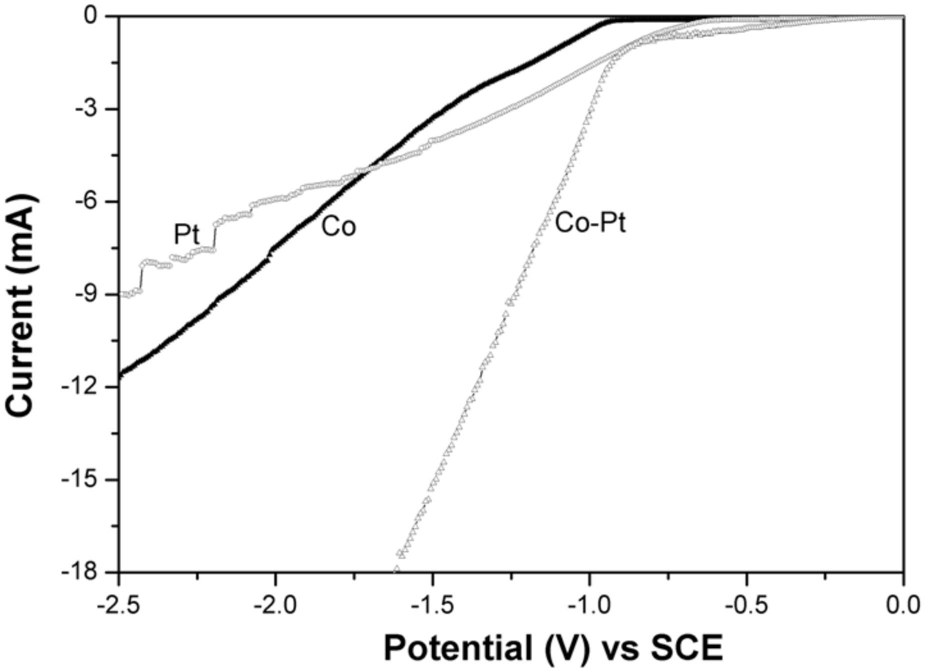

Figure 25: Current-potential curves of pure Co, pure Pt and Co-Pt deposition. The electrolyte systems and pH used for the deposition have been discussed in section 2.1 (Scan rate 10 mV/s).

The Pt curve exhibits a current onset at a more positive potential (-0.6 V) than Co (-0.9 V). In case of Co-Pt system current onset is observed at slightly low negative potential (-0.85 V) compared to the pure Co deposition. This onset in current can be attributed to the co-deposition of the Co-Pt alloy. From the current-potential curve for Co-Pt deposition, a starting current of 10 mA (~ 10 mA/cm^2) was chosen for the deposition of Co-Pt films.

3.2 Film morphology and chemical composition

Co-Pt films have been prepared by varying the current density from 10 to 32 mA/cm^2, as discussed in section 2.1.1. The chemical composition was determined by EDX. Morphological investigations of the films deposited at two different current densities are shown in Figure 26. The film morphology changes with the current density.

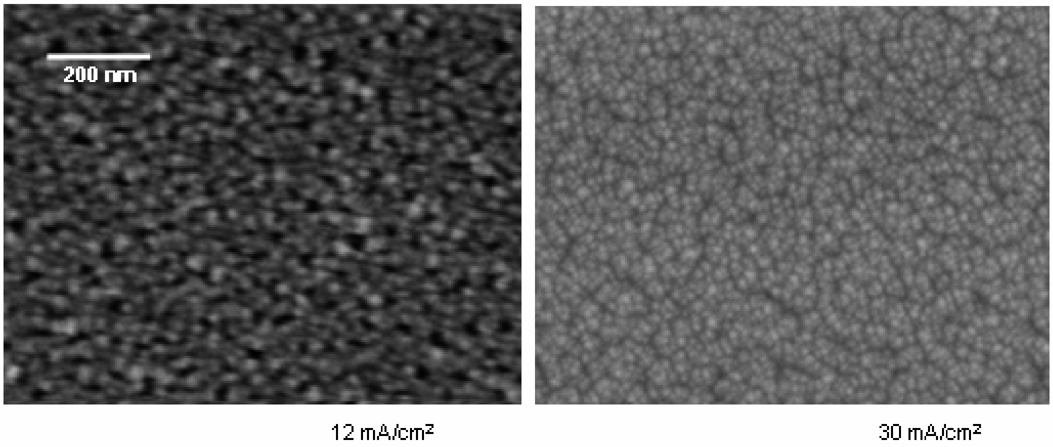

12 mA/cm^2 30 mA/cm^2

Figure 26: Surface morphology of the films deposited at two different current densities.

The composition of the electrodeposited alloys was $Co_{100-x}Pt_x$, where x changes from 45 to 26 at. % with current density (Figure 27). The concentration of Co in the films increases with the current density up to 18 mA/cm^2. At higher current density (above 18 mA/cm^2) Co to Pt ratio in the films is almost constant. This is attributed to the diffusion limited deposition of Co and Pt at higher current densities.

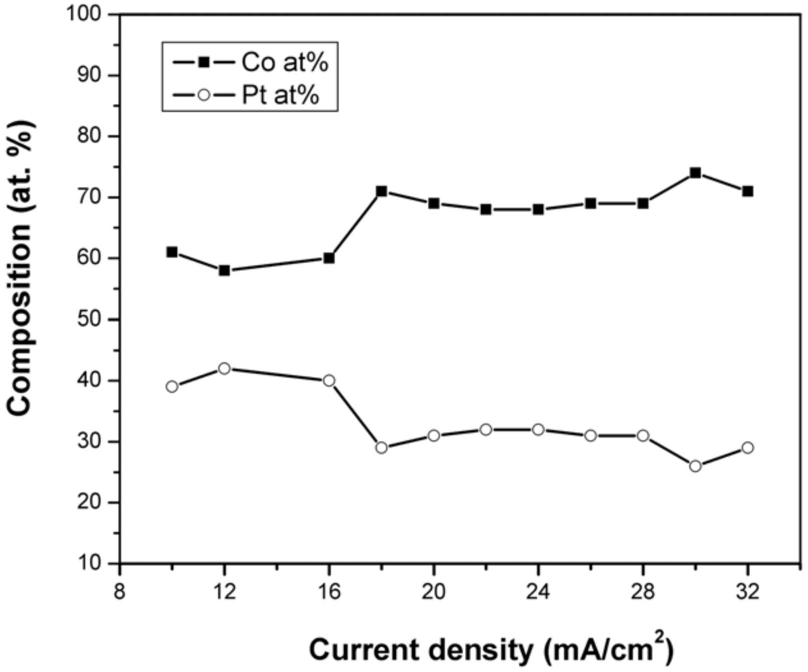

Figure 27: Film composition versus current density.

3.3 Phase formation and crystal structure

3.3.1 XRD patterns of Co-Pt films

XRD patterns of Co-Pt films deposited at different current densities are shown in Figure 28. The perpendicular lines in the X-ray diffraction patterns correspond to the hcp and fcc reflections calculated using the lattice parameter for the hcp and fcc $Co_{80}Pt_{20}$ phases. In addition to the (400) reflection originating from the Si substrate at 82.43° and the (111) reflection of the Au buffer at 44.65°, two reflections at ~ 49.89° and at ~ 116.12° originating from the Co-Pt films are observed. For a better visibility of the XRD patterns, the Si reflections have been removed from the graph. These reflections don’t match exactly with the perpendicular lines drawn in Figure 28, as these lines correspond to the 2θ value of $Co_{80}Pt_{20}$. In our case the maximum Co content

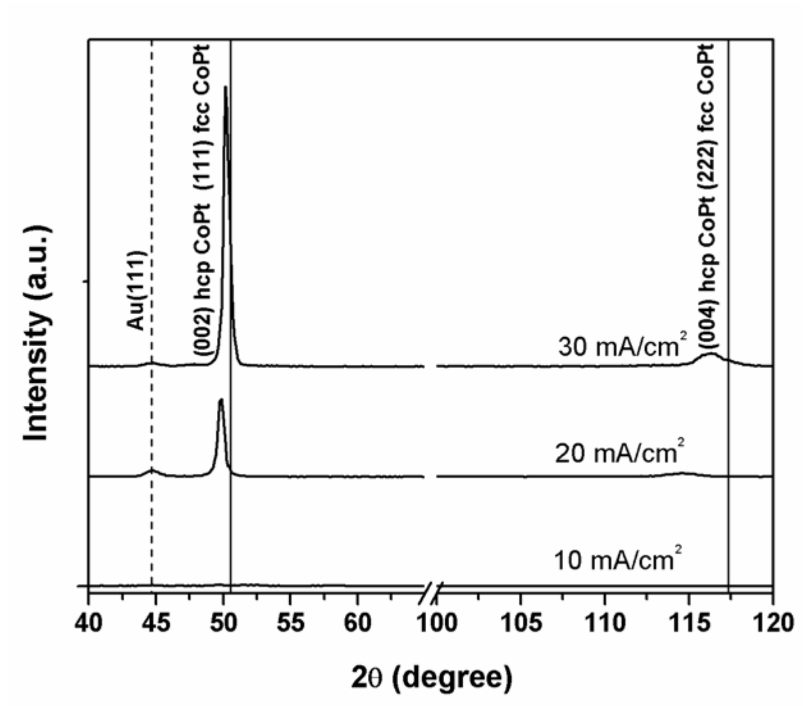

Figure 28: XRD patterns of Co-Pt films deposited at different current densities measured in Bragg-Brentano geometry.

in the films is 74 at. %. Hence, the lattice parameters are expected to slightly differ from $Co_{80}Pt_{20}$. Due to the similar lattice spacing for hcp and fcc the measured reflection position of Co-Pt almost coincides with the position expected for both possible structures, (002) hcp and (111) fcc Co-Pt. The higher order reflections originating from planes parallel to the first ones ((004) hcp and (222) fcc Co-Pt)) also coincide and therefore, do not give any help for phase identification. As no other reflections occur in Bragg-Brentano geometry a pronounced fibre texture can be assured. Similar findings have been reported for Co-Pt films on Cu (111) seedlayer[6].

3.3.2 Phase analysis by pole figure measurements

Consequently, for structure determination other lattice planes have to be measured that are not parallel to the substrate plane. When comparing positions of the most intense reflections calculated for an isotropic texture of both phases, only the (200) fcc reflection is unique and is sufficiently separated from the hcp reflection positions. Hence, pole figures have been measured for the (200) pole of the fcc phase and are compared with the (002) hcp/(111) fcc pole figures. The (002) hcp/(111) fcc and the (200) fcc pole figures are displayed for two films deposited at different current densities in Figure 29.

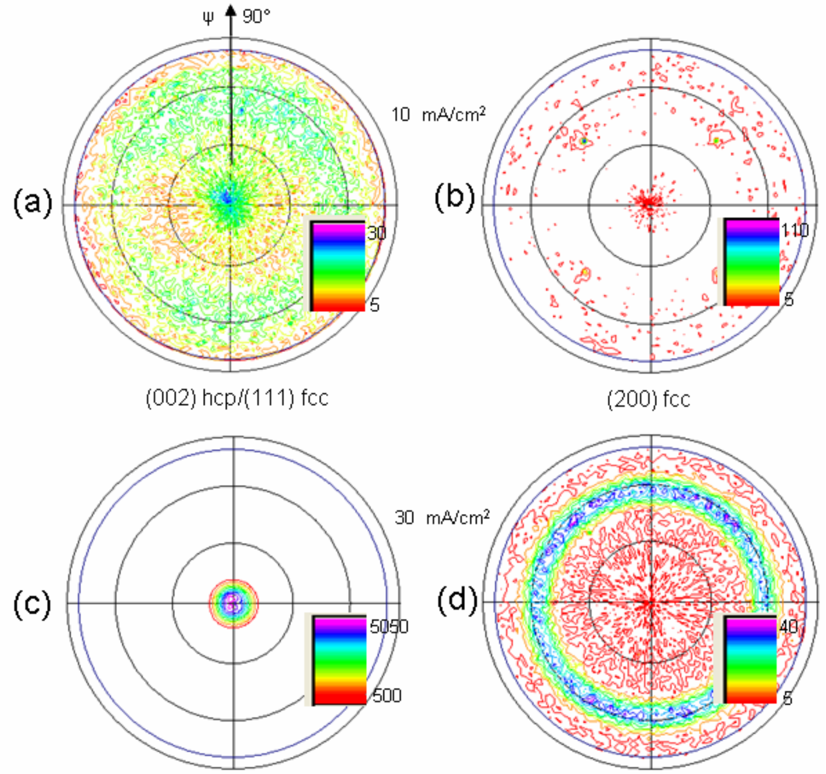

Figure 29: Pole figures of Co-Pt films deposited at current densities of 10 mA/cm^2 ((a) and (b)) and 30 mA/cm^2 ((c) and (d)), respectively. Whereas (a) and (c) show (002) hcp Co-Pt poles or (111) fcc poles; (b) and (d) show (200) fcc Co-Pt poles. For better visibility the intensity of each pole figure is linearly scaled to its maximum. For better comparison the maximum intensity is also given. Circles are shown at $\Psi = 30°$ and 60°.

For a film deposited at low current density (10 mA/cm^2, Figure 29 (a)) a broad ring between $\Psi = 55°$ and 70° is observed in addition to the central peak within the (002) hcp/(111) fcc pole figure.

If it is assumed that this pole figure originates from the hcp only, the central reflection would originate from the hcp unit cell with the c-axis aligned perpendicular to the substrate. The ring could originate from another texture component, having the c-axis inclined by about 60° to the substrate normal. This orientation however has neither densely packed planes parallel to the substrate nor represents a highly symmetric plane.

Though these arguments make an assignment to an hcp phase unlikely, the measurement of this pole figure does not allow to rule out the existence of hcp. The measurement of the (200) fcc pole figure indeed unambigously reveals the presence of the fcc phase. The highest intensity is observed in the centre, indicating a (111) texture (Figure 29 (a)). Since for a fcc structure the angle between (200) and (111) planes is 55°, one would expect a ring within the (111) fcc pole figure in agreement with the experiments. The angle between two neighboring (100) planes is 90°, hence they are not visible in the (200) fcc pole figures. In a similar way the central (111) fcc reflection can be consistently explained. The angle between two (111) fcc reflections is 70°, which explains why a broad ring is observed in the (111) pole figure (Figure 29 (a)). From these arguments also a ring at 54° is expected in the (200) pole figures. The diffraction intensity of (200) planes is significantly lower compared to the (111) planes, which apparently does not allow to clearly see this ring in the present measurements (Figure 29 (b)). In addition to the broad ring at around 54° within the (200) pole figure a four fold symmetry can be seen, which originates from the Si substrate. Hence, a fcc structure with a major (111) and a minor (200) texture component perpendicular to the substrate can consistently explain both pole figures. The ratio of the integrated intensities (integrating the intensity measured for (200) fcc and (002) hcp/(111) fcc poles) of both pole figures can be used to obtain criteria on the phase fraction. The integrated intensity of the the (200) fcc pole figure is about 35 % of the integrated intensity of the (002) hcp/(111) fcc pole figure. This value has to be compared with the relative diffraction intensities of (200) fcc planes to the (111) fcc planes. In the case of a pure fcc phase with isotropic texture the scattering intensities of (200) fcc is 53 % of (111) fcc planes. Hence this film contains mostly fcc phase with some minor fraction of hcp phase.

The (002) hcp/(111) fcc pole figure (Figure 29 (c)), is dominated by an intense single peak in the center according to hcp (002) or fcc (111) planes. The absence of additional reflections of other (111) planes expected at Ψ = 70.5° indicates that the central reflection is mostly due to the hcp phase having its c-axis aligned perpendicular to the substrate. Since the angle between different (002) hcp poles is 180°, no other reflection is visible in this pole figure. However, within the (200) fcc pole figure (Figure 29 (d)) a ring at Ψ = 55° is observed, which corresponds to the angle between the (111) and (200) planes in fcc structure. This indicates that still a minor contribution of fcc phase with a (111) orientation must exist. For the films deposited at a higher current density (30 mA/cm^2) the hcp (002)/fcc (111) pole figure (Figure 29 (c)) shows a much higher intensity compared to the (200) fcc pole figure (Figure 29 (d)), which suggests a low fraction of the fcc phase. The integrated intensity ratio of the (200) fcc is 1.5 % of the integrated intensity ratio of the (002) hcp/(111) fcc pole for this film. When neglecting this minor fcc content, the (002) hcp/(111) fcc pole figure can be assigned to the hcp structure only. The observed central peak hence reveals a strong (002) hcp fibre texture. The integrated intensity ratio was evaluated for all films and will later be used to establish a correlation between the structure and the magnetic properties.

3.4 Magnetic properties and their correlation with structure

Hysteresis loops of characteristic Co-Pt films measured at room temperature are shown in Figure 30. They have not been corrected for the demagnetization field contribution. At low a current density (10 mA/cm^2; Figure 30 (a)) the magnetization saturates in low applied fields when the field is applied in-plane. A significantly higher field is required to saturate the magnetization with the field applied perpendicular to the substrate. In this direction a field of about 0.9 T is required. Since this is close to the saturation magnetization of Co-rich Co-Pt (M_S = 0.97 T), the magnetic properties are mostly dominated by the shape anisotropy of the present thin film geometry and not by magnetocrystalline anisotropy. This agrees with the pole figure measurements revealing a mostly fcc structure, which is characterized by a low cubic magnetocrystalline anisotropy.

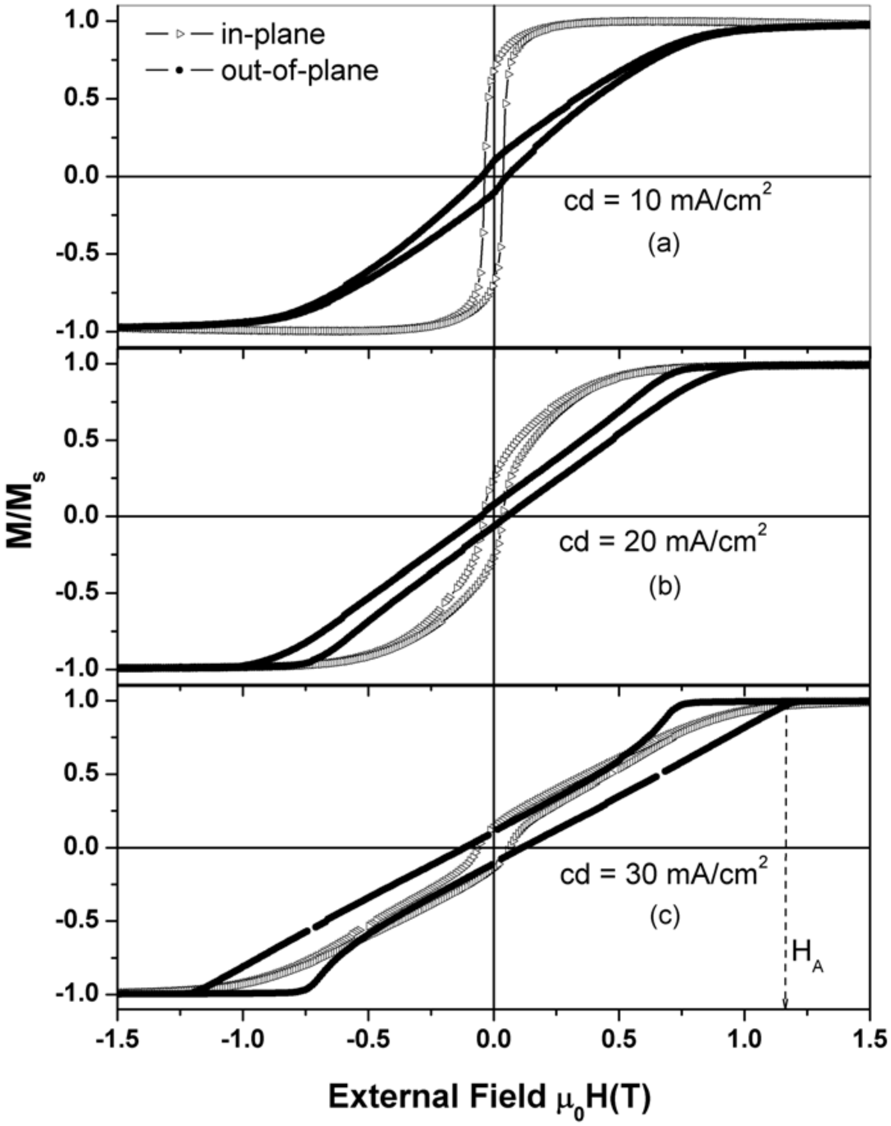

Figure 30: Hysteresis loops of Co-Pt films measured with the field applied in-plane (open triangles) and out-of-plane (solid circles) of three films deposited at current densities of 10 mA/cm² (a), 20 mA/cm² (b) and 30 mA/cm² (c).

Hysteresis curves for a samples deposited at an intermediate current density of 20 mA/cm^2 are shown in Figure 30 (b). The in-plane hysteresis curve is not linear any more, but exhibits a significant curvature. This behavior may either originate from the contribution of the anisotropy constant of higher order (K_2) or, more likely, from an exchange coupled two phase system with different anisotropy constants (hcp and fcc). Considering only the first order anisotropy constant (K_1), would result in a linear dependence of the magnetization with field, while including higher order constant (K_2), The magnetization becomes nonlinear with applied field. In the case of an exchange coupled two phase system, the magnetization of the soft phase (fcc Co-Pt) is rotated into the field direction already at low fields. This is superimposed by the rotation of the hard phase (hcp Co-Pt). A similar shape of hard axis loop had been recently analyzed by Neu *et al.*[86]

The hysteresis curves are significantly different when examining films deposited at a high current density (30 mA/cm²; Figure 30 (c)). Now a high field is required to saturate the sample in-plane. This agrees with the results of the texture measurements, revealing the formation of the anisotropic hcp phase with the easy axis aligned perpendicular to the substrate. However, the estimated anisotropy field, as sketched in Figure 30 (c), is about 1.13 T, which is low compared to the value calculated for the Co-rich Co-Pt film ($\mu_0 H_A \sim 2.4$ T)[49]. The reason for this low anisotropy could be an increased number of stacking faults in the hcp phase when approaching the stability limit of the hcp phase. At low field, indeed, a steep increase of the magnetization is observed in the in-plane direction, indicating that a low amount of fcc phase with low magnetocrystalline anisotropy is still present in the sample. This coexistence of two phases is expected by the equilibrium phase diagram[23].

As expected from the increased magnetocrystalline anisotropy, the coercivity in the out-of-plane direction increases to $\mu_0 H_c \sim 0.12$ T for a film deposited at 30 mA/cm^2. However, coercivity is not sufficient to overcome shape anisotropy and reach a remanence to saturation ratio close to one. This can be attributed to the fact, that during electrodeposition no additives like phosphorus had been used, which allow to decouple grains for an enhanced coercivity.

In Figure 31 the coercivity (out-of-plane direction) and the remanence ratio are plotted with respect to the integrated intensity ratio of (002) hcp/(111) fcc to (200) fcc, calculated from the pole figure measurements. At a low integrated intensity ratio the coercivity is also low (0.05 T), which is due to the existence of mainly fcc phase in the films. The fcc phase still has a small (cubic) anisotropy, hence, the coercivity does not drop to zero for an almost pure fcc film. With the increase in the integrated intensity ratio an increase in coercivity (~ 0.12 T) is observed, which is due to a higher amount of anisotropic hcp phase in the film, exhibiting a pronounced alignment of the easy c-axis perpendicular to the substrate.

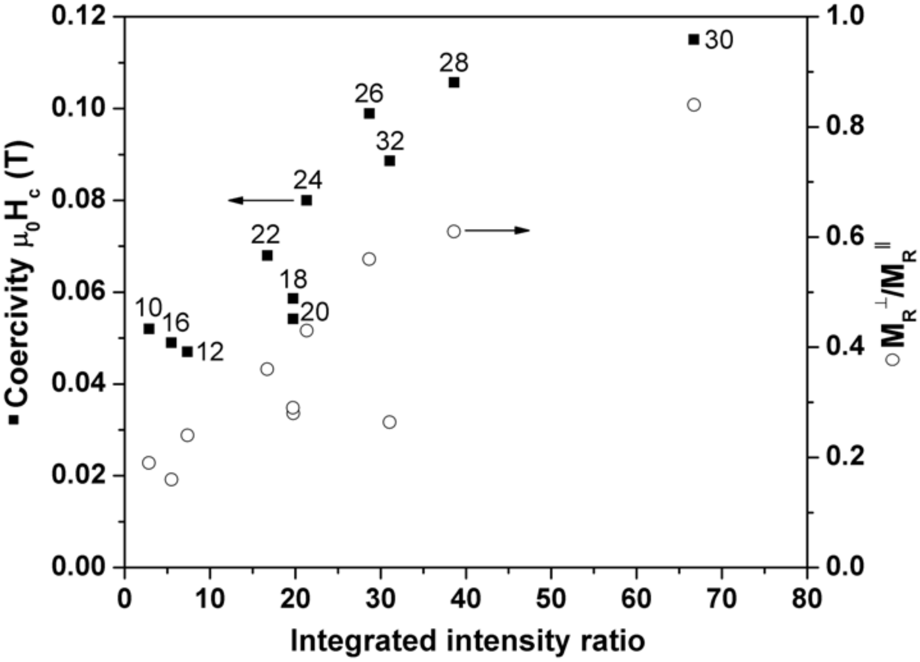

Figure 31: Out-of-plane coercivity and remanence ratio, calculated from the magnetic measurements, in comparison with the integrated intensity ratio calculated from the pole figure measurements. The numbers inside the graph beside the data points correspond to the deposition current density (in mA/cm^2).

In addition, the ratio of the out-of-plane to the in-plane remanence is shown in Figure 31, as a measure of magnetic texture. This ratio follows the same trend as the coercivity. Since the decrease at the highest current density (32 mA/cm^2) occurs simultaneously in both independent probes (i.e. pole figures and magnetic measurements), the suggested approach of a structural analysis indeed probes the key origin of the intrinsic magnetic properties. In Figure 31, the current density used for film preparation is additionally given. As a general trend, the films deposited at a higher current density exhibit a high integrated intensity, a high coercivity H_c and and a high $M_R^{\perp}/M_R^{//}$ ratio.

However, when plotting their correlation (not shown), a significant scattering is observed. This indicates that further parameters are important for structure control, as it will be discussed in section 3.6.

3.5 Magnetic microstructure

The AFM images, the magnetic domain structures and the corresponding magnetization curves of two samples deposited at 20 mA/cm^2 and 30 mA/cm^2 are shown in Figure 32. AFM images (Figure 32 (a, d)) show that both films exhibit a smooth surface morphology, as the roughness value is ~ 2 nm. MFM images (Figure 32 (b, e)) have been taken in the remanent state of the films. Due to the limit of the perpendicular field achievable (max. 0.5 T) with the MFM we are using, it was not possible to measure starting from the saturation field. An obvious color contrast in the MFM images shows distinct features of magnetic stripe domains, which indicates the presence of perpendicular magnetic anisotropy. This agrees with the structural and magnetic measurements. A shoulder in the hysteresis curve, when coming from the saturation state, is observed for the film deposited at 30 mA/cm^2. This characteristic shoulder (Figure 32 (f)) in the out-of-plane direction is connected with a nucleation of reversed domains.

Similar hysteresis curves, in the literature which also confirm the strong out-of-plane anisotropy of the thin films have been reported by other groups [87,88,89,90]. In thin films with perpendicular anisotropy, the saturation state is characterized by the single domain state.

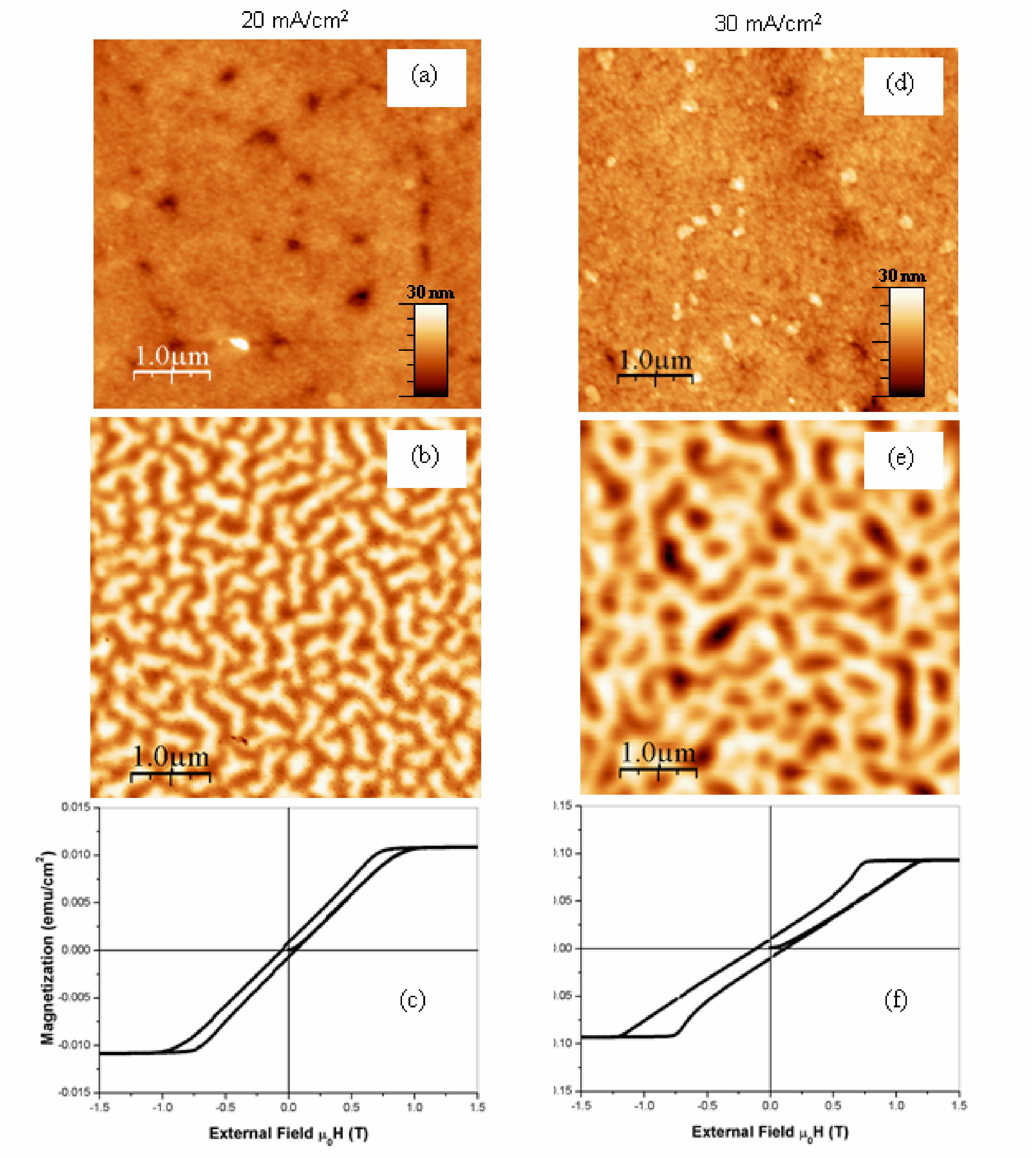

Figure 32: AFM images (a, d), MFM images in remanence state (b, e) and hysteresis curves (c, f) (measured in the out-of-plane direction) of two films deposited at 20 mA/cm^2 and 30 mA/cm^2.

As the field is decreased from saturation, a nucleation of the reversed domains takes place in the form of bubble domains. A further decrease of the field results in the formation of stripe domains. Their width and their magnetic contrast increase with the perpendicular anisotropy (see Figure 32 (e)). This could be due to the higher magnetostatic charge density at the surface of the sample. Similar findings have been reported by the group of Asenjo *et al.*[89] for FePd thin films with an out-of-plane anisotropy.

3.6 Ageing study of the electrolyte

There is significant scattering in the data points, when plotting the integrated intensity ratio and the coercivity for the samples deposited at the same current density. To understand this scattering in data points, the ageing effect of the electrolyte has been studied. For this, Co-Pt films have been deposited on different days after preparing the electrolyte keeping all other deposition parameters constant. A deposition current density of 28 mA/cm^2 was chosen for the deposition of the films, as the films deposited at this current density exhibited the best magnetic properties. The intensity measured in

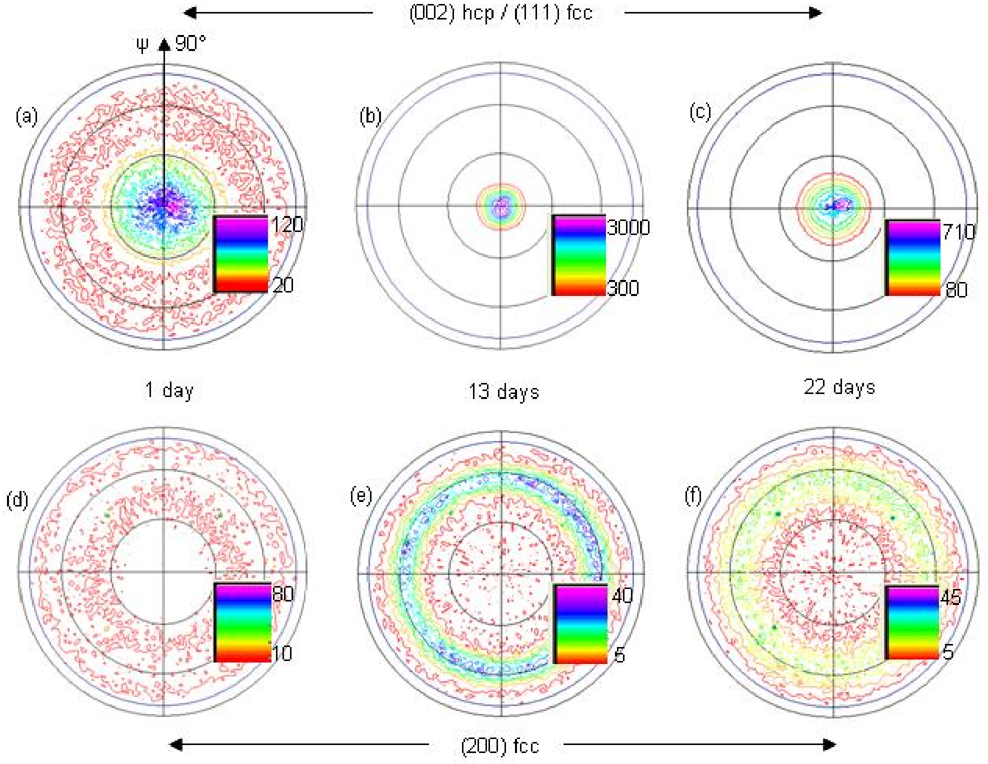

Figure 33: Pole figures of Co-Pt films deposited at 28 mA/cm^2 on different days after preparing the electrolyte; where (a), (b) and (c) are (002) hcp/(111) fcc and (d), (e) and (f) are (200) fcc poles. For better comparison the maximum intensity is also given. Circles are shown at Ψ =30° and 60°.

pole figures for the films deposited after 1, 13 and 22 days since deposition are shown in Figure 33. For the sample prepared on the same day of the electrolyte preparation the maximum intensity measured at the centre for the (002) hcp/(111) fcc is about 120 counts (Figure 33 (a)). Intensity increases to ~ 3000 counts (Figure 33 (b)) after 13 days and again decreases to 650 counts (Figure 33 (c)) after 22 days of preparing the electrolyte. In comparison to the (002) hcp/(111) fcc pole the intensity measured for the (200) pole of fcc is significantly lower. Its maximum intensity is about 80 counts (Figure 33 (d)) for the film prepared after 1 day, and decreased to 45 counts for the film prepared 22 days after preparing the electrolyte. Thus the low intensity measured for the (200) fcc pole, signifies that there is a minor contribution from the fcc phase to the intensity measured at the centre of the (002) hcp/(111) fcc pole. Therefore, the intensity measured at the centre within the (002) hcp/(111) fcc pole is mostly due to the hcp phase in the film.

Hysteresis curves of these samples are shown in Figure 34. The film deposited 1 day after preparing the electrolyte exhibits an in-plane anisotropy (Figure 34 (a)). A coercivity of 0.05 T is measured in both in-plane and out-of-plane directions. After an ageing of the electrolyte for 13 days, the easy axis changes from in-plane to easy out-of-plane (Figure 34 (b)). The in-plane hysteresis curve for the film deposited after 13 days is not linear, but exhibits a significant curvature. This behavior may either originate from the contribution of a higher order anisotropy constant (K_2) or more likely, from an exchange coupled two phase system with different anisotropy constants (hcp and fcc) as discussed in section 3.4. The coercivity increases from 0.05 to 0.11 T in the out-of-plane direction which can be attributed to a change in the anisotropy of the film. With further ageing of the electrolyte up to 22 days, the out-of-plane coercivity decreases (0.08 T) while the in-plane coercivity increases (0.09 T; see Figure 34 (c)). The dependence of the film composition, the integrated intensity ratio calculated from the pole figure measurements and the coercivity with the age of the electrolyte is summarized in Figure 35. It can be observed that the average cobalt composition in the films changes with ageing of the electrolyte. The average cobalt concentration is ~ 60 at. % for the film prepared after 1 day (Figure 35 (a)). After 22 days of ageing, the cobalt concentration is increased to 76 at. %. The integrated intensity ratio and the coercivity increase with the age of the electrolyte, and a maximum of both is obtained after 13 days which can be attributed to the formation of an hcp rich film as discussed in section 3.4. After 13 days of ageing there is a decrease in the integrated intensity ratio and in coercivity which is attributed to the decrease of the amount of hcp phase in the films. For the films prepared after 15 and 22 days, an increase in the fcc content is not correlated to composition. This indicates that the composition is not the only factor to change the integrated intensity ratio and the

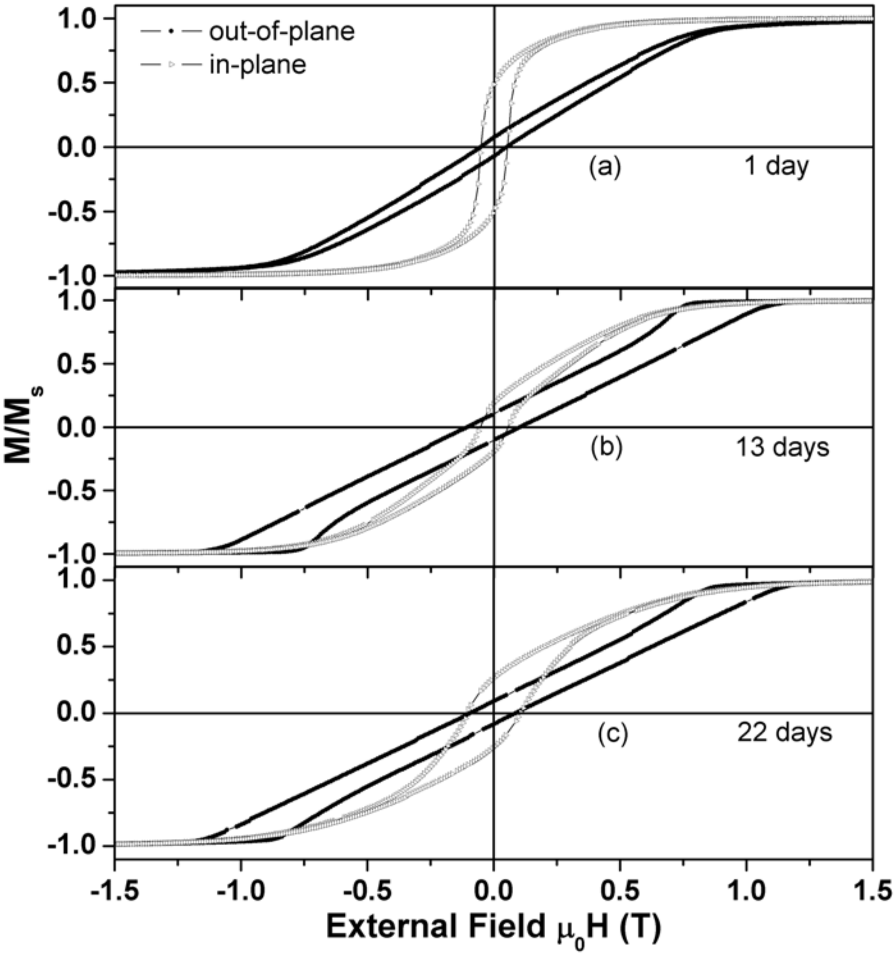

Figure 34: Exemplary hysteresis curves of Co-Pt films deposited at a current density of 28 mA/cm^2 from an aged electrolyte.

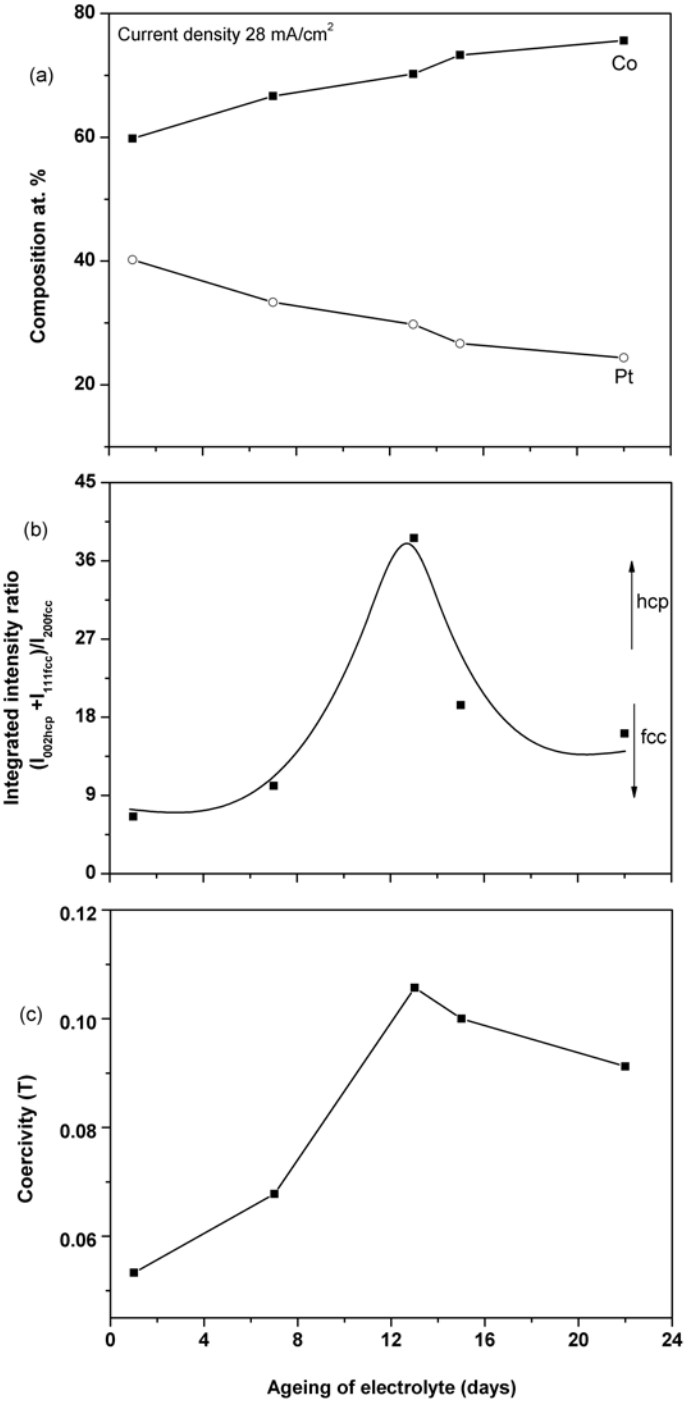

Figure 35: Variation of composition, integrated intensity ratio and coercivity (out-of-plane) with ageing time of the electrolyte.

coercivity. It is obvious from pole figures and magnetic measurements that the age of the electrolyte has a significant effect on phase formation and magnetic properties of Co-Pt films.

This instability in the deposition process of Co-Pt films has been explained by Donten and Osteryoung[91]. They have reported that the anodic oxidation of ammonia and citrate are both highly accelerated in the presence of Co^{2+} ions, which has a significant influence on the deposition of cobalt based alloys. The oxidation products can modify Co^{2+} reduction in two ways. First, it is possible that the extent and the nature of the complexation of Co^{2+} is changed because of a decomposition of ammonium citrate and formation of new compounds. Secondly, the new molecules formed in the anodic reaction may decrease the rate of reduction of Co^{2+} by adsorbing on the cathode surface. These adsorbed products on the cathode surface can influence the structure and magnetic properties of the films.

Chapter 4

Co-Pt nanowires within alumina templates

Alumina templates have emerged as an important self-assembly for nanofabrication. These templates have a high porosity (~ 10^{11} pores/cm^2). They can easily be prepared in the laboratory with a good control over the size (length and diameter) of the pores. Porous alumina templates can also withstand high temperatures, which may be necessary in some cases to anneal the deposited material. They can be used in different ways to synthesize self-assembled arrays of nanowires and nanodots of a variety of materials, such as metals, alloys, binary compounds and multilayers.

Magnetic nanowires have attracted much attention due to their novel physical and chemical properties. These nanowires have been investigated not only for the fundamental interest but also for their potential application in ultrahigh density magnetic storage devices and spintronics.

4.1 Influence of the deposition potential on morphology and composition

Co-Pt nanowires have been deposited into alumina templates using the three electrode deposition set-up as discussed in section 2.4. The electrolyte used for the deposition of the nanowires is different from that used for the continuous films, due to a possible dissolution of alumina template during the deposition process. The dissolution of alumina template can be attributed to the increase in the pH value during the deposition process.

Nanowires have been deposited with varying the potential from -0.6 to -0.9 V. All other deposition conditions, including the pH value and the deposition time remained constant. A starting potential of -0.6 V has been chosen, as Co and Pt can be co-deposited at this potential. The influence of the deposition potential on morphology and composition has been studied. It is observed from the SEM micrographs (Figure 36) that the nanowires are well isolated and parallel to each other.

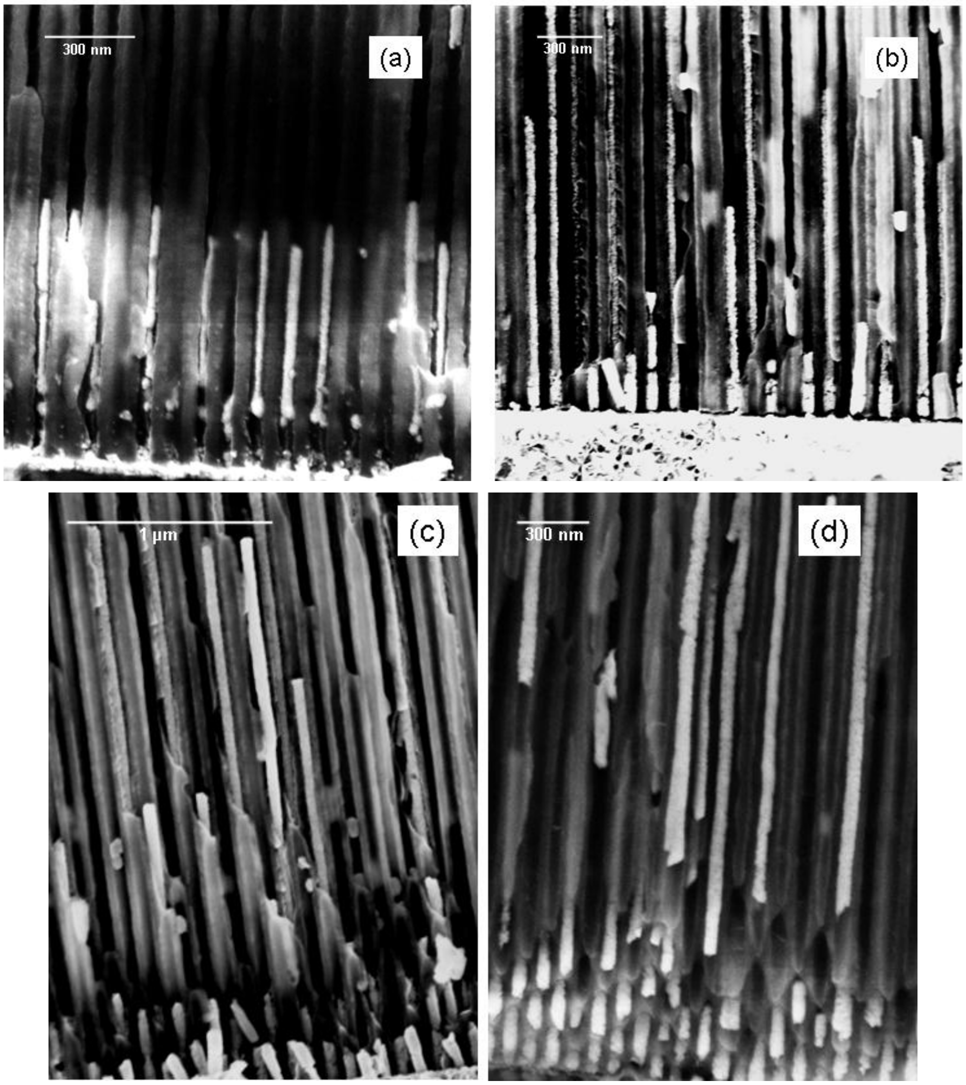

Figure 36: SEM images of Co-Pt nanowires taken at the crack surface of the templates. The nanowires are deposited at different potentials -0.6 V (a), -0.7 V (b), -0.8 V (c) and -0.9 V (d).

Co-Pt nanowires deposited at -0.6 V are smooth (Figure 36 (a)), compared to those deposited at -0.7 V which are discontinuous (Figure 36 (b)). With a decrease in the deposition potential the smoothness is improved (see Figure 36 (c) and (d)).

The composition of the nanowire arrays can be controlled by the deposition potential. At a low negative potential (-0.6 to -0.65 V) mainly Pt is deposited (see Figure 37). The deposition of Co-rich Co-Pt nanowires starts at -0.7 V (78 at. % Co). With a further decrease in the deposition potential (below -0.75 V) mainly Co is deposited. The average composition of Pt in the nanowires for the sample deposited at -0.6 V is ~ 86 at. % Pt, which is decreased to ~ 3 at. % Pt for the sample deposited at -0.9 V.

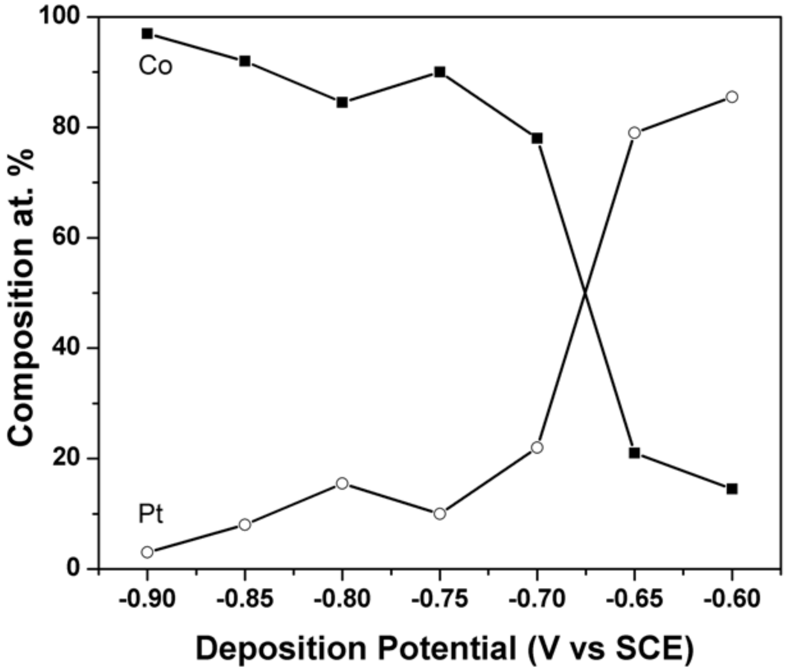

Figure 37: Variation of nanowire composition with deposition potential.

The variation of the length and the aspect ratio of the nanowires are plotted in Figure 38. The nanowires deposited at -0.6 V are shorter in length (~ 1 μm). The length of the nanowires is increased from ~ 2 μm to ~ 5 μm, as the deposition potential is decreased from -0.7 V to -0.8 V. Co-Pt nanowires deposited at the more negative potential of -0.9 V are ~ 14 μm in length.

As the pore diameter of the alumina templates used in our experiments is ~ 70 nm, an aspect ratio of more than 10 is achieved for these nanowires (Figure 38). For this aspect ratio, the effective anisotropy is controlled by the shape in addition to the magnetocrystalline anisotropy. This is due to the low demagnetization field contribution for the nanowires magnetized along their axis[92] as discussed in section 1.1.

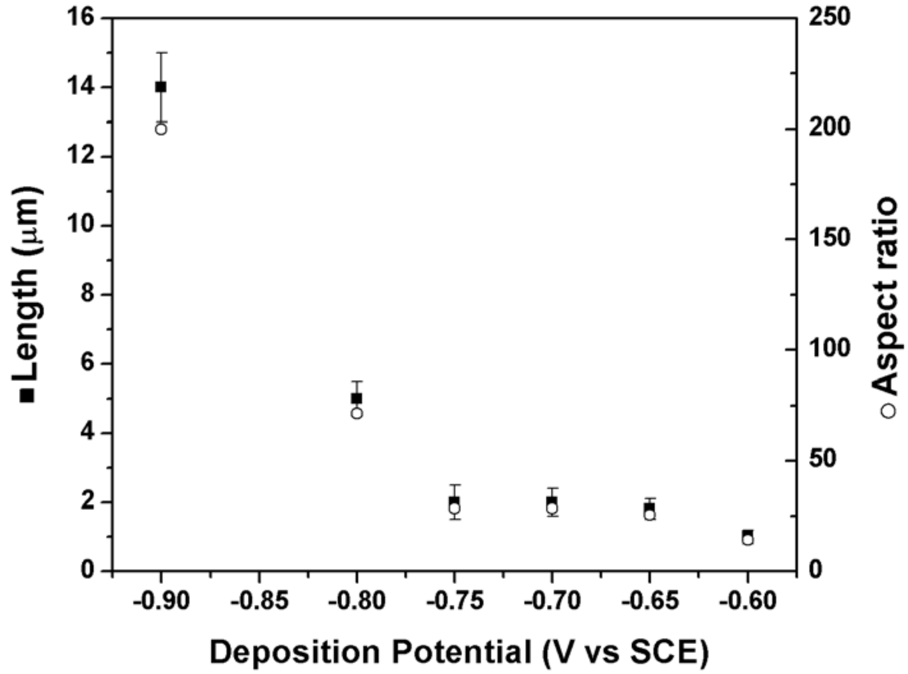

Figure 38: Variation of nanowire length and aspect ratio with deposition potential.

4.2 XRD in the as-deposited state

X-ray diffraction measurements have been carried out for Co-Pt nanowire arrays deposited at different potentials (Figure 39). The perpendicular lines in the XRD patterns are drawn for the 2θ values taken from the literature for Au, Pt and Co-Pt reflections. The XRD pattern shows reflections for (111) and (200) Au and (111) and (200) Pt. These Pt reflections originate from the back side of the membrane. There is no reflection originating from Co-Pt nanowire arrays, indicating that the as-deposited nanowires are either nanocrystalline or amorphous, in agreement with previous reports[74].

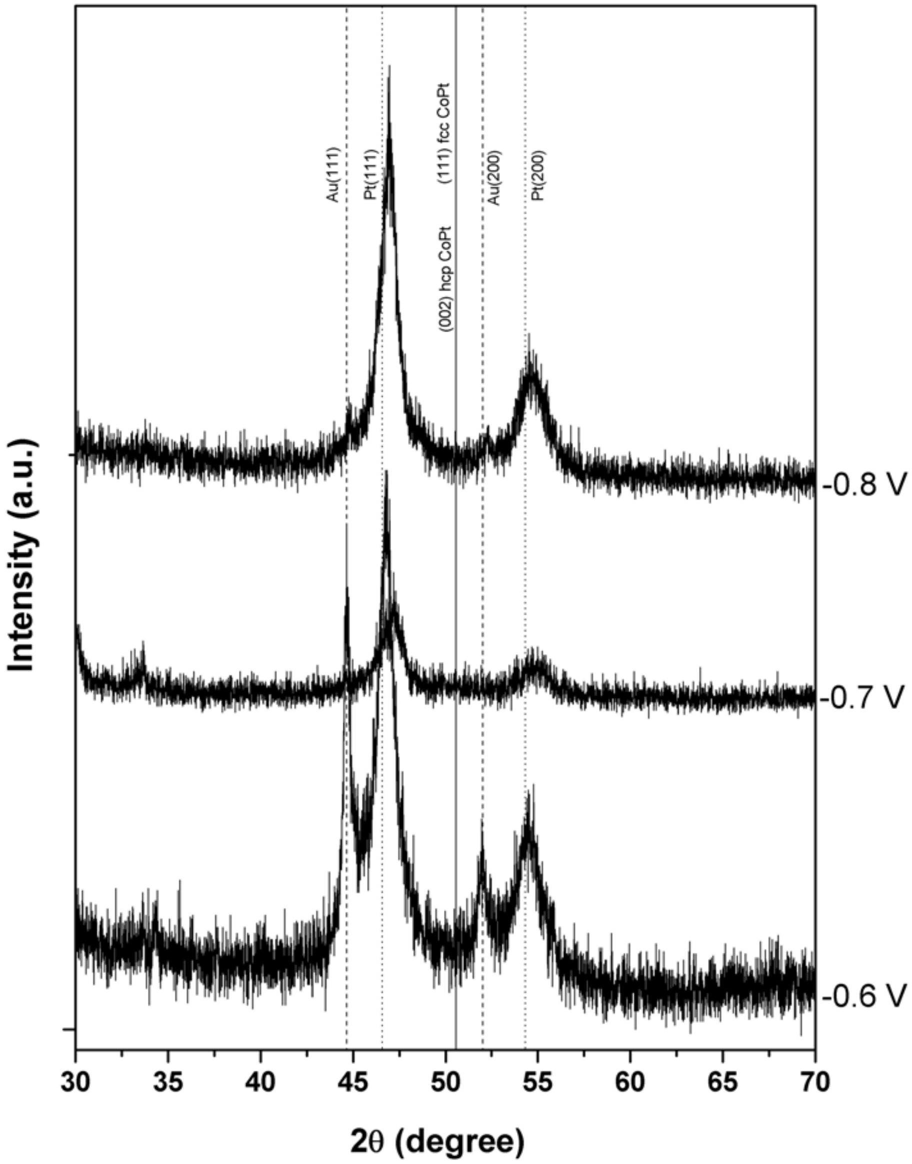

Figure 39: XRD patterns of Co-Pt nanowire arrays in AAO templates deposited at different potentials.

4.3 Magnetic properties and their correlation with deposition potential

Exemplary hysteresis curves for four samples deposited at different potentials are shown in Figure 40. These nanowires exhibit a change in anisotropy with deposition potential. Co-Pt nanowires deposited at -0.6 V are isotropic (Figure 40 (a)). The

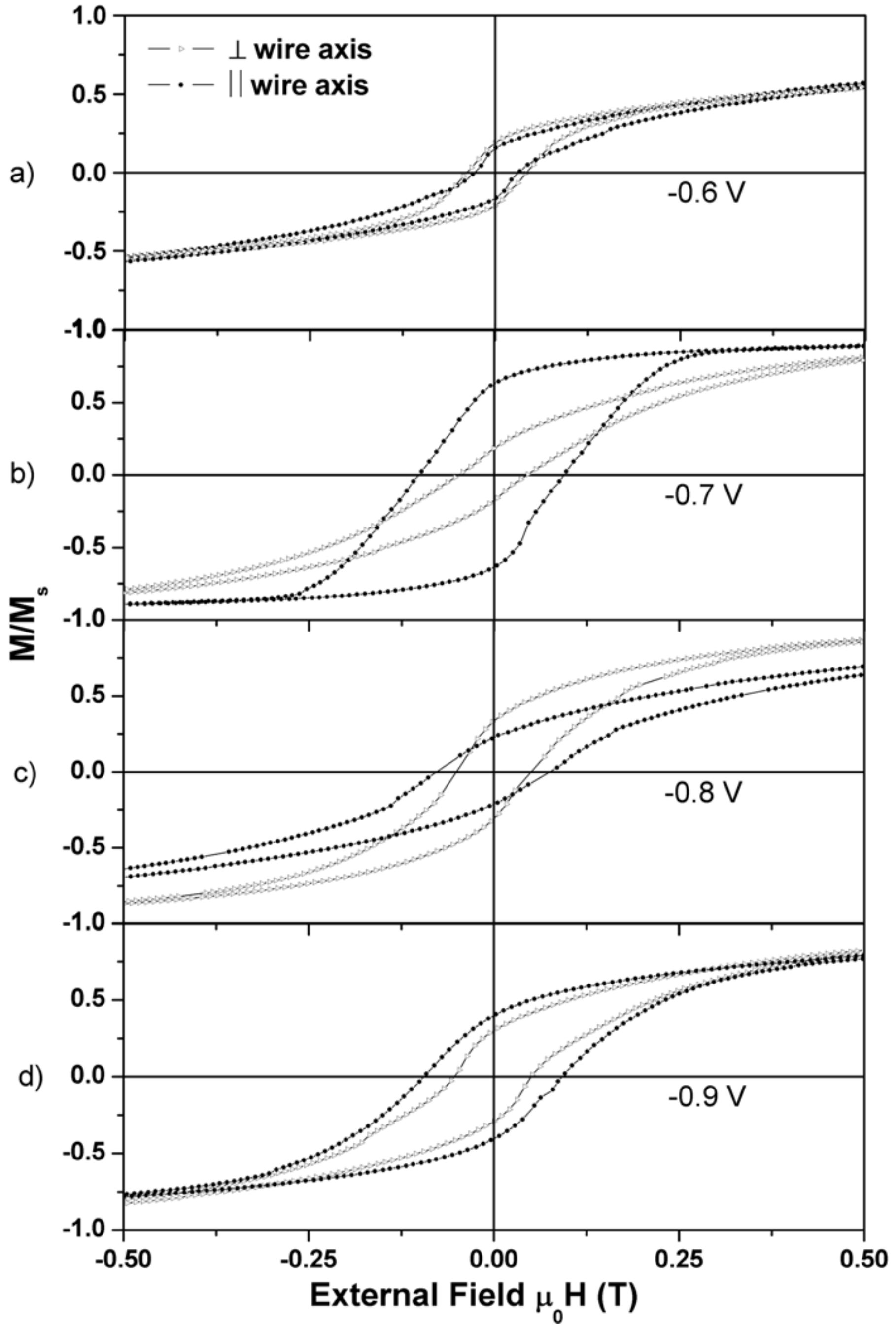

Figure 40: Hysteresis loops of Co-Pt nanowire arrays measured at room temperature with the field applied perpendicular (open triangles) or parallel (solid circles) to the axis of the nanowire, and deposited at -0.6 V (a), -0.7 V (b), -0.8 V (c) and -0.9 (d). The magnetization was normalized to a field value of 3 T (outside the range presented here).

coercivity measured along the wire axis (0.03 T) is slightly lower compared to that measured perpendicular to the wire axis (0.04 T). After deposition at -0.7 V, the nanowire arrays exhibit a strong anisotropy along the wire axis, since the remanence parallel to the wire axis significantly exceeds the remanence measured perpendicular to the wire axis. The coercivities measured parallel and perpendicular to the wire axis are 0.1 T and 0.05 T, respectively (Figure 40 (b)). Nanowires deposited at -0.8 V have a weak anisotropy perpendicular to the wire axis (Figure 40 (c)). The coercivity measured parallel to the wire axis is decreased to 0.07 T, while it doesn’t change perpendicular to the wire axis. Hysteresis curves measured for nanowire arrays deposited at a more negative potential, i.e. -0.9 V, are almost isotropic (Figure 40 (d)), with coercivities of 0.09 T and 0.06 T measured parallel and perpendicular to the wire axis.

The variation of coercivity and magnetic texture $M_R^{//} / M_R^{\perp}$ with deposition potential is summarized in Figure 41.

It can be concluded from the magnetic measurements that at a low negative potential (-0.6 to -0.7 V) the easy axis is mainly controlled by the shape anisotropy of the nanowire. This is expected to be due to the low cobalt content (from -0.6 to -0.65 V), where the fcc structure exhibiting a low anisotropy is formed. A low coercivity and and a low remanence are also expected for the nanowires deposited at -0.7 V due to their rough and discontinuous morphology (Figure 36 (b)). There is a significant increase in coercivity parallel to the wire axis when changing the potential from -0.6 V to -0.7 V, which may be due to the increased spontaneous magnetization, due to an increase of the Co content. Similar findings have been reported by Li *et al.*[93] for cobalt nanowires. They have reported that the effective anisotropy of fcc cobalt nanowires is mostly determined by shape anisotropy. As a result, cobalt nanowire arrays with fcc structure exhibit a higher coercivity than those with hcp structure. This is due to the low demagnetization factor along the nanowire axis, as discussed in section 1.1. When comparing it with the Co-Pt films, deposited at low current densities, have in-plane anisotropy. This is due to the low demagnetization field contribution along the film plane.

At more negative potentials, the nanowires exhibit a weak anisotropy perpendicular to the wire axis, as the curve measured parallel to the wire axis is slightly sheared

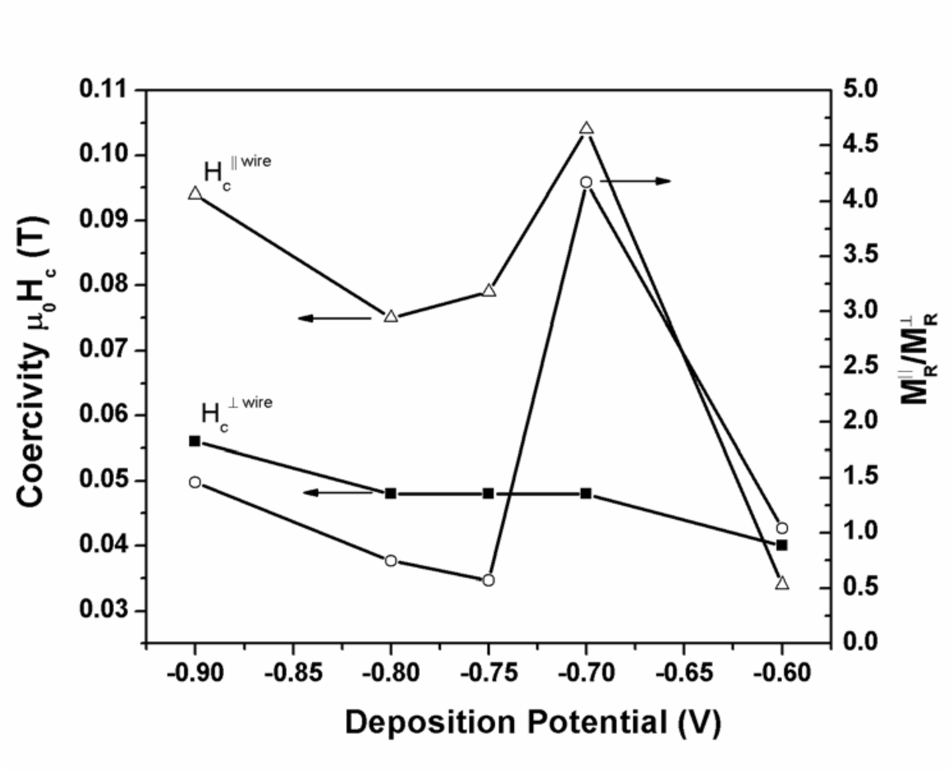

Figure 41: Variation of coercivity and magnetic texture of Co-Pt nanowires with deposition potential.

(-0.80 V; Figure 40 (c)), or they are isotropic (-0.9 V; Figure 40 (d)). From SEM micrographs (see Figure 36 (c), (d)) of these samples (-0.8 and -0.9 V) a high coercivity and a high anisotropy is expected parallel to the wire axis, due to their smooth and continuous morphology. This change in anisotropy with deposition potential is presumably due to an increase of the hcp phase in the nanowire arrays, as these nanowires contain higher amount of cobalt (~ 90 to 97 at. %).

It has been reported by Li *et al.*[93] and by Piraux *et al.*[94] that, for hcp cobalt, the magnetocrystalline anisotropy (~ $5x10^5$ J/m^3) is comparable to the shape anisotropy (~ $6x10^5$ J/m^3). Thus, the effective magnetic anisotropy is determined both by magnetocrystalline anisotropy and by shape anisotropy. This holds in particular, if the c-axis of the hcp cobalt is aligned preferentially perpendicular to the nanowire axis. Indeed, this texture has been reported by Bantu *et al.*[95] for Co nanowires. Similar findings have been reported by Cho *et al.*[96] for hcp cobalt nanowires.

4.4 Temperature dependent study in the as-deposited state

To investigate the effect of the magnetocrystalline anisotropy, temperature dependent measurements have been performed. In Figure 42, hysteresis curves measured between 50 and 400 K are shown. The key extracted data (coercivity and remanence ratio) in Figure 43 show the temperature dependence of coercivity in the parallel and perpendicular field directions. At 400 K coercivities of 0.09 T and 0.05 T are obtained parallel and perpendicular to the nanowire axis, respectively. As the temperature is decreased from 400 K to 50 K the coercivity increases for both directions. At 50 K it increases to about 0.15 T and 0.08 T parallel and perpendicular to the nanowire axis. In the whole temperature range, the coercivity in the parallel direction is larger than that in perpendicular direction. This shows the obvious anisotropy along the wire axis over the complete temperature range. The remanence ratio however decreases significantly at lower temperatures. At 400 K, remanence ratio $\left(M_R^{//} \middle/ M_R^{\perp} \right)$ is 4.43 and approaches 1 at 50 K. This behavior can be attributed to the isotropic orientation of easy axis, as reported by Khurshid *et al.*[97]. Due to the random distribution of easy axis, coercivity increases in both directions at low temperatures. As shape anisotropy becomes less important, since shape doesn't change with the temperature. The magnetization does only marginally increase with decreasing temperature. Magnetocrystalline anisotropy caused by the spin-orbit interaction is quite often increases with decreasing temperature[76,92]. From these measurements it can be concluded that, these nanowires may be nanocrystalline and are not amorphous, as magnetocrystalline anisotropy contributes at low temperatures.

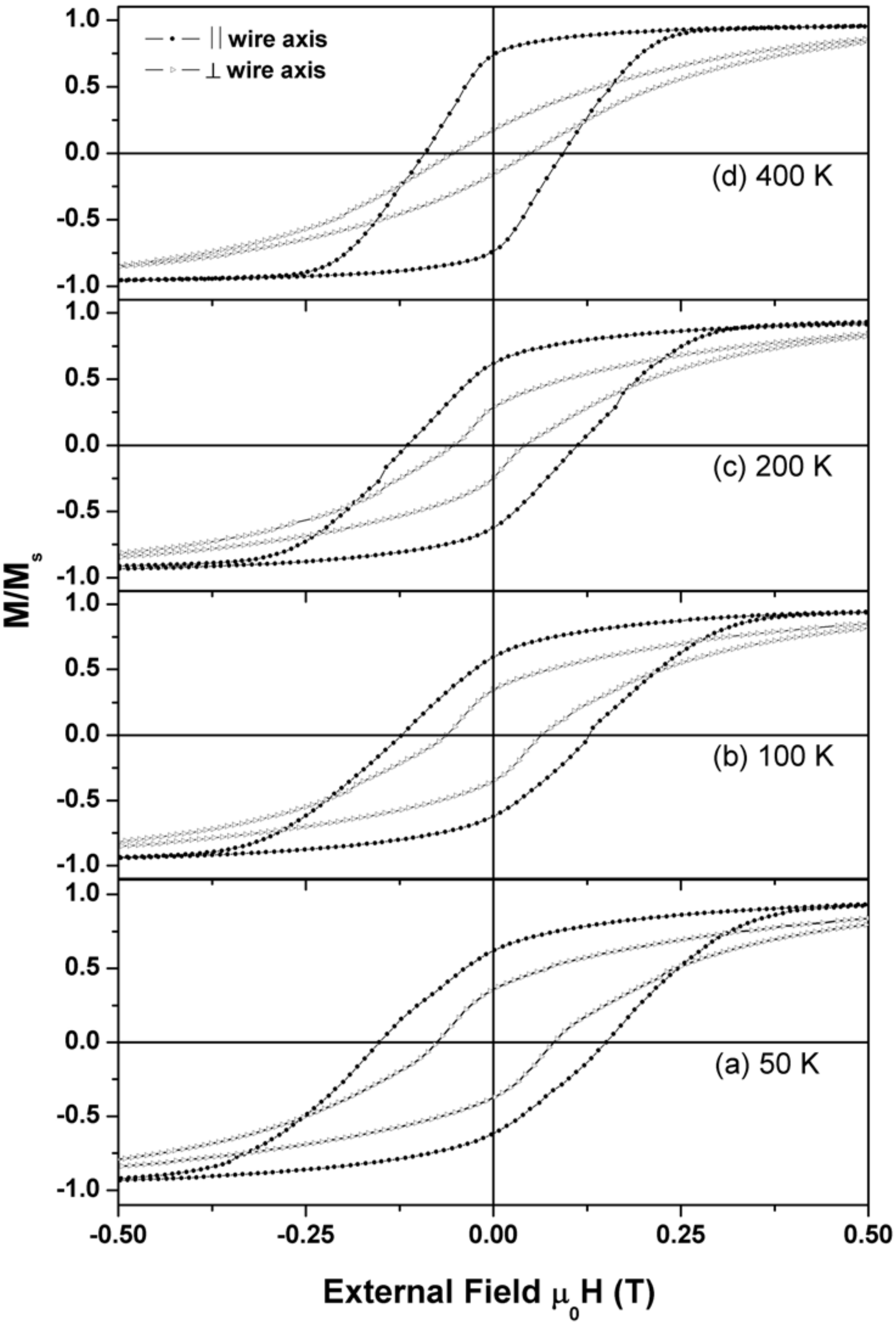

Figure 42: Hysteresis curves of Co-Pt nanowires measured at different temperatures (deposited at -0.7 V).

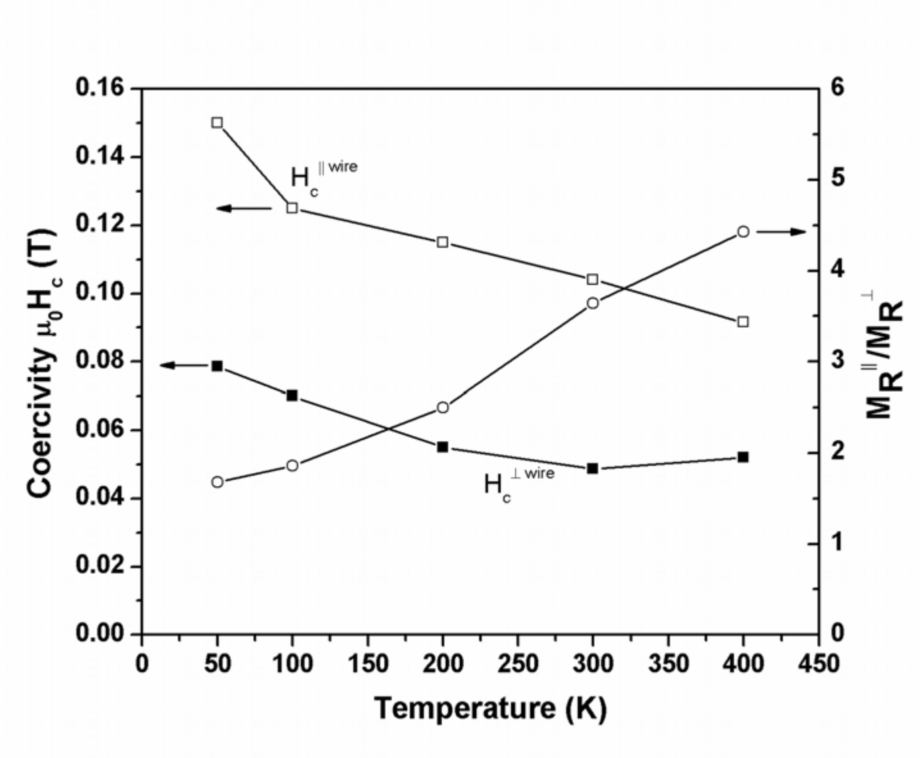

Figure 43: Coercivity (parallel and perpendicular to the wire axis) and remanence ratio of Co-Pt nanowires vs. temperature (deposited at -0.7 V).

Co-Pt nanowires deposited at -0.8 V exhibit a weak anisotropy perpendicular to the wire axis (see Figure 44). This could be due to the increased contribution from magnetocrystalline anisotropy, as these nanowires contain a higher amount of cobalt compared to the sample deposited at -0.7 V.

The temperature dependent study has shown a similar trend as observed for the nanowire arrays deposited at -0.7 V. With decrease in temperature from 400 K to 50 K, the coercivity increases from 0.06 T to 0.12 T parallel and from 0.05 T to 0.09 T perpendicular to the wire axis (Figure 45). This increase in coercivity in both directions can be attributed to the random orientation of the easy axis.

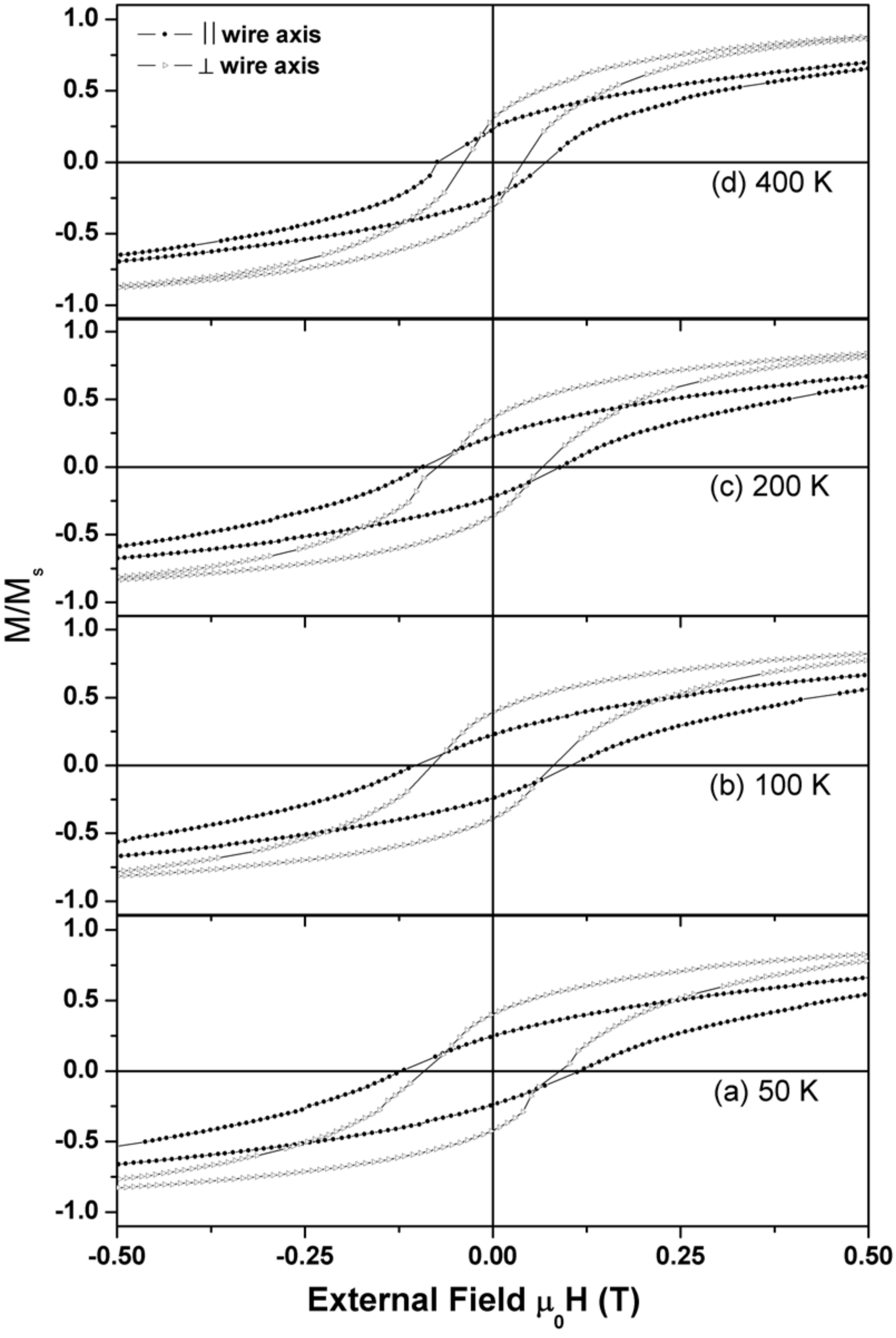

Figure 44: Hysteresis curves of Co-Pt nanowires measured at different temperatures (deposited at -0.8 V).

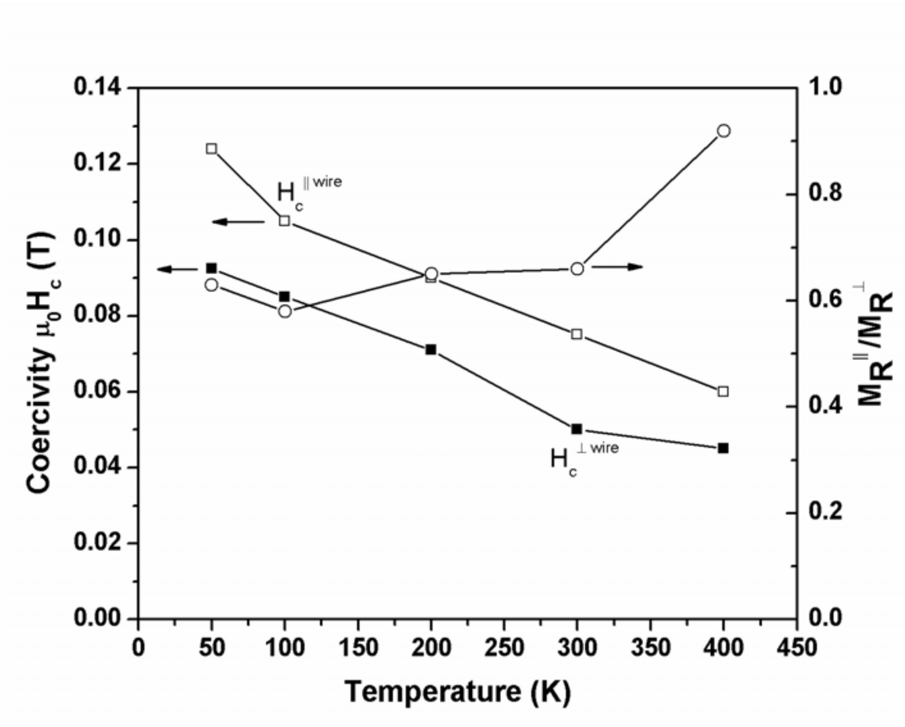

Figure 45: Coercivity (parallel and perpendicular to the wire axis) and remanence ratio of Co-Pt nanowires vs. temperature (deposited at -0.8 V).

The decrease in remanence ratio $\left(M_R^{//} \big/ M_R^{\perp} \right)$ from 0.92 to 0.63 with temperature indicates that the nanowire arrays have a weak anisotropy perpendicular to the wire axis. This shows that in this case the magnetocrystalline anisotropy seems to dominate over shape anisotropy. However, this requires at least a slight preferential orientation of the easy axis perpendicular to the wire axis. This kind of texture has been indeed reported for pure Co nanowires[93].

Chapter 5

Co and Co-Pt within polymeric templates

Continued advances in technologies such as magnetic storage and optoelectronics depend crucially on the ability to produce ultrahigh density arrays of nanometer-scale elements. As critical device dimensions shrink to the nanometer scale, the parallel fabrication of well-ordered arrays becomes increasingly difficult. Diblock copolymers have received much attention due to their ability to assemble into various ordered nanostructures. They do so in order to reduce the number of energetically unfavorable contacts between the two different blocks comprising the polymer molecule. It has been demonstrated by Thun-Albrecht *et al.*[57] that, by using diblock copolymer templates it is possible to fabricate magnetic arrays with densities in excess of 1 terabit per square inch. In particular, block copolymers have been used as templates for the synthesis of regular arrays of nanowires[57], nanolithography[62] and nanodots[98].

In this chapter, results on the deposition of Co and Co-Pt within diblock copolymer templates after using different pretreatment conditions will be presented. Finally, the microstructure of these deposits will be correlated with the magnetic measurements.

5.1 Electrodeposition of Co using different pretreatment conditions

Prior to the electrodeposition process, different pretreatment times have been used in order to wet the pores with the electrolyte. Although methanol can wet the pores, in the mean time collapsed poly (4-vinylpyridine) P4VP across the pore walls may also swell in methanol. Therefore, the templates have been wet in dilute methanol for different pretreatment times to avoid the swelling of P4VP. Here three samples deposited after wetting the template in dilute methanol (4 : 1; water : methanol) for 30, 90 and 120 seconds are presented. Finally, Co was electrodeposited by pulse plating after replacing the dilute methanol by the electrolyte. The deposition set-up and electrolyte system used for Co deposition has been discussed in section 2.4. The deposition was carried out by pulse plating, using a current of 4 mA as cathodic and anodic pulse for 10 and 2 ms, respectively. The total number of 250 sweeps has been used for the electrodeposition.

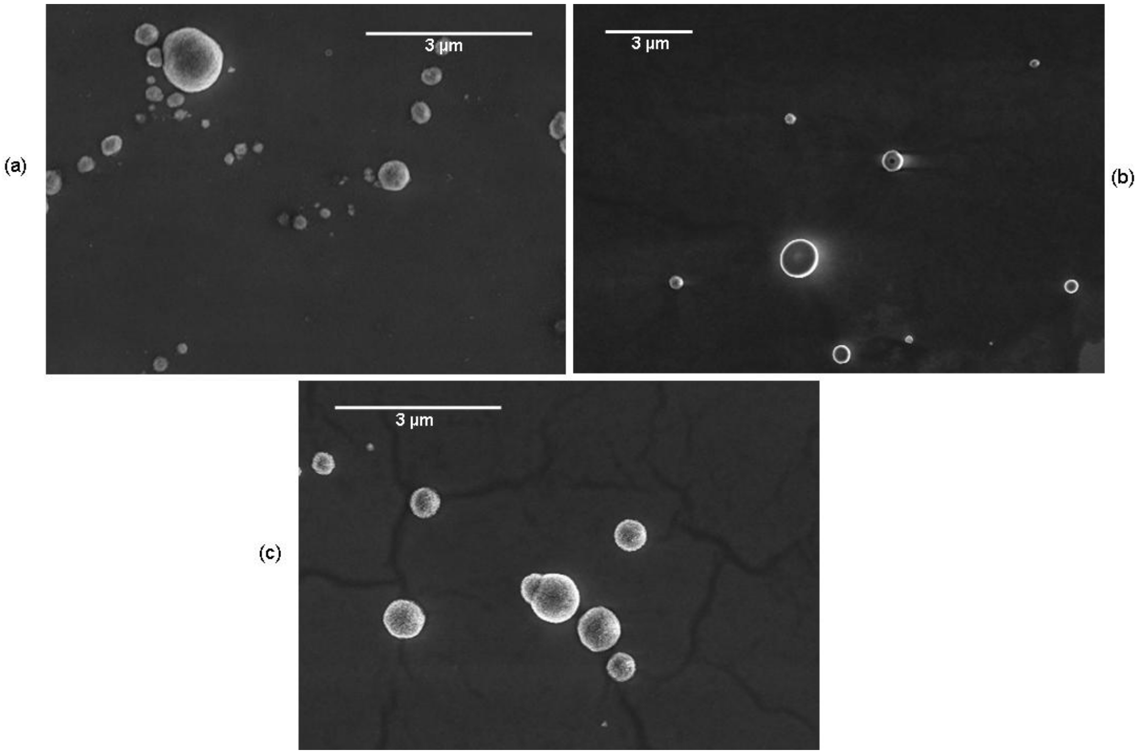

Figure 46: SEM images of the Co deposits after washing the template in chloroform for three different pretreatment times 30 s (a), 90 s (b) and 120 s (c).

SEM micrographs of these three samples are shown in Figure 46. For all three samples large deposits of ~ 0.5 to 1 μm in size can be seen on the top of the sample. The formation of these hemispherical Co deposits can be explained in the following way: The deposition may start from a defect site formed at the interface of substrate and barrier layer in the template and grow in size with the deposition time. The spot at the centre of the reversed hemispherical deposit (Figure 47) corresponds to the site from where the deposition starts and grows with deposition time. The schematic diagram of such a hemispherical deposit is sketched in Figure 47. Once the pore is overfilled, the deposit grows in size and starts filling the neighboring pores. This results in the formation of a hexagonal array of dots around the centre of the large deposit

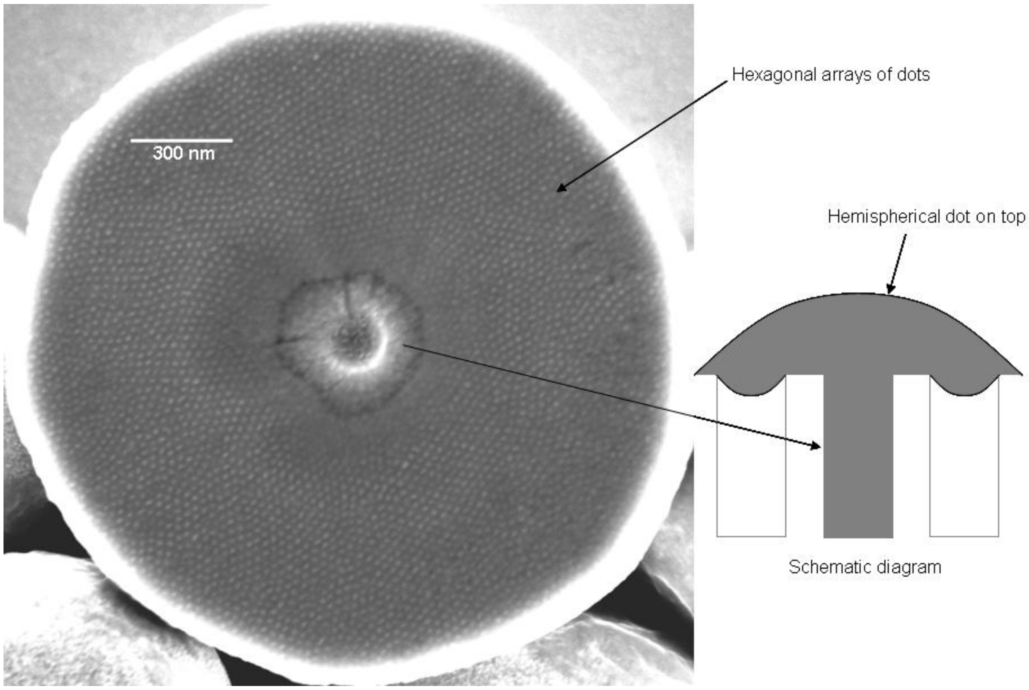

Figure 47: SEM image of a reversed hemispherical Co deposit after washing the template in chloroform and a schematic diagram of such a hemispherical dot formation.

It can be concluded from these observations that despite using different pretreatment times for the pore wetting, a homogeneous deposition of Co can not be achieved. The deposition of Co resulted in the formation of large hemispherical Co deposits on top of the template.

5.2 Electrodeposition of Co-Pt using different pretreatment conditions

Prior to the electrodeposition process, different pretreatment conditions have been used in order to wet the pores with the electrolyte.

One step process

In the one step process, electrodeposition was carried out directly after washing 2-(4-hydroxybenzeneazo) benzoic acid (HABA) in methanol to open the pores. The deposition set-up and the electrolyte system have been discussed in section 2.4. A SEM micrograph of the sample deposited at a current density of 36 mA/cm^2 is shown in Figure 48. Large deposits of ~ 0.5 to 1 µm size can be seen on the top of the sample. It has been confirmed by cross-sectional SEM that the pores below the large grains are only partially filled (Figure 49 (a)). No filled pores have been observed in between the large grains.

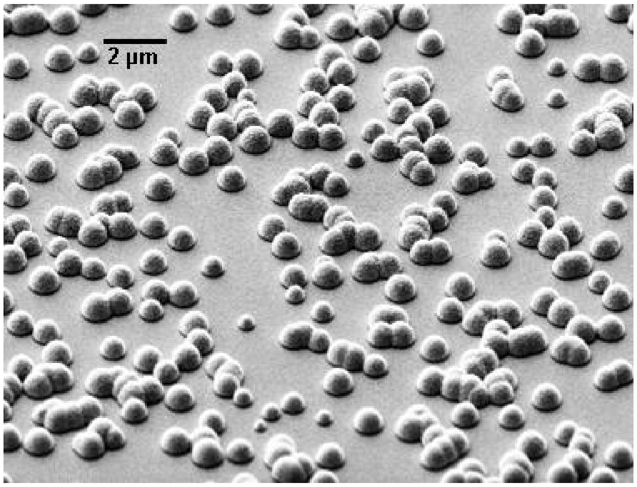

Figure 48: SEM image of the template filled with Co-Pt after a one step pretreatment.

Two step process

To improve the wetting of the pores, a two step process has been used. In this process, first HABA was washed in methanol and then 15 ml of methanol was added to the 30 ml of electrolyte in order to wet the pores with electrolyte. No improvement has been observed in the filling of Co-Pt into the template (see Figure 49 (b)). The formation of these hemispherical Co-Pt deposits on the top of the template can be explained in a similar way as discussed for Co in section 5.1.

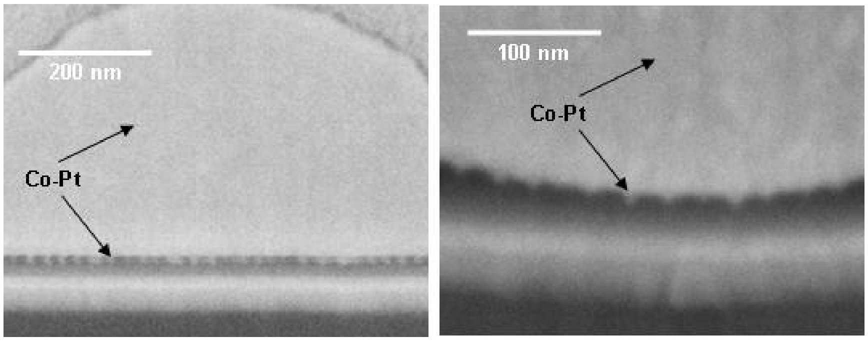

(a) One step (b) Two step

Figure 49: FIB cross-section of the template after electrodeposition of Co-Pt; after one step (a) and two step (b) pretreatment process.

Three step process

In the three step process, first HABA was washed in methanol. By this the P4VP chain swell, which closes the pores. Therefore, in the next step, dilute methanol has been used for 15 minutes in order to reduce the swelling of the P4VP chains. As a next step, dilute methanol was replaced by water and then the template was immersed in water for 10 minutes prior to electrodeposition. The reason for using water in the next step is to make the swelled P4VP chains to collapse across the pore walls. Similar to the previous pretreatment conditions large grains of Co-Pt have been observed on the top of the template.

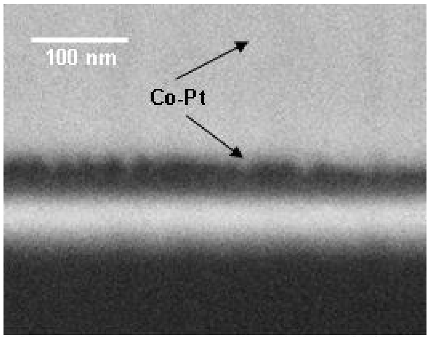

Three step

Figure 50: FIB cross-section of the template after electrodeposition of Co-Pt (three step pretreatment).

The cross-sectional image across one grain of Co-Pt is displayed in Figure 50, where pores below the large deposits are partially filled with Co-Pt.

From these different pretreatment conditions it can be concluded that the deposition occurs through the defects in the remaining polymer barrier layer (~ 2 nm) at the pore bottom. This barrier layer is formed by the collapsed P4VP chains after washing HABA in methanol (Figure 51 (a)). Although the rms roughness of the substrate is only ~ 0.5 nm, but due to the local roughness of the substrate kinks may form at the interface of barrier layer and substrate or electrode (Figure 51 (b)). Such kinks can form defects in the template, resulting in preferential nucleation sites for the deposition.

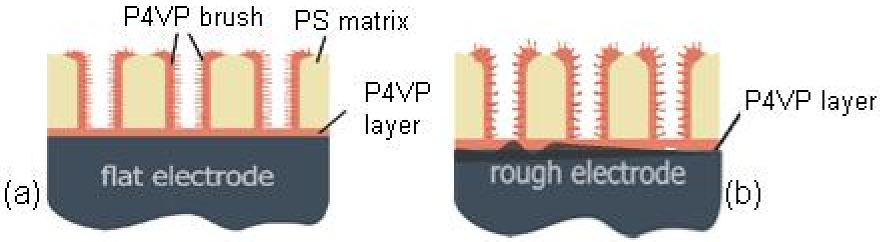

Figure 51: Schematic diagram of a diblock copolymer template on flat (a) and rough (b) substrates.

Alternatively this inhomogeneous deposition can be attributed to the nonuniform template thickness. Light microscope and SEM images of the diblock copolymer template are shown in Figure 52. Although the templates appear homogeneous on a small scale (Figure 20), on a larger scale they are inhomogeneous (see Figure 52). In both images there is a different contrast originating from the template, which very likely originates from the inhomogeneous thickness of the template.

In spite of the different pretreatment conditions, there occurs an inhomogeneous deposition of Co and Co-Pt within the template. Large deposits of Co or Co-Pt of ~ 0.5 to 1 μm size can be seen on the top of the sample. This inhomogeneous deposition can be attributed to defects and the nonuniform thickness of the template.

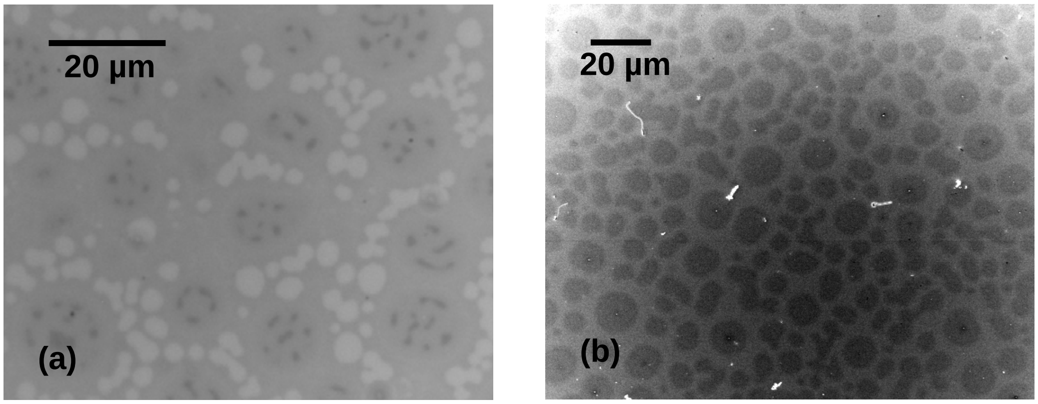

Figure 52: Light microscope (a) and SEM (b) images of a diblock copolymer template.

5.3 Magnetic properties of Co-Pt within polymeric template

Magnetic hysteresis loops of Co-Pt deposited at a current density of ~ 36 mA/cm^2 after different pretreatments have been measured. The hysteresis curves measured after the one step pretreatment process, with applied field parallel and perpendicular to the film plane, are compared in Figure 53. The magnetization is preferentially aligned in the in-plane direction. Coercivity values of 0.08 T are measured in both directions. Such a behavior is not expected for nanowires but can be attributed to the large grains on top of the template. As these hemispherical deposits of Co-Pt on top are larger in diameter than in height, the in-plane direction should be slightly favorable[99].

A similar magnetic behaviour was observed for the other samples. This agrees with the microstructural analysis, revealing almost no filling of the isolated pores, but only the formation of hemispheres on the top of the sample.

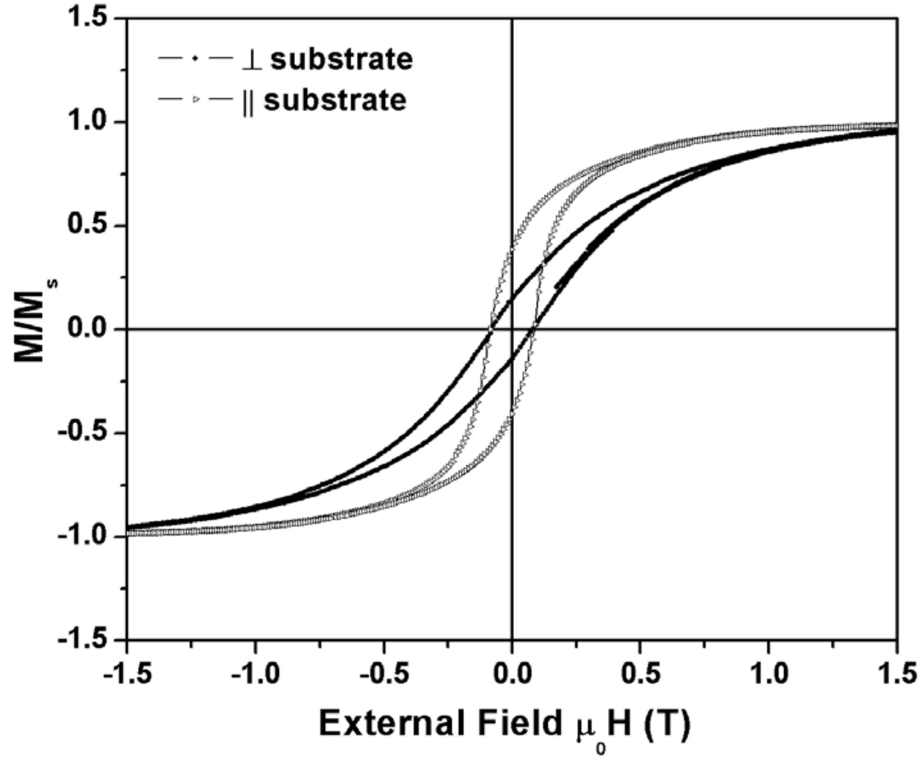

Figure 53: M–H curves for Co–Pt deposited into the pores at a current density of ~ 36 mA/cm^2, directly after deposition; the curves were measured at 300 K with the applied field parallel and perpendicular to the substrate.

Chapter 6

Magnetic properties of rolled-up microtubes

6.1 Motivation

Rolled-up micro-and nanotubes[100,101] have been created from a wide variety of material combinations[102,103,104,105] and are promising candidates for waveguides[106,107], ring resonators[108], transport experiments[109] as well as electronic[110] applications. A good control over size[8] and lateral position[111] of nanotubes has been exerted, raising the legitimate hope for a future scalable and highly integrative nanotechnology. More recently, a method to rearrange prestressed nanomembranes into microtubes on polymers has extended the range of material systems, including magnetic materials[10,112]. This technique allows the fabrication of individual tubes as well as large tube arrays in a controlled way. The magnetic tubes created in this fashion have been employed as remotely controlled microjet engines[4] and magnetofluidic sensors[5]. The magnetic tubes presented here are the subject of fundamental studies due to the change of magnetic properties after the roll-up process

6.2 Fabrication of rolled-up microtubes

Strain engineering has been used to prepare rolled-up microtubes based on semiconductor materials in the past years[9,113]. There are two methods for making these solid-state nanotubes (Figure 54 (a) and (b)), involving a ‘general’ and a ‘specialized’ method[101]. In a general method an etchant-sensitive material is deposited on a substrate surface. On top of this sacrificial layer, a thin film (or a series of thin films) is deposited. After selective etching of the sacrificial layer, the thin top layer is wrapped up and folded back onto the sample surface, where it can bond to itself. At the position where the layer bends, a nanotube has formed (Figure 54 (a)). In case of a ‘specialized’ method the layer sequence consists of an etchant-sensitive material, followed by a bilayer of two different materials (materials 1 and 2). Material 1 has a compressive stress relative to the tensile stress in material 2. Once the bilayer is released by selective etching, the material tends to acquire its inherent lattice constant. The bilayer bends upwards, finally forming a nanotube after one complete revolution (Figure 54 (b)). Both rely on the release of thin layers of the material from a substrate by a selective etching procedure. The position of the nanotubes is exactly determined by the etching time. Controlling the thickness of the layers and hence of the tube walls depends on the deposition time and can be as precise as a single atomic layer.

The microtubes presented here are prepared by the roll-up of a corresponding Au/Co/Au layer stack[11]. Tubes have been prepared by Dr. C. Müller in the Institute for Integrative Nanosciences of Prof. Dr. O. G. Schmidt at the IFW. The tube diameter is shown to be scalable with the metal film thickness, while their lengths are predefined by the lithographically adjusted pattern size.

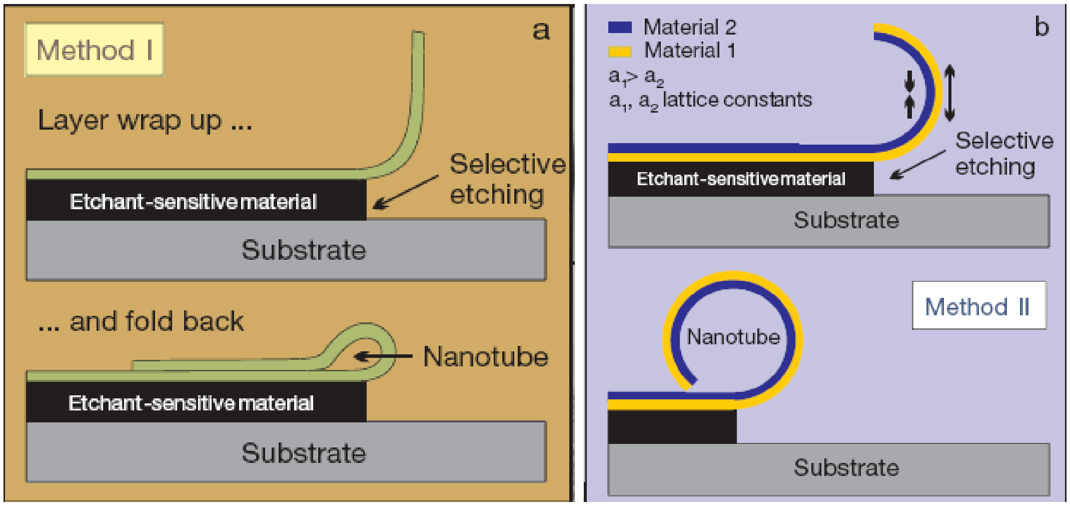

Figure 54: schematic illustration of the formation of solid state nanotubes: (a) General method to create a nanotube and (b) Specialized way to create a nanotube[101].

To fabricate the rolled-up microtubes, photoresist layers with a thickness of ~ 2 µm on Si (001) are patterned into well-defined squares (20 x 20, 50 x 50, and 100 x 100 μm^2) by conventional photolithography. Thin Au (4 nm) /Co (*x*) /Au (4 nm) layers were deposited by electron beam deposition at a pressure of < 10^{-4} Pa onto the photoresist layer. A Co film thickness *x* between 7 and 22 nm was used. Using inclined deposition, one side of the photoresist edge becomes covered, which facilitates a rolling up of the film in a predefined direction. Subsequently, the Au/Co/Au films are rolled-up by dissolving the photoresist layer with acetone. In order to avoid deformation or collapse of the structures, the organic solvent was removed afterward using a drying step.

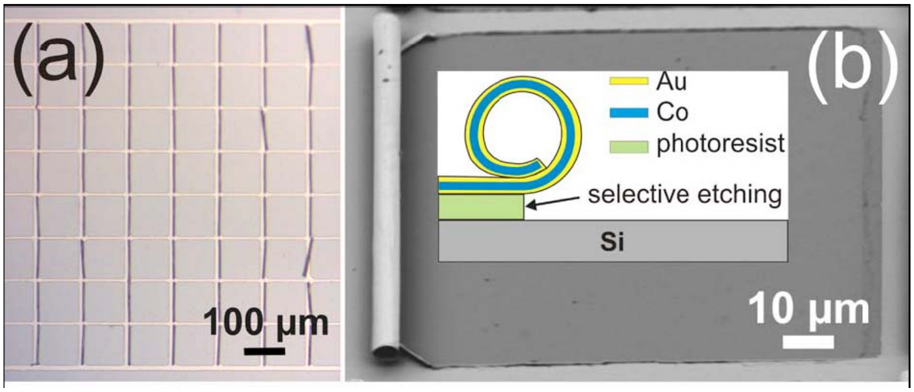

Figure 55: Optical microscope image of a periodic microtube array obtained after roll-up of 4 nm Au/10 nm Co/4 nm Au trilayers (a) and SEM image of a microtube with a diameter of roughly 5 µm (b). The inset schematically describes the roll-up process.

Figure 55 (a) shows an optical microscopy image of well aligned Au/Co/Au microtubes. Each of them was obtained from a 100 µm x 100 µm large film square. After releasing the prestressed layers, the fraction of microtubes amounts to 90% of the magnetic material, whereas the rest of 10 % originates from the Au/Co/Au film located in between the rolled-up areas (bright stripes in Figure 55 (a)). A SEM image of a typical single microtube with a diameter of ~ 5 µm and a sketch of the rolling process are illustrated in Figure 55 (b). The driving force for roll-up is the relaxation of stress gradients across the metallic layer stack depending on the deposition parameters (growth rate and substrate temperature). A variation of the metal layer thickness allows to tune the tube diameter between ~ 2 and ~ 11 µm, corresponding to tube with one to ten windings.

From a cross-sectional TEM micrograph, the estimated thickness, evaluated from different material contrast, is ~ 3 nm for the Au layers and ~ 12 nm for the Co layer. The tube diameter is ~ 5 µm which corresponds to 2 windings.

6.3 Magnetic measurements

In order to study the difference of the magnetic properties of the Au/Co/Au films and the corresponding rolled-up tubes, magnetic measurements have been performed. Figure 56 presents typical magnetization curves for the Au/Co/Au films and the corresponding rolled-up tubes measured at 300 K. These measurements were performed with the same samples used for the structural investigations. Measurements of the film (Figure 56 (a)) perpendicular to the substrate surface reveal a hard axis loop with a low slope and a low coercivity H_c of 12 mT, as expected due to shape anisotropy. The saturation magnetization M_S for the film is close to the value for bulk Co ($1.4\text{x}10^6$ A/m). Unexpectedly, a pronounced difference is observed when measuring hysteresis loops for different directions within the film plane. Measurements along 90° (the direction of the inclined deposition) exhibit a typical easy axis rectangular loop with H_c of 17 mT. The coercivity along 0° is smaller (10 mT), and the curve is significantly more tilted. The intersection of both in-plane curves gives an average anisotropy field of $H_A = 2K/M_S$ of 12 mT, which is equal to an anisotropy constant of $K = 8\text{x}10^3$ J/m^3. The absence of hcp Co reflections within the XRD measurements as well as the absence of any pronounced microstructure in the TEM images allows to attribute this anisotropy entirely to stress. The difference of stress along both in-plane directions can be estimated from $K = \frac{3}{2}\lambda_s\sigma$, where λ_s is the magnetostrictive constant and σ is the stress[88]. Using the value[114] $\lambda_s = -62\text{x}10^{-6}$ for Co one obtains a difference of stress between both in-plane directions of ~ 86 MPa. The sign suggests a more compressive stress along 90° compared to the 0° direction ($\sigma_{0^0} - \sigma_{90^0} < 0$). As a conclusion, the orientation of the easy axis seems to be supported by this external uniaxial stress, which was induced during the deposition process.

After roll-up the magnetization behavior changes completely (Figure 56 (b)). First, the magnetic in-plane anisotropy is reversed, and the magnetic saturation field along the out-of-plane direction is significantly decreased. The observed curve shape suggests that shape anisotropy tries to locally align the magnetization within the tube surface, but the integral VSM measurements average over all directions of the local surface with the direction of the applied field. Second, since stress release only occurred along 90° ($\sigma_{90^0} = 0$), just the lower compressive stress along 0° ($\sigma_{0^0} < 0$) remains. Hence, the easy axis of magnetization is now aligned along 0°. In comparison to the film, H_c along the easy axis is smaller and amounts to 13 mT. For tubes with an ideal cylindrical cross-section the directions normal to the tube axis are expected to be equal. In fact, identical values for H_c of 11 mT are obtained, but small differences in the slope of the hysteresis are observed. These small differences may originate from deviations of the ideal cylindrical structure. As already described, a small continuous film contribution is superimposed in these hysteresis loops.

In addition to the measurements at room temperature, the hysteresis of the tube array after field cooling (FC, +0.5 T, along the tube axis) was measured at low temperatures. The shifted hysteresis, exemplarily shown for 20 K (Figure 57 (a)) suggests a pronounced negative exchange bias (EB) effect due to the exchange coupling at ferromagnetic/antiferromagnetic interfaces[115]. The presence of small amounts of O within the samples in the EDX measurements (not shown here) can be an indication that some antiferromagnetic cobalt oxide was formed. The EB field H_E is obtained from $H_E = \left| H_{c(+)} + H_{c(-)} \right| / 2$, where $H_{c(+)}$ and $H_{c(-)}$ are the coercive fields

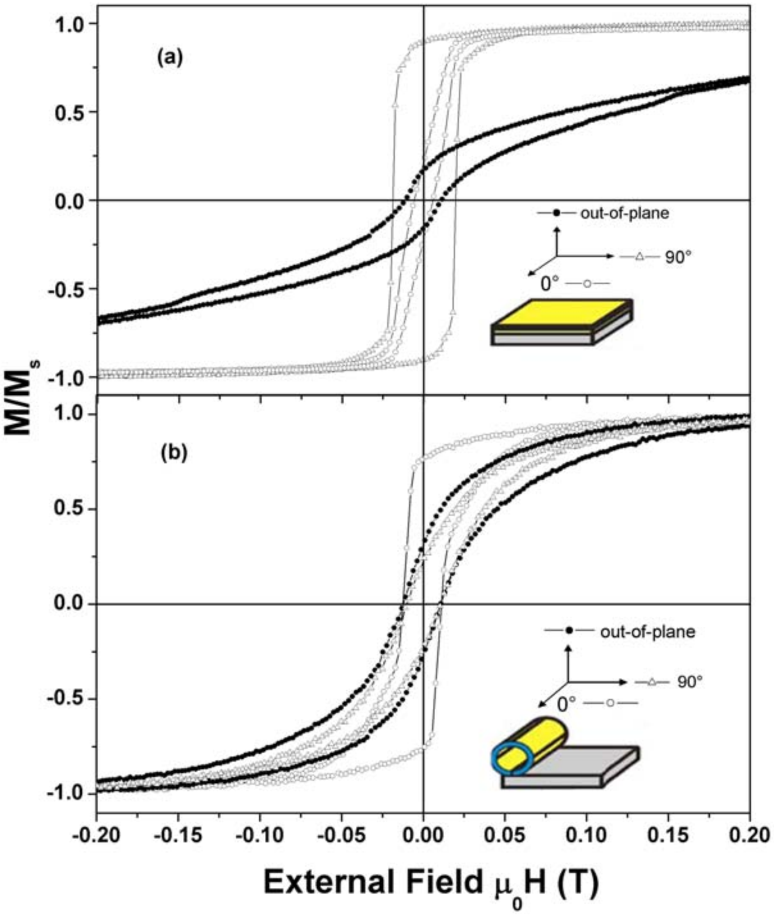

Figure 56: VSM hysteresis loops of (a) a 4 nm Au/10 nm Co/4 nm Au film array and (b) the corresponding tube array after the roll-up process at 300 K. The insets show the directions of the applied magnetic field.

determined on the positive and the negative field sweeping directions. At 20 K the FC curve exhibits a hysteresis loop shift H_E of 24 mT and a coercivity $H_{c(-)}$ of 3 mT. From the FC hysteresis loops measured between 20 and 300 K, the values for $H_{c(+)}$ and H_E were extracted and plotted as a function of the temperature (Figure 57 (b)). It is found that H_E strongly increases when measuring below the EB blocking temperature of T_b ~ 100 K. On the other hand, $H_{c(+)}$ first increases when reducing the temperature, which can be attributed to thermal fluctuations, but drops as H_E increases. The latter observation indicates that the anisotropy causing $H_{c(+)}$ is aligned in a different direction compared to the magnetic field applied during FC (see Figure 57 (a)). The drop in $H_{c(+)}$ can be explained when considering the different thermal expansion coefficients α for Co and Si ($\alpha_{Co} = 13 \times 10^{-6} K^{-1}$ and $\alpha_{Si} = 3 \times 10^{-6} K^{-1}$ at room temperature)[116] and adapting the model reported by Kumar *et al.*[117]. In the present case the tube length is considered to be constrained by the substrate whereas its diameter is free. Thus, when cooling from 300 to 20 K (ΔT = -280 K) and using the elastic modulus for Co (E_{Co} = 204 GPa at room temperature)[118] the stress σ_{0^0} amounts to ~ 570 MPa, with $\sigma_{0^0} = E_{Co}\Delta T(\alpha_{Si} - \alpha_{Co})$. This changes the stress along the tube axis from compressive ($\sigma_{0^0} < 0$) into tensile ($\sigma_{0^0} > 0$). As a consequence the magnetic anisotropy is reversed, observable from the change in slope in Figure 57 (a).

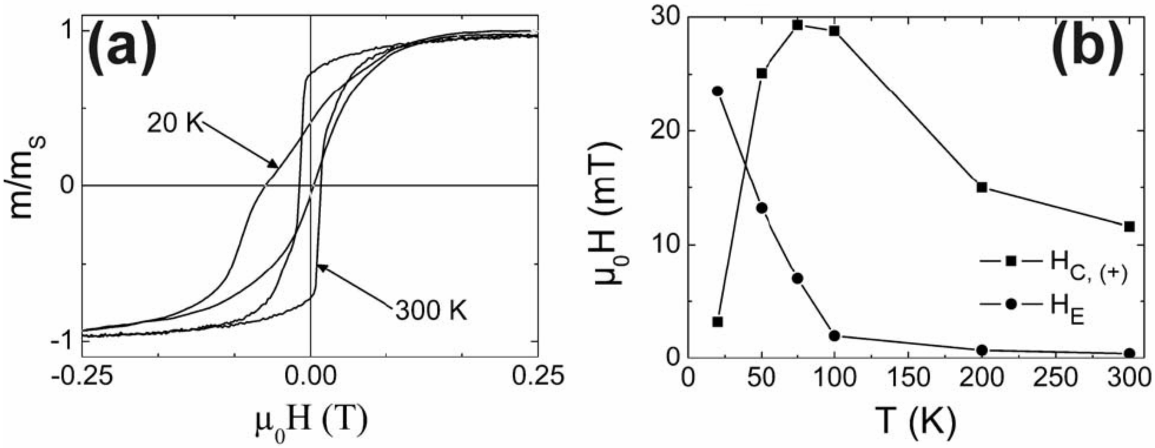

Figure 57: FC hysteresis loops at 20 and 300 K. (b) Temperature dependence of the coercive field $H_{C(+)}$ and of the EB field H_E of a Au/Co/Au microtube array after FC (+0.5 T). The field was applied along the tube axis.

Summary and outlook

In this work the influence of shape, magnetocrystalline and magnetostrictive anisotropy is examined in different types of magnetic nanostructures: films, nanowires and microtubes. Electrodeposition as well as physical deposition methods have been used to deposit Co and Co-Pt as magnetic materials. Since the single domain diameter (about 34 nm for hcp Co) is in the same order of magnitude as the smallest extension of all nanostuctures, the shape of these nanostructures strongly affects their magnetic properties.

This can be most directly examined when preparing Co-Pt under conditions which result in a fcc phase, exhibiting a low magnetocrystalline anisotropy (e. g. films deposited at low current density (10 mA/cm^2) or nanowires at low negative potential (-0.6 to -0.7 V)). In this case shape anisotropy favors an alignment of the magnetization along the long sample axis. Hence, for these samples the magnetization is aligned in-plane for thin films, along the wire axis in nanowire arrays and along the tube axis in rolled-up micotubes.

A variation of deposition conditions allows to increase the hcp content, exhibiting a significantly higher magnetocrystalline anisotropy (e.g. by increasing the Co concentration in films obtainable at high current density (30 mA/cm^2) or by using a more negative potential (-0.75 to -0.90 V) during the growth of the nanowires). For both cases, films and nanowires, the easy axis is aligned perpendicular to the long sample axis. For the thin films, this has been directly probed by pole figure measurements, while for the nanowires temperature dependent magnetization measurements have been used. For Co-Pt nanowires magnetocrystalline anisotropy increases at low temperatures, as a result it competes with shape anisotropy.

As the *fcc* and *hcp* structures are difficult to distinguish in nanostructured material, a dedicated approach to use pole figure measurements was developed. This method reveals a direct correlation of the structure with the magnetic properties. The ratio of the out-of-plane to the in-plane remanence as a measure of magnetic texture follows the same trend as the coercivity. Since the decrease in integrated intensity ratio and coercivity at highest current density (32 mA/cm^2) occur simultaneously in both independent probes (i.e. pole figures and magnetic measurements), the suggested approach of the structural analysis indeed probes the key origin of the intrinsic magnetic properties. In addition to current density, the age of the electrolyte used has a significant influence on composition, phase formation and thus on the magnetic properties. This instability of the Co-Pt electrolyte is attributed to the anodic oxidation of ammonium citrate in the presence of Co^{2+} ions, which has a significant influence on the deposition of cobalt based alloys.

For Co-Pt nanowires the contribution of the magnetocrystalline anisotropy is concluded from a cross-over behavior. At high temperatures the magnetization is preferentially aligned along the wire axis, while at lower temperatures the increased magnetocrystalline anisotropy tends to align the magnetization perpendicular to the wire axis. Similar to thin films, the deposition conditions strongly affect structure and magnetic properties of these nanowires. E.g. with a decrease in the deposition potentials (-0.75 to -0.90 V) an increase in the amount of the hcp phase is observed.

Several attempts have been carried out to fill the 8 nm pores of diblock copolymer templates with Co and Co-Pt by electrodepositon. Though wetting with the electrolyte have been identified as key problem, different pretreatment conditions had not been successful to obtain a regular, homogeneous filling. Instead of nanowires, the formation of large Co and Co-Pt hemispheres with diameters between 0.5 and 1 µm have been formed on top of the template had been observed. These hemispheres most probably originate from one single nanowire, which can be filled by electrodeposition. Once it is completely filled, radial growth on top of the template results in a hemisphere, growing partly into the empty pores. Magnetic measurements show that the easy axis of magnetization in this case is also controlled by shape anisotropy. A slight in-plane direction is favorable, as these hemispherical deposits of Co or Co-Pt on top are larger in diameter than in height.

Magnetic properties of Au/Co/Au films are strongly affected by the roll-up process. In addition to shape anisotropy the easy axis of the magnetization is controlled by magnetoelastic anisotropy. Since stress release only occurs perpendicular to the tube axis, a compressive stress along the tube axis remains, which was already induced during growth. Hence, the easy axis of magnetization changes by rolling-up. This effect was identified by analysing temperature dependent measurements. Due to the different thermal expansion coefficients of the microtube and the substrate, the stress along the tube axis changes from compressive to tensile during cooling. As a consequence the magnetic anisotropy is reversed.

Though in this work the key contributions of shape, magnetocrystalline and magnetostrictive anisotropy could be analyzed, some open questions remain. Ageing of the electrolyte had been identified to have a strong effect on composition, phase formation and magnetic properties of Co-Pt films, but further studies of the detailed electrochemical processes are required. First attempts were made to fill the diblock copolymer template with Co and Co-Pt, but certainly more work is to be done to achieve a homogeneous filling of this type of template.

References

---

[1] T. S. Chin. *Permanent magnet films for applications in microelectromechanical systems*. J. Magn. Magn. Mater. **209**, 75 (2000).

[2] T. Aoyama, S. Okawa, K. Hattori, H. Hatate, Y. Wada, K. Uchiyama, T. Kagotani, H. Nishio and I. Sato. *Fabrication and magnetic properties of CoPt perpendicular patterned media*. J. Magn. Magn. Mater. **235**, 174 (2001).

[3] C. Haginoya, S. Heike, M. Ishibashi, K. Nakamura, K. Koike, T. Yoshimura, J. Yamamoto and Y. Hirayama. *Magnetic nanoparticle array with perpendicular crystal magnetic anisotropy*. J. Appl. Phys**. 85**, 8327 (1999).

[4] Y. Mei, G. Huang, A. A. Solovev, E. Bermúdez Ureňa, I. Mönch, F. Ding, T. Reindl, R. K. Y. Fu, P. K. Chu and O. G. Schmidt. *Versatile approach for integrative and functionalized tubes by strain engineering of nanomembranes on polymers*. Adv. Mater. **20**, 4085 (2008).

[5] E. Bermúdez Ureña, Y. F. Mei, E. Coric, D. Makarov, M. Albrecht and O. G. Schmidt. *Fabrication of ferromagnetic rolled-up microtubes for magnetic sensors on fluids.* J. Phys. D: Appl. Phys. **42,** 055001 (2009).

[6] I. Zana and G. Zangari. *Electrodeposition of Co-Pt films with high perpendicular anisotropy*. Electrochem. Solid-State Lett. **6**, C153 (2003).

[7] G. H. Fredrickson and F. S. Bates. *Dynamics of block copolymers: Theory and experiment*. Annu. Rev. Mater. Sci. **26**, 501 (1996).

[8] C. Deneke, C. Müller, N. Y. Jin-Phillipp and O. G. Schmidt. *Diameter scalability of rolled-up In(Ga)As/GaAs nanotubes*. Semicond. Sci. Technol. **17**, 1278 (2002).

[9] C. Deneke, U. Zschieschang, H. Klauk and O. G. Schmidt. *InGaAs/GaAs/alkanethiolate radial superlattices*. Appl. Phys. Lett. **89**, 263110 (2006).

[10] C. Deneke, J. Schumann, R. Engelhard, J. Thomas, C. Müller, M. S. Khatri, A. Malachias, M. Weisser, T. H. Metzger and O. G. Schmidt. *Structural and magnetic properties of an InGaAs/*Fe_3Si *superlattice in cylindrical geometry*. Nanotechnology **20,** 045703 (2009).

[11] C. Müller, M. S. Khatri, C. Deneke, S. Fähler, Y. F. Mei, E. Bermúdez Ureña and O. G. Schmidt. *Tuning magnetic properties by roll-up of Au/Co/Au films into microtubes*. Appl. Phys. Lett. **94**, 102510 (2009).

[12] B. D. Cullity. *Introduction to magnetic materials*. Addision-Wesley, Philippines (1972).

[13] C. L. Faust. *In modern electroplating*. Wiley, New York (1974).

[14] M. Paunovic and M. Schlesinger. *Fundamentals of electrochemical deposition*. Wiley-Interscience, New Jersey (1998).

[15] F. Wang, K. Hosoiri, S. Doi, N. Okamoto, T. Kuzushima, T. Totsuka and T. Watanabe. *Nanostructured* $L1_0$ *Co-Pt thin films by an electrodeposition process*. Electrochem. Commun. **6**, 1149 (2004).

[16] S. Shiomi, H. Okazawa, T. Nakakita, T. Kobayashi and M. Masuda. *Magnetic properties of CoPt alloy films sputtered on Pt underlayers*. Jpn. J. Appl. Phys. **32**, L315 (1993).

---

[17] D. Weller and A. Moser. *Thermal effect limits in ultrahigh-density magnetic recording*. IEEE Trans. Magn. **35**, 4423 (1999).

[18] J. H. Judy. *Advancements in PMR thin film media*. J. Magn. Magn. Mater. **287**, 16 (2005).

[19] R. L. White, R. M. H. New and R. F. W. Pease. *Patterned media: a viable route to 50 Gbit/in^2 and up for magnetic recording?*. IEEE Trans Magn. **33**, 990 (1997).

[20] H. A. M. Haast, J. R. Schuurhuis, L. Abelmann, J. C. Lodder and T. J. Popma. *Reversal mechanism of submicron patterned CoNi/Pt multilayers*. IEEE Trans. Magn. **34**, 1006 (1998).

[21] J. S. Chen, B. C. Lim, J. F. Hu, Y. K. Lim, B. Liu and G. M. Chow. *High coercivity $L1_0$ FePt films with perpendicular anisotropy deposited on glass substrate at reduced temperature*. Appl. Phys. Lett. **90**, 42508 (2007).

[22] K. Barmak, J. Kim, L. H. Lewis, K. R. Coffey, M. F. Toney, A. J. Kellock and J. –U. Thiele. *On the relationship of magnetocrystalline anisotropy and stoichiometry in epitaxial $L1_0$ CoPt (001) and FePt (001) thin films*. J. Appl. Phys. **98**, 33904 (2005).

[23] Binary alloy phase diagrams, 2nd ed. William W. Scott., Jr. vol. **2,** p.1225 (1990).

[24] C. Leroux, M. C. Cadeville, V. P. Bohnes, G. Inden and F. Hinz. *Comparative study of structural and transport properties of $L1_0$ NiPt and CoPt phases; the role of magnetism*. J. Phys. F: Met. Phys. **18**, 2033 (1988).

[25] Y. Yamada, T. Suzuki, H. Kanazawa and J. C. Österman. *The origin of the large perpendicular magnetic anisotropy in Co_3Pt alloy thin films*. J. Appl. Phys. **85**, 5094 (1999).

[26] W. M. Liao, S. K. Chen, F. T. Yuan, C. W. Hsu and H. Y. Lee. *Thickness dependence of crystallographic and magnetic properties for $L1_0$-CoPt thin films*. J. Magn. Magn. Mater. **303**, e243 (2006).

[27] A. Tsoukatos, H. Wan, G. C. Hadjipanayis, Y. J. Zhang and M. Waite. *Thickness effects of the magnetic hysteresis of Co-Pt films*. J. Magn. Magn. Mater. **118**, 387 (1993).

[28] H. Zeng, M. L. Yan, N. Powers and D. J. Sellmyer. *Orientation controlled nonepitaxial $L1_0$ CoPt and FePt films*. Appl. Phys. Lett. **80**, 2350 (2002).

[29] M. R. Visokay and R. Sinclair. *Direct formation of ordered CoPt and FePt compound thin films by sputtering*. **66**, 1692 (1995).

[30] E. Agostinelli, S. Laureti, G. Varvaro, A. Generosi, B. Paci, V. Rossi-Albertini, G. Scavia and A. M. Testa. *Study of structural microstructural and magnetic properties of very thin $Co_{50}Pt_{50}$ films deposited by PLD*. Mat. Sci. Eng. C **27**, 1466 (2007).

[31] M. Yu, H. Ohguchi, A. Zambano, I. Takeuchi, J. P. Liu, D. Josell and L. A. Bandersky. *Orientation and magnetic properties of FePt and CoPt films grown on MgO (110) single-crystal substrate by electron-beam coevaporation*. Mat. Sci. Eng. B-Solid. **142**, 139 (2007).

[32] R. A. Ristau, K. Barmak, L. H. Lewis, K. R. Coffey and J. K. Howard. *On the relationship of high coercivity and $L1_0$ ordered phase in CoPt and FePt thin films*. J. Appl. Phys. **86**, 4527 (1999).

[33] A. Tsoukatos, H. Wan, G. C. Hadjipanayis, Y. J. Zhang and M. Waite. *Thickness effect on magnetic hysteresis of Co-Pt films*. J. Magn. Magn. Mater. **118**, 387 (1993).

---

[34] JCPDS-International centre for diffraction data, CoPt, Card No. 43-1358 (1997).

[35] G. R. Harp, D. Weller, T. A. Rabedeau, R. F. C. Farrow and M. F. Toney. *Magneto-optical Kerr spectroscopy of a new chemically ordered alloy:* Co_3Pt*.* Phys. Rev. Lett. **71**, 2493 (1993).

[36] J. K. Howard. *The effect of Cr and W nucleation layers on the magnetic properties of CoPt films*. J. Appl. Phys. **63**, 3263 (1988).

[37] K. K. M. Pandey, J. S. Chen, G. M. Chow and B. C. Lim. *Seedlayer interface enhanced magnetic anisotropy in CoPt (0002)-textured films*. J. Magn. Magn. Mater. In Press.

[38] J. Ariake, T. Chiba, S. Watanabe, N. Honda and K. Ouchi. *Magnetic and structural properties of Co-Pt perpendicular recording media with large magnetic anisotropy*. J. Magn. Magn. Mater. **287**, 229 (2009).

[39] T. Shimatsu, H. Sato, T. Oikawa, Y. Inaba, O. Kitakami, S. Okamoto, A. Aoi, H. Muraoka and Y. Nakamura. *High-potential magnetic anisotropy of* $CoPtCr\text{-}SiO_2$ *perpendicular recording media*. IEEEE Trans. Magn. **41**, 566 (2005).

[40] J. Zhu, Y. G. Peng and D. E. Laughlin. *Toward an understanding of grain-to-grain anisotropy field variation in thin film media*. IEEE Trans. Magn. **41**, 543 (2005).

[41] K. Barmak, R. A. Ristau, K. R. Coffey, M. A. Parker and J. K. Howard. *Grain growth and ordering kinetics in CoPt thin films*. J. Appl. Phys. **79**, 5330 (1996).

[42] H. Kanazawa, G. Lauhoff and T. Suzuki. *Magnetic and structural properties of* $(Co_xFe_{1-x})_{50}Pt_{50}$ *alloy thin films*. J. Appl. Phys. **87**, 6143 (2000).

[43] O. Berkh, Y. Rosenberg, Y. S. Diamand and E. Gileadi. *Electrodeposited near-equiatomic CoPt thick film. Electrochem*. Solid-State Lett. **11(4)**, D38 (2008).

[44] K. Z. Rožman, A. Krause, K. Leistner, S. Fähler, L. Schultz and H. Schlörb. *Electrodeposition and hard magnetic properties of Co-Pt films in comparison to Fe-Pt films*. J. Magn. Magn. Mater. **314**, 116 (2007).

[45] P. L. Wu, X. H. Li, W. Li, H. Y. Sun, Y. Chen and X. Y. Zhang. *Microstructure and magnetic behavior of electrodeposited CoPt thick films upon annealing*. Mater. Lett. **62**, 309 (2008).

[46] K. Hosoiri, F. Wang, S. Doi and T. Watanabe. *Preparation and characterization of electrodeposited Co-Pt binary alloy film*. Mater. Trans. **44**, 653 (2003).

[47] I. Zana, G. Zhangari and M. Shamsuzzoha. *Enhancing the perpendicular magnetic anisotropy of Co-Pt(P) films by epitaxial electrodeposition on to Cu(111) substrates*. J. Magn. Magn. Mater. **292**, 266 (2005).

[48] G. Pattanaik, J. Weston and G. Zangari. *Magnetic properties of Co-rich Co-Pt films electrodeposited on a Ru underlayer*. J. Appl. Phys. **99**, 08E901-1 (2006).

[49] I. Zana and G. Zangari. *Magnetic properties of electrodeposited Co-Pt thin films with very high perpendicular magnetic anisotropy*. J. Magn. Magn. Mater. **272**, 1698 (2004).

[50] M. Ghidini, G. Zangari, I. L. Prejbeanu, G. Pattanaik, L. D. Buda-Prejbeanu, G. Asti, C. Pernechele and M. Solzi. *Magnetization processes in hard Co-rich CoPt films with perpendicular anisotropy*. J. Appl. Phys. **100**, 103911 (2006).

---

[51] T. S. Eagleton, J. Mallet, X. Cheng, J. Wang, C. L. Chien and P. C. Searson. *Electrodeposition of Co_xPt_{1-x} thin films*. J. Electrochem. Soc. **152**, C27 (2005).

[52] S. Y. Chou, M. Wei, P. R. Krauss and P. B. Fisher. *Study of nanoscale magnetic structures fabricated using electron-beam lithography and quantum magnetic disk*. J. Vac. Sci. Technol. B. **12(6)**, 3695 (1994).

[53] M. Hehn, K. Ounadjela, J. P. Bucher, F. Rousseaux, D. Decanini, B. Bartenlian and C. Chappert. *Nanoscale magnetic domains in mesoscopic magnets*. Science. **272**, 1782 (1996).

[54] H. Masuda and K. Fukuda. *Ordered metal nanohole arrays made by a two step replication of honeycomb structures of anodic alumina*. Science. **268**, 1466 (1995).

[55] C. R. Martin. *Nanomaterials: A membrane-based synthetic approach*. **266**, 1961 (1994).

[56] A. Fert and L. Piraux. *Magnetic nanowires*. J. Magn. Magn. Mater. **200**, 338 (1999).

[57] T. Thun-Albrecht, J. Schotter, G. A. Kästle, N. Emley, T. Schibauchi, L. Krusi-Elbaum, K. Guarini, C. T. Black, M. T. Tuominen and T. P. Russell. *Ultrahigh-density nanowire arrays grown in self-assembled diblock copolymer templates*. Science, **290**, 2126 (2000).

[58] A. Sidorenko, I. Tokarev, S. Minko and M. Stamm. *Ordered Reactive nanomembranes/nanotemplates from thin films of block copolymer supramolecular assembly*. J. Am. Chem. Soc. **125**, 12211 (2003).

[59] M. Muthukumar, C. K. Ober and E. L. Thomas. *Competing interactions and levels of ordering in self-organized polymeric materials*. Science. **277**, 1225 (1997).

[60] I. Tokarev. *Order in thin films of diblock copolymers by supramolecular assembly*. Dissertation, Dresden University of Technology. (2004).

[61] M. W. Matsen and M. Schick. *Stable and unstable phases of diblock copolymer melt*. Phys. Rev. Lett. **72**, 2660 (1994).

[62] M. Park, Ch. Harrision, P. M. Chaikin, R. A. Register and D. H. Adamson. *Block copolymer lithography*: *periodic arrays of ~10^{11} holes in 1 square centimeter*. Science. **276**, 1401 (1999).

[63] T. Thurn-Albrecht, R. Steiner, J. De Rouchey, C. M. Stafford, E. Huang, M. Bal, M. Tuominen, C. J. Hawker and T. P. Russell. *Nanoscopic templates from oriented block copolymer films*. Adv. Mater. **12**, 787 (2000).

[64] I. Tokarev, A. Sidorenko, S. Minko and M. Stamm. *Switching nanotemplates*. Polym. Mater. Sci. Eng. **90**, 292 (2004).

[65] R. Mäki-Ontto, K. de Moel, W. de Odorico, J. Ruokolainen, M. Stamm, G. ten Brinke and O. Ikkala. "*Hairy Tubes*": *Mesoporous materials containing hollow self-organized cylinders with polymer brushes at the walls*. Adv. Mater. **13**, 117 (2001).

[66] J. Mallet, K. Y. Zhang, S. M. Tempfli, M. M. Tempfli and L. Piraux. *Electrodeposited $L1_0$ Co_xPt_{1-x} nanowires*. J. Phys. D. Appl. Phys. **38**, 909 (2005).

[67] N. Yasui, A. Imada and T. Den. *Electrodeposition of (001) oriented CoPt $L1_0$ columns into anodic alumina films*. Appl. Phys. Lett. **83**, 3347 (2003).

[68] Y. Dahmane, L. Cagnon, J. Voiron, S. Pairis, M. Bacia, L. Ortega, N. Benbrahim and A. Kadri. *Magnetic and structural properties of electrodeposited CoPt and FePt nanowires in nanoporous alumina templates*. J. Phys. D: Appl. Phys. **39**, 4523 (2006).

---

[69] A. I. Gapin, X. R. Ye, J. F. Aubuchon, L. H. Chen, Y. J. Tang and S. Jin. *CoPt patterned media in anodized aluminum oxide templates*. J. Appl. Phys. **99**, 08G902-1 (2006).

[70] Y. H. Huang, H. Okumura and G. C. Hadjipanayis. *CoPt and FePt nanowires by electrodeposition*. J. Appl. Phys. **91**, 6869 (2002).

[71] J. H. Gao, D. L. Sun, X. Q. Zhang, Q. F. Zhan, W. He, Y. Sun and Z. H. Cheng. *Structure and magnetic properties of the self-assembled* $Co_{52}Pt_{48}$ *nanowire arrays*. Appl. Phys. Lett. **92**, 102501 (2008).

[72] J. H. Min, J. H. Wu, J. U. Cho, J. H. Lee, Y. D. Ko, H. L. Liu, J. S. Chung and Y. K. Kim. *Electrochemical preparation of* Co_3Pt *nanowires*. Phys. Stat. Sol. (a) **204**, 4158 (2007).

[73] W. Li and T. H. Shen. *Composition and annealing temperature dependent properties of* $Co_{1-x}Pt_x$ *($0<x\leq 0.2$) alloy nanowire arrays*. J. Appl. Phys. **97**, 10J706-1 (2005).

[74] H. Li, C. Xu, G. Zhao, Y. Su, T. Xu and H. Li. *Fabrication and magnetic properties of amorphous* $Co_{0.71}Pt_{0.29}$ *nanowires arrays*. Solid State Commun. **132**, 399 (2004).

[75] H. P. J. Wijn. *Data in science and technology, Magnetic properties of metals*. Springer, Berlin (1991).

[76] S. Shamila, R. Sharif, S. Riaz, M. Ma, M. K. Rahman and X. F. Han. *Magnetic and magnetization properties of electrodeposited fcc CoPt nanowire arrays*. J. Magn. Magn. Mater. **320**, 1803 (2008).

[77] J. U. Cho, J.-H. Wu, J. H. Min, S. P. Ko, J. Y. Soh, Q. X. Liu and Y. K. Kim. *Control of magnetic anisotropy of Co nanowires*. J. Magn. Magn. Mater. **303**, e281 (2006).

[78] H. Masuda, F. Hasegwa and S. Ono. *Self-ordering of cell arrangement of anodic porous alumina formed in sulphuric acid solution*. J. Electrochem. Soc. **144**, L127 (1997).

[79] O. Jessensky, F. Müller and U. Gösele. *Self-organized formation of hexagonal pore arrays in anodic alumina*. Appl. Phys. Lett. **72**, 1173 (1998).

[80] V. Sadasivan, C. P. Richter, L. Menon and P. F. Williams. *Electrochemical self-assembly of porous alumina templates*. AIChE Journal **51(2)**, 649 (2005).

[81] H. Jiang and M. J. O'Shea. *Structure and magnetic properties of NdFeB thin films with Cr, Mo, Nb, Ta, Ti, and V buffer layers*. J. Magn. Magn. Mater. **212,** 59 (2000).

[82] Materials science and technology, vol. 2a/2b. *Characterization of materials*. Wiley-VCH Weinheim (2005).

[83] C. R. Blanchard. *Atomic force microscopy*. The chemical educator. **1(5)**, 1 (1996).

[84] U. Hartmann. *Magnetic force microscopy*. Annu. Rev. Mater. Sci. **29**, 53 (1999).

[85] R. Rugar, H. J. Mamin, P. Guethner, S. E. Lambert, J. E. Stern, I. McFadyen and T. Yogi. *Magnetic force microscopy: General principles and application to longitudinal recording media*. J. Appl. Phys. **68 (3)**, 1169 (1990).

[86] V. Neu, K. Häfner, A. K. Patra and L. Schultz. *Fully epitaxial, exchange coupled* $SmCo_5/Fe/SmCo_5$ *trilayers*. J. Phys. D: Appl. Phys. **39**, 5116 (2006).

---

[87] F. Schmidt and A. Hubert. *Domain observations on CoCr-layers with a digitally enhanced Kerr microscope*. J. Magn. Magn. Mater. **61**, 307 (1986).

[88] A. Hubert and R. Schäfer. *Magnetic domains: the analysis of magnetic microstructures*. Springer, Berlin (1998).

[89] A. Asenjo, J. M. García, D. García, A. Hernando, M. Vázquez, P. A. Caro, D. Ravelosona, A. Cebollada and F. Briones. *MFM imaging of FePd stripe domains. Evolution with Pt buffer layer thickness*. J. Magn. Magn. Mater. **196**, 23 (1999).

[90] G. Wei, H. Ge, Q. Wu, Y. Yu, X. Wang and C. Chen. *Co-Pt-W thin films electrodeposited from sulphate-gluconate baths*. Mater. Chem. Phys. In Press.

[91] M. Donten and J. Osteryoung. *Electrochemical and chemical reaction in baths for plating amorphous alloys*. J. Appl. Electrochem. **21**, 496 (1991).

[92] R. C. O'Handley. *Modern magnetic materials: Principles and applications*. A Wiley-Interscience, New York (2000).

[93] F. Li, T. Wang, L. Ren and J. Sun. *Structure and magnetic properties of Co nanowires in self-assembled arrays*. J. Phys.: Condens. Matter **16**, 8053 (2004).

[94] L. Piraux, S. Dubois, E. Ferain, R. Legras. K. Ounadjela, J. M. George, J. L. Maurice and A. Fert. *Anisotropic transport and magnetic properties of arrays of sub-micron wires*. J. Magn. Magn. Mater. **165**, 352 (1997).

[95] A. K. M. Bantu, J. Rivas, G. Zaragoza, M. A. López-Quintela and M. C. Blanco. *Structure and magnetic properties of electrodeposited cobalt nanowires*. J. Appl. Phys. **89**, 3393 (2001).

[96] J. U. Cho, J. H. Wu, J. H. Min, S. P. Ko, J. Y. Soh, Q. X. Liu and Y. K. Kim. *Control of magnetic anisotropy of Co nanowires*. J. Magn. Magn. Mater. **303**, e281 (2006).

[97] H. Khurshid, Y. H. Huang, M. J. Bonder and G. C. Hadjipanayis. *Microstructural and magnetic properties of CoPt nanowires*. J. Magn. Magn. Mater. **321**, 277 (2009).

[98] K. Shin, K. A. Leach, J. T. Goldbach, D. H. Kim, J. Y. Jho, M. Tuominen, C. J. Hawker and T. P. Russel. *A simple route to metal nanodots and nanoporous metal films*. Nanoletters. **2**, 933 (2002).

[99] M. S. Khatri, H. Schlörb, S. Fähler, L. Schultz, B. Nandan, M. Böhme, R. Krenek and M. Stamm. *Electrodeposition of Co-Pt continuous films and nanowires within diblock copolymer template*. Electrochimica Acta **54**, 2536 (2009).

[100] V. Y. Prinz, V. A. Seleznev, A. K. Gutakovsky, A. V. Chehovskiy, V. V. Preobrazhenskii, M. A. Putyato and T. A. Gavrilova. *Free-standing and overgrown InGaAs/GaAs nanotubes, nanohelices and their arrays*. Physica E **6**, 828 (2000).

[101] O. G. Schmidt and K. Eberl. *Thin solid films rolled up into nanotubes*. Nature (London) **410**, 168 (2001).

[102] O. G. Schmidt, N. Schmarje, C. Deneke, C. Müller and N.-Y. Jin-Phillipp. *Three-dimensional nano-objects evolving from a two-dimensional layer technology*. Adv. Mater. **13**, 756 (2001).

[103] V. Luchnikov, O. Sydorenko and M. Stamm. *Self-rolled polymer and composite polymer/metals micro- and nanotubes with patterned inner walls*. Adv. Mater. **17**, 1177 (2005).

---

[104] O. Schumacher, S. Mendach, H. Welsch, A. Schramm, Ch. Heyn and W. Hansen. *Lithographically defined metal-semiconductor-hybrid nanoscrolls*. Appl. Phys. Lett. **86**, 143109 (2005).

[105] M. Huang, C. Boone, M. Roberts, D. E. Savage, M. G. Lagally, N. Shaji, H. Qin, R. Blick, J. A. Nairn and F. Liu. *Nanomechanical architecture of strained bilayer thin films: from design principles to experimental fabrication*. Adv. Mater. **17**, 2860 (2005).

[106] C. Deneke and O. G. Schmidt. *Structural characterization and potential x-ray waveguiding of a small rolled-up nanotube with a large number of windings*. Appl. Phys. Lett. **89**, 123121 (2006).

[107] S. Mendach, R. Songmuang, S. Kiravittaya, A. Rastelli, M. Benyoucef and O. G. Schmidt. *Light emission and wave guiding of quantum dots in a tube*. Appl. Phys. Lett. **88**, 111120 (2006).

[108] T. Kipp, H. Welsch, Ch. Strelow, Ch. Heyn and D. Heitmann. *Optical modes in semiconductor microtube ring resonators*. Phys. Rev. Lett. **96**, 077403 (2006).

[109] S. Mendach, S. Mendach, O. Schumacher, H. Welsch, Ch. Heyn, W. Hansen and M. Holz. *Evenly curved two-dimensional electron systems in rolled-up Hall bars*. Appl. Phys. Lett. **88**, 212113 (2006).

[110] O. G. Schmidt, C. Deneke, S. Kiravittaya, R. Songmuang, H. Heidemeyer, Y. Nakamura, R. Zapf-Gottwick, C. Müller and N. Y. Jin-Phillipp. *Self-assembled nanoholes, lateral quantum-dot molecules, and rolled-up nanotubes*. IEEE J. Sel. Top. Quantum Electron. **8**, 1025 (2002).

[111] C. Deneke and O. G. Schmidt. *Real-time formation, accurate positioning, and fluid filling of single rolled-up nanotubes*. Appl. Phys. Lett. **85**, 2914 (2004).

[112] Y. Mei, G. Huang, A. A. Solovev, E. Bermúdez Ureňa, I. Mönch, F. Ding, T. Reindl, R. K. Y. Fu, P. K. Chu and O. G. Schmidt. *Versatile approach for integrative and functionalized tubes by strain engineering of nanomembranes on polymers*. Adv. Mater. **20**, 4085 (2008).

[113] R. Songmuang, C. Deneke and O. G. Schmidt. *Rolled-up micro-and nanotubes from single-material thin films*. Appl. Phys. Lett. **89**, 223109 (2006).

[114] D. R. Lide. *CRC Handbook of Chemistry and Physics. CRC*, Boca Raton (2008).

[115] J. Nogués and I. K. Schuller. *Exchange bias*. J. Magn. Magn. Mater. **192**, 203 (1999).

[116] K. Schäfer and G. Beggerow. *Landolt Börnstein: Mechanische-Thermische Zustandgröße.* (1) Springer, Berlin (1971).

[117] A. Kumar, S. Fähler, H. Schlörb, K. Leistner and L. Schultz. *Competition between shape anisotropy and magnetoelastic anisotropy in Ni nanowires electrodeposited within alumina templates*. Phys. Rev. B **73**, 064421 (2006).

[118] W. Martienssen and H. Warlimont. *Handbook Materials Data.* Springer, Heidelberg (2005).

Publication List

Some of the results in this work are published in the following papers.

1. M. S. Khatri, H. Schlörb, S. Fähler, L. Schultz, B. Nandan, M. Böhme, R. Krenek and M. Stamm. *Electrodeposition of Co-Pt continuous films and nanowires within diblock copolymer template*. Electrochimica Acta **54**, 2536 (2009).

2. C. Müller, M. S. Khatri, C. Deneke, S. Fähler, Y. F. Mei, E. Bermúdez Ureña and O. G. Schmidt. *Tuning magnetic properties by roll-up of Au/Co/Au films into microtubes*. Appl. Phys. Lett. **94**, 102510 (2009).

3. C. Deneke, J. Schumann, R. Engelhard, J. Thomas, C. Müller, M. S. Khatri, A. Malachias, M. Weisser, T. H. Metzger and O. G. Schmidt. *Structural and magnetic properties of an InGaAs/Fe_3Si superlattice in cylindrical geometry*. Nanotechnology **20,** 045703 (2009).

Acknowledgements

It would not have been possible to write this doctoral thesis without the help and support of the kind people around me, to some of whom it is possible to give particular mention here.

First and foremost I wish to thank my supervisor Prof. Dr. Ludwig Schultz for giving me an opportunity to carry out doctoral work at IFW Dresden. I am thankful to him for his encouragements, valuable comments and suggestions about my work and providing me the full freedom and pleasant work atmosphere to carry out this work.

I owe my gratitude to Dr. Heike Schlörb for her significant positive influence through her role as both my project leader and my advisor. It was under her direct supervision that the work contained in this thesis was performed. Without her encouragement and constant guidance, I could not have finished this dissertation.

I am grateful to Dr. Sebastian Fähler for helping me complete the writing of this dissertation as well as the research that lies behind it. He was always there to meet and talk about my ideas, to proofread and mark up my papers and chapters, and to ask me good questions to help me think through my problems.

A special thanks goes to Ms. S. Neitsch for fabricating alumina templates for my experiments and for her help in all electrochemical stuffs in the lab.

I would like to thank Ms. K. Hennig for making cross-sectional SEM images on several Co-Pt films and Co-Pt within diblock copolymer template.

My thank also go to Dr. B. Nandan, M. Böhme, Dr. R. Krenek and Prof. Dr. M. Stamm at IPF Dresden for providing diblock copolymer templates.

I would like to thank Dr. C. Müller for providing the rolled-up microtubes for magnetic measurements and for his help in MFM measurements on Co-Pt films.

Let me also say ‘thank you’ to all colleagues like Dr. S. Haindl, T. Niemeier, Dr. K. Leistner, A. K. Srivastava, V. Hähnel, D. Iselt and D. Pohl.

I would like to thank all the members of department 21 for their direct and indirect help and support.

I would like to thank Ms. K. Clausnitzer and Ms. S. Schumann for all the help related to the office work.

I must not forget the support of our Library staff and I thank them all.

I would like to acknowledge the Special Priority Program SPP 1165 of Deutsche Forschungsgemeinschaft (DFG) for funding the project SCHL 589/2.

I am very grateful to Dr. A. K. Patra for his support and encouragement throughout my PhD work.

I would like to thank all my Indian friends (Dr. K. Biswas, Dr. R. B. Gangineni, Dr. P. Kumar, Dr. R. Mahaling, Dr. V. S. Vidyarthi, A. Mukherjee, S. M. Gorantla, S. Kumar, S. Aswartham and K. B. Surreddi) for their help and moral support.

And last, but definitely not least, I would like to thank my parents and family members, who have always supported me in my endeavors, always given me the strength and encouragement.

Perhaps, I forgot someone… so, just in case: thank you to whom it concerns!

Versicherung

Hiermit versichere ich, dass ich die vorliegende Arbeit ohne unzulässige Hilfe Dritter und ohne Benutzung anderer als der angegebenen Hilfsmittel angefertigt habe; die aus fremden Quellen direkt oder indirekt übernommenen Gedanken sind als solche kenntlich gemacht. Die Arbeit wurde bisher weder im Inland noch im Ausland in gleicher oder ähnlicher Form einer anderen Prüfungsbehörde vorgelegt. Ich erkenne die Promotionsordnung der Technischen Universität Dresden an.

Diese Arbeit wurde am Leibniz-Institut für Festkörper - und Werkstoffforschung (IFW) Dresden unter der wissenschaftlichen Betreuung von Prof. Dr. L. Schultz angerfertigt.

Dresden, den 12.01.2010
Manvendra Singh Khatri